Università di Pisa

Department of Civil and Industrial Engineering
Master's Degree in Materials & Nanotechnology

Superconducting Quantum Interference Devices based on InSb nanoflags

Supervisors:
Prof. Stefan Heun
Prof. Lucia Sorba

Candidate:
Andrea Chieppa

Academic year 2023/2024

Abstract

In mesoscopic physics, interference effects play a relevant role in determining the behavior and the transport properties of quantum devices. Among all, interference phenomena are of particular importance in the context of superconducting systems. Indeed, superconducting quantum interference devices, known as SQUIDs, have found several applications in magnetometry, scanning probe microscopies, and more recently quantum computing. Besides, SQUIDs in the strongly asymmetric geometry are useful to investigate fundamental properties of Josephson junctions, for instance to extract the Current Phase Relationship (CPR).

In this master thesis, we report the first fabrication and characterization of SQUIDs made with InSb nanoflag-based Josephson junctions. The two arms of the SQUIDs are composed of two superconducting-normal-superconducting junctions, where the normal part is a single InSb nanoflag, a semiconductor with strong spin-orbit coupling and with quasi-2D electronic transport. Making use of the elongated shape of the nanoflags, both symmetric and asymmetric SQUID geometries are realized. Characterization at low temperature is performed by magneto transport measurements, showing supercurrent interference for various values of temperature and back gate.

Interference can be controlled by the back gate, which allows to tune from partial or total destructive interference. An additional tuning knob is the applied perpendicular magnetic field, which allows to choose an optimal working point. In the symmetric geometry, the typical SQUID interference pattern is observed. In the asymmetric geometry, the two nanoflags respond differently to the global back gate. This enables the suppression of the supercurrent in one junction at a time, allowing for the observation of no interference as the supercurrent in one arm is extinguished.

Acknowledgments

I would like to express my deepest gratitude to my supervisors, Prof. Stefan Heun and Prof. Lucia Sorba, for introducing me to the field of experimental physics. I will always be grateful for this valuable opportunity. When I started, I didn't even know how to use an instrument, but thanks to your guidance, I soon became proficient in conducting experiments independently. The degree of independence and trust I was granted allowed me to learn by doing—an increasingly rare fortune these days. I also extend my heartfelt thanks to Dr. Giada Bucci, who carefully explained every fabrication step of my devices in real time in the clean-room, allowing me to explore the fascinating world of nano-fabrication with a direct-experience. Alongside Dr. Giada Bucci, I would like to thank Dr. Gaurav Shukla. Your fabrication of the devices was fundamental, and this thesis would not exist without your invaluable contribution and expertise. My appreciation goes to Dr. Sergio Pezzini and Dr. Ivan Villani for their patience in teaching me about the cryogenic setup, insightful discussions, and extensive technical support with the experiments. I am also immensely grateful to Dr. Matteo Carrega, who read the entire thesis, provided invaluable advice, and offered useful observations. I would like to extend my gratitude to the theoretical group of Prof. Maura Sassetti, particularly Dr. Simone Traverso and Dr. Samuele Fracassi. I learned a great deal from our discussions, and I am thankful for the physical insights you shared. Special thanks go to my lab mate, Antonio. Your company truly enriched my weeks and weekends in the laboratory with exciting discussion about physics. I would also like to thank my colleagues from the Nanoscience group at NEST: Matteo, Gabriele, Giulio, and Simone, for making my experience memorable.

As I reach the end of my journey in Pisa, a special thanks goes to all my friends, from the "Maledetti Toscani" to the "Cenetta Incredibile" group, with particular gratitude to Giovanni, Francesco and Francesca. A heartfelt acknowledgment to my lifelong friends from Rionero: Gianpiero, Mauro, Giovanni, Carmine, Gennaro, and Clarissa. To my family and my constant supporter, Valeria, this thesis is dedicated to you.

Contents

1

Introduction

Motivation

In recent years, quantum technologies have seen an incredible development pushed by the ever-increasing need for improvement of the performance of quantum devices. Superconducting electronics promises such improvements, with many applications in a large variety of fields.

One important area of research is the field of quantum computation. Quantum computing aims at solving problems that classical computation cannot overcome, by taking advantage of the quantum superposition of two logic states [1]. Although quantum computers and quantum bits have already been demonstrated, they are subject to noise and decoherence caused by the environment, making them highly prone to errors. To mitigate this problem, one approach is to use topological states as logic states, which would lead to a more robust and fault-tolerant quantum computation[2].

A possible platform for implementing this method of topologically protected quantum computation are superconductor-semiconductor hybrids, but to drive the system in a topological phase several requirements must be met [3]. If the superconductor possess an s-wave pairing symmetry, the semiconducting material should possess a large spin-orbit interaction [4], while a large Landè g factor would be needed to limit the magnetic field at which the transition to the topological phase happens.

Among the variety of semiconductors, some materials are natural candidates like InAs [5], HgTe [6] or InSb [7, 8]. To this end, the InSb nanoflag, the semiconducting material used in this thesis, offers the two-dimensional platform with large spin-orbit interaction and large Landè g factor. Previously, the group reported ballistic InSb nanoflags-based Josephson junctions [9], which exhibited intriguing phenomena such as half-integer Shapiro steps and the superconducting diode effect [10, 11].

To explain these observations, a non-sinusoidal current-phase relationship (CPR) has been proposed. However, to date, no measurement of the CPR has been performed and remains an open problem to be addressed experimentally. Proposals on how to probe the CPR involve the use of Superconducting Quantum Interference Devices (SQUIDs) in strongly asymmetric configurations [12, 13]. In these setups, it is possible to separate the contribution of each junction to the total supercurrent, allowing to understand the behavior of the CPR as a function of different variables. Other approaches involve the use of SQUIDs and tunneling spectroscopy to examine the energy spectrum to obtain a indirect reconstruction of the CPR [14].

Because of this, there is lot of interest in investigating InSb nanoflags with SQUIDs. In fact, the investigations of superconducting quantum effects was prevalently done on single junctions [15] and SQUIDs with two-dimensional nanostructures of InSb have not been reported yet.

Motivated by these arguments, in this thesis I investigate dc-SQUIDs based on InSb nanoflags. The thesis is structured in the following way:

- In Chapter 2, the theoretical background is provided.
- In Chapter 3, the experimental setup is described, from the fabrication steps to the details of the measurements.
- In Chapter 4, the main results of this work are presented.
- Chapter 5 concludes the thesis with a comment on the future perspectives.

These chapters are further supported by two appendices. In Appendix A the algorithm used to extract the values of the critical current from the VI curves is discussed. In Appendix B the details of the numerical simulations are provided.

2

Theoretical Background

2.1 Semiconductors

This section focuses on summarizing the properties of semiconducting systems that are needed in the understanding of the physics presented in the experimental part. Semiconductors are crystalline materials in which electrons occupy energy levels grouped together in energy bands. From low to high energy and at zero temperature, the last occupied energy band is called *valence band*, while the first empty band is called *conduction band*. These two bands are separated in energy by the band-gap, the lowest energy scale needed to excite one electron from the valence to the conduction band.

The semiconducting system used in this thesis is Indium Antimonide (InSb), a material that at zero temperature has a small band gap of $0.24\,\mathrm{eV}$ and crystallize in a zinc-blende structure. Fig. 2.1 shows a schematic of the band structure of bulk InSb at room temperature.

One remarkable property of semiconducting materials is that when electrons are excited near the bottom of the conduction band (by thermal excitation or other means), the role of the crystal is to renormalize the mass of these carriers in such a way that they

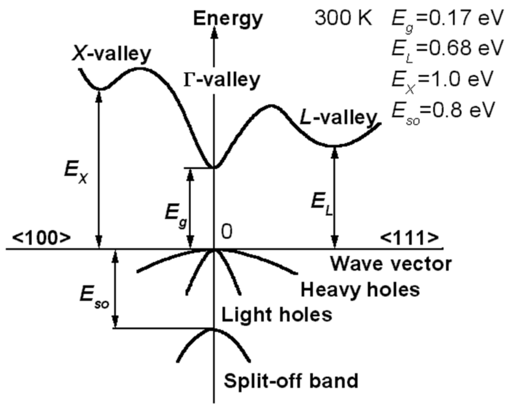

Figure 2.1: InSb band structure at $300\,\mathrm{K}$. Source: [16].

behave as having a different, *effective*, mass m^*. For an infinite semiconductor, within the effective mass approximation, the energy of the electrons near the bottom of the conduction band is described in k-space by:

$$E(\vec{k}) = \frac{\hbar^2}{2m_x^*}k_x^2 + \frac{\hbar^2}{2m_y^*}k_y^2 + \frac{\hbar^2}{2m_z^*}k_z^2 \tag{2.1}$$

2.1.1 *Two-dimensional systems*

The semiconducting system presented in this thesis is a two-dimensional nanostructure of InSb. To show two-dimensional behavior, the motion of the system in one direction (e.g., z) must be highly quantized. Consider an electron system in a box whose energy is described by eq. 2.1, and with the lowest de-Broglie wavelength, the Fermi wavelength λ_F, which is much larger than the confinement direction length, L_z. If the size of the box[1] is reduced such that $L_x, L_y \gg L_z$ then the momentum states in the plane $k_{x,y} = 2\pi/L_{x,y}$ will be continuous with respect to those in the perpendicular direction, where motion will be highly quantized. In this sense, the system behaves as two-dimensional, as little perturbations will fill the in-plane momentum states before exciting the momentum states in the z direction, producing a confinement in one direction. Confinement in these systems results in the formation of what are called *subbands* which are shown schematically in Fig. 2.2.

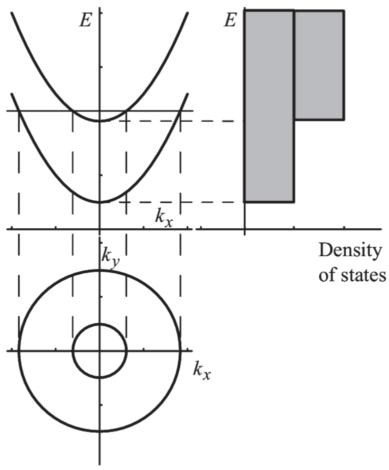

Figure 2.2: Electronic two-dimensional subbands in reciprocal space. Adapted from [17]

Not always $\lambda_F \gg L_z$, and many systems, like the one used in this thesis, are in a situation where $\lambda_F \simeq L_z$. In this case, the system is considered in a a quasi-$2D$ regime.

[1]A more correct formulation is uses the Schrodinger equation for the envelope function of the electrons, in which the confinement potential is given by the vacuum level, but the qualitative picture is the same.

2.1.2 *Interfaces & Metals*

Experimental work with semiconductors consists in applying voltages and measuring currents, which requires Ohmic contacts. Connecting the experimental apparatus to the semiconductor under study is not a trivial problem, as metal connections to the semiconductor are needed, which can result in Ohmic or Schottky contacts. In addition to that, the semiconductor interface is typically not perfect, and complicated by the presence of Fermi level pinning (Fig. 2.3).

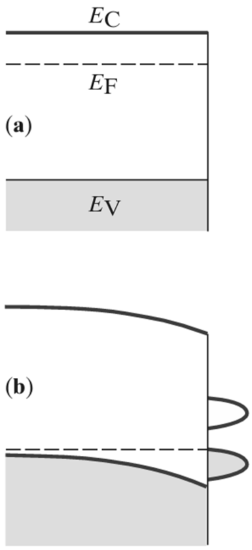

Figure 2.3: Adapted from [18]. **(a)** No Fermi level pinning **(b)** p-type semiconductor presenting Fermi level pinning due to surface states, with downward bending of the electronic bands.

Defects on the semiconductor surface, as well as the surface band structure (if present) modify the local electrostatics, causing band-bending in proximity to the interface. When Ohmic contacts are obtained, they show linear characteristics, and because of this they can be characterized by the contact resistance R_c, specific to the interface.

2.1.3 *Mobility*

The mobility μ represent the response of carriers with charge q to external fields, and is introduced as the proportionality constant between the drift velocity v and the electric field $\vec{\mathbf{E}}$. It is a very important parameter, as in the effective mass approximation it allows to estimate the elastic scattering time $\tau = q/(\mu m^*)$ and the mean free path l_{mfp}:

$$l_{\text{mfp}} = v_F \tau, \tag{2.2}$$

where v_F is the Fermi velocity. The mean free path can be used to understand if in a certain length the transport regime of the device is diffusive, ballistic, or in a cross-over situation between the two limits. Strictly speaking, when a semiconducting transport channel with length L is ballistic, the "classic" mobility is not defined, but it can still be identified an effective mobility from experimental measurements. From this point of view, different methods are used to estimate the mobility, from Hall effect measurements to field-effects measurements. The last method uses the action of an external gate electrode to control the charge inside the semiconducting channel.

2.1.4 *Back gate modulation*

Control of the chemical potential in the semiconductor can be achieved by a capacitive coupling to a metallic gate. There are different types of gate electrodes, and the common factor is the use of electric fields to modify the electro-chemical potential distribution in the space, locally or globally. The naming of a gate electrode is done according to its position with respect to the semiconducting channel (top, bottom, side gates). In this thesis due to the fabrication steps, the gate electrode is positioned under the semiconductor and is called back gate. The specific relation between the charge inside the semiconductor and the back gate voltage requires precise and accurate modeling, as the specific capacitance of the system should be calculated. In addition to that, the induced charge will give an additional (self-)contribution to the electrostatic potential that modifies the action of the back gate, a phenomenon known as screening.

In the system under study, by modulating the electron density inside the semiconductor, the role of the back gate is to modulate the transport properties of the system. To model the back gate modulation, it is important to make some simplifications. The system is a semiconductor nanostructure $\simeq 100\,\mathrm{nm}$ thick coupled to a heavily doped p-type Silicon back gate by $285\,\mathrm{nm}$ of SiO_2. Neglecting screening effects, the charge induced by the back gate is given by $Q = CV_{bg}$. A simple parallel plate capacitor model is used, where the capacitance per unit area is given by:

$$c_{ox} = \frac{\varepsilon\varepsilon_0}{t},$$

where ε is the dielectric constant of the oxide, and t the separation between the electron gas and the back gate. In this way, the induced electron density can be written as:

$$n = \frac{1}{e} c_{ox} \left(V_{bg} - V_{th}\right), \tag{2.3}$$

where the threshold voltage V_{th} has been introduced that takes into account at a phenomenological level the details of the band structure at the interface. An unwanted doping near the surface between the semiconductor and the oxide can in fact deplete or cause accumulation in the semiconductor. For the depletion, before actually inducing charge, a nonzero voltage between the back gate and the channel has to be applied to create flat band alignment. Numerous definitions in the literature are given for V_{th}, each depending on the application [19]. In this thesis it is defined as the voltage at which the back gate starts inducing a nonzero electron density in the channel.

To obtain an expression for the conductance of the semiconductor, expressions for the current and the voltage drop across the device as a function of experimental variables are needed. The semiconducting region between the source and drain electrodes–the contacts used to inject and collect the electrical–is called the semiconducting channel, or simply the *channel*. The current density between the source and the drain electrode is:

$$I_{SD}/W = e\,n\,v, \tag{2.4}$$

where e is the elementary charge and $v = \mu\, E_{\|}$ is the drift velocity, proportional to the longitudinal electric field in the channel. For a small applied voltage V_{SD} between source and drain, a linear voltage drop along the channel length L can be assumed, such that $E_{\|} = V_{SD}/L$ is obtained. In this way, the back gate modulates the conductance of the semiconducting channel $G = I_{SD}/V_{SD}$:

$$G = c_{ox} \frac{W}{L} \mu \left(V_{bg} - V_{th}\right), \tag{2.5}$$

with a "response" that depends on the mobility. When using G vs. V_{bg} curves (the transfer curves) to estimate the mobility, what is obtained is the field-effect mobility. As

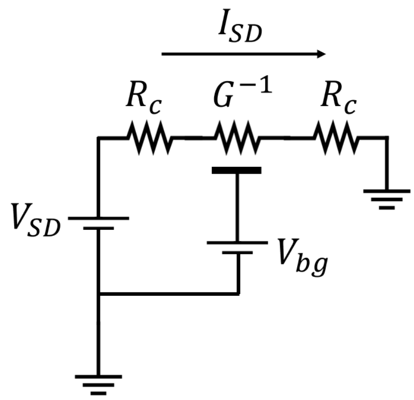

Figure 2.4: Schematics of an experimental setup where the effects of contact resistance must be incorporated into the modeling.

mentioned in Sec. 2.1.3, this procedure is not strictly correct when the device is ballistic. However it is still possible to identify an effective mobility from the transfer curves that corresponds to the "ballistic" mobility [20, 21]:

$$\mu = \frac{L}{W c_o x} \frac{\partial I_{DS}}{\partial V_{bg}} \frac{1}{V_{DS}}$$

V_{bg} represent the back gate voltage with respect to the semiconducting channel. When doing experiments, the source and back gate electrode have common ground, evidenced in the sketch in Fig. 2.4. Having contact resistances R_c between the source and drain electrodes and the semiconductor, changes both the working point of the applied gate voltage $V_{bg,\text{app}}$ and the measured voltage drop $V_{DS,\text{meas}}$ by an amount proportional to the current flowing.

$$V_{DS,\text{meas}} = V_{DS} + 2R_c I_{SD}$$

$$V_{bg,\text{app}} = V_{bg} + R_c I_{SD}$$

In the system under study, because of the order of magnitude of currents, contact resistances, and back gate voltage, (respectively $100\,\text{nA}$, $100\,\Omega$ and $10\,\text{V}$) the effect is negligible as it is at most O($100\,\mu\text{V}$) on applied voltages of order of V.
Instead, it is not negligible when considering the conductance of the channel, as $1/G$ is the same order of R_c. In this case, to model the measured conductance, the two in-series contact resistances need to be included [22]:

$$\frac{1}{G_{\text{meas.}}} = \left(c_{ox} \frac{W}{L} \mu \left(V_{bg} - V_{th} \right) \right)^{-1} + 2R_c \tag{2.6}$$

2.2 Superconductors

Discovered over a century ago by H. Kamerlingh Onnes, superconductivity has kept physicist busy for decades trying to unveil its mysteries, and still today there are a great amount of open questions. Giving a complete description of the basic theory of superconductivity definitely goes beyond the scope of this thesis. To give the right amount of space to the latest developments, I will limit myself discussing the key points of the historical theories, while for a in-depth analysis of the foundations I refer to the textbooks [23], [24].

What Onnes found was that certain metals, when cooled down to liquid Helium temperature, showed a sudden drop in the electrical resistance to the current flow (Fig. 2.5).

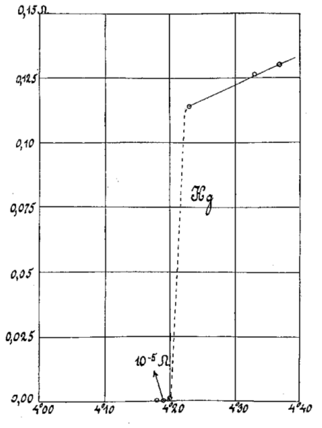

Figure 2.5: Original data of H. Kamerlingh Onnes, displaying the superconducting transition of Mercury.

Later, Meissner and Ochsenfeld discovered an additional properties of these materials: when cooled down to low temperature, they showed a perfect diamagnetic response. In the zero resistance state and exposed to an external magnetic fiel $\vec{\mathbf{H}}$, the samples magnetize in a way to completely screen the magnetic flux density $\vec{\mathbf{B}}$ penetrating the inside (*Meissner effect*).

The first two persons who gave a phenomenological description of these two properties were the London brothers in 1935 [25] who provided a theory that, together with Maxwell's equations, allowed for a qualitative understanding and modeling of these new "superconducting" materials. The model consisted in having a current density $\vec{\mathbf{J}}_\mathrm{s}$ proportional to the vector potential $\vec{\mathbf{A}}$ in a specific (London) gauge.
The proportionality constant, material dependent, controlled how strong the magnetic flux screening was:

$$\vec{\mathbf{J}}_\mathrm{s} = -\frac{1}{\mu_0 \lambda_L^2} \vec{\mathbf{A}} \tag{2.7}$$

Today it is called the London penetration depth, λ_L.

2.2.1 *Ginzburg - Landau Theory*

A step forward in the understanding of superconductivity was made by V. Ginzburg and L. Landau in 1950, who gave a theoretical treatment based on Landau's theory of second order phase transitions. The incredible physical intuition was to introduce a complex order parameter $\psi(\vec{\mathbf{x}})$, the wavefunction of the "superconducting electrons"[2] and related to their density n_s by:

$$n_s(\vec{\mathbf{x}}) = |\psi(\vec{\mathbf{x}})|^2 \tag{2.8}$$

The innovation was that the order parameter ψ, being a complex variable, was described both by an amplitude $\left(\sqrt{n_s}\right)$ and by a *phase*. Using a variational approach on the free energy of the system $F\left[\psi^*, \psi, \vec{\mathbf{A}}\right]$ with $\vec{\mathbf{A}}$ the vector potential, allows to write an equation

[2]This was the term used by Ginzburg and Landau in their original paper [26], since at that time a microscopic picture was missing. Today we know that in bulk superconductors the transport is due to Cooper pairs, which are vompsite bosons, and this wavefunction describes their condensate.

for the superconducting current density ($\delta F/\delta A_i$):

$$\vec{\mathbf{J}}_{\mathbf{s}}(\vec{\mathbf{x}}) = \frac{i\hbar q}{2m^*}\left(\psi^*(\vec{\mathbf{x}})\nabla\psi(\vec{\mathbf{x}}) - \psi(\vec{\mathbf{x}})\nabla\psi^*(\vec{\mathbf{x}}) + \frac{2q}{i\hbar}\left|\psi(\vec{\mathbf{x}})\right|^2 \vec{\mathbf{A}}(\vec{\mathbf{x}})\right), \tag{2.9}$$

recovering the result of the London brothers in a *gauge-invariant* form. Given $\hat{n}$ the normal direction to the surface of the superconductor, and $\vec{\mathbf{M}}$ the magnetization, the boundary conditions that $\hat{n} \wedge \vec{\mathbf{M}} = \vec{0}$, and $\hat{n} \cdot \vec{\mathbf{J}}_{\mathbf{s}} = 0$ impose that superconducting current flows on the surface of the superconductor and not in the bulk, where it would produce a non-zero magnetic flux. Fitting experiments with this theory gave a value for the charge $q = -2e$, but to interpret this numerical result, a microscopic theory was needed.

2.2.2 *Bardeen - Cooper - Schrieffer Theory*

Since this chapter has the scope of providing the base for an understanding of the experimental results, only the essential elements of the BCS theory are provided. The key observation prior to the Bardeen - Cooper - Schrieffer (BCS) theory, was the discovery of the isotope effect [27]. For two isotopes of Mercury (Fig. 2.6) a shift of the critical temperature at different applied magnetic fields was observed, such that:

$$T_c M^\alpha = \text{cost.},$$

with $\alpha \simeq 0.5$. This fact (plus numerous other observations, like heat capacity measurements) lead to the understanding that the interaction between the electrons and the crystal lattice is the reason behind the superconducting transition.[3] In particular, phonons mediate an effective attractive interaction between the electrons, causing an instability in the Fermi surface of the metal and leading to a different ground state for the system which is not anymore a Fermi liquid.

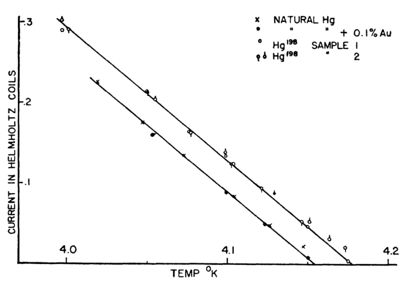

Figure 2.6: Original data from Maxwell [27], showing a shift in the H vs T_c curve between two isotopes of mercury.

The electrons of the system, due to the attractive interaction (pairing mechanism), form Cooper pairs, a combination of electrons with opposite momentum and spin (pairing symmetry). They are bosonic particles and can condense in one macroscopic superconducting ground state $|\Psi_S\rangle$. BCS models the ground state as a superposition of Cooper pairs which can be occupied (with amplitude v_k) or unoccupied (with amplitude u_k):

$$|\Psi_S\rangle = \prod_k \left(u_k + v_k c^\dagger_{k\uparrow} c^\dagger_{-k\downarrow}\right)|0\rangle \tag{2.10}$$

The single-particle excitation spectrum of the system consists of quasiparticle states of energy E_k that are superpositions of electron and holes. The excitation gap at momentum k, Δ_k, is determined self consistently. The spatial extension of the Cooper pairs,

[3] In most materials.

called BCS coherence length ξ_{BCS}, is derived from the uncertainty principle investigating in which region of the k-space ($\xi_{BCS} \simeq 1/\delta k$) the product of the coherence factors $u_k v_k$ is nonzero. In energy, this corresponds to a scale of Δ (the gap) around the chemical potential:

$$\xi_{BCS} = \frac{1}{\pi}\frac{\hbar v_F}{\Delta} = \frac{1}{\pi}\frac{\hbar^2 k_F}{m\Delta} \tag{2.11}$$

In addition to that, for weakly coupled superconductors, it is also possible to relate the zero-temperature gap $\Delta(0)$ to the critical temperature T_c by:

$$\Delta(0) = 1.76 k_b T_c \tag{2.12}$$

The BCS approach to the physics of superconducting systems is valid only for homogeneous systems. The need for describing inhomogeneous systems such as Josephson junctions or superconducting vortices requires further refinement of the theoretical treatment that will be provided in the following sections.

2.3 Superconductor - Semiconductor Heterostructures

The discovery of the Josephson effect in 1962 lead to a revolution in superconductivity, as a connection between various field of physics was made. The original picture of Brian Josephson is to have two superconducting material (S) separated by a small insulating layer (I). If the insulating layer is thin enough, Cooper pairs can tunnel through the barrier, and transport through the insulating layer is made without developing a voltage drop. This effect, called the Josephson effect, was discovered in many other systems very different from the original. In its honor, when two superconductors are linked together by another material, a Josephson junction is formed. Additionally, Josephson provided a physical description of the junctions through two equations. The first equation states that supercurrent I_s flows through a Josephson junction according to the phase difference φ of the order parameter between the two superconductors :

$$I_s = I_c \sin(\varphi), \tag{2.13}$$

where I_c is the critical current, the maximum amount of supercurrent that can flow without developing a voltage drop. The second Josephson equation describes the time evolution of the phase difference φ, when a voltage V is applied across the junction:

$$\frac{d\varphi}{dt} = \frac{2eV}{\hbar} \tag{2.14}$$

In this thesis, SNS Josephson junctions are discussed, in which two superconductors are linked by a normal material with a non-tunnel type conductivity (Fig. 2.7).

The two superconducting electrodes are separated by a distance L, that defines the normal channel length (that can differ from the true effective channel length, $L_{\text{eff}} \geq L$ [28]). Introducing this length scale, Josephson junctions can be ranked in different categories, according to a comparison made with other parameters. The categories that will be relevant for this work are:

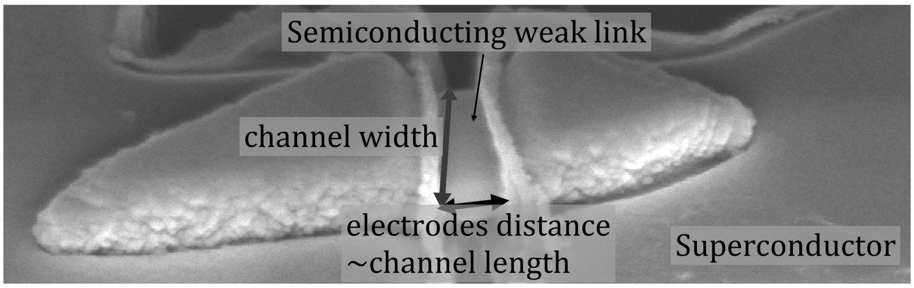

Figure 2.7: Scanning electron micrograph of an SNS Josephson junction.

- Ballistic Junction $L \ll l_{\text{mfp}}$: this transport regime happens when length of the normal material is smaller than the elastic scattering length. In the opposite situation, the regime is called diffusive.
- Short Junction (ballistic case) $L \ll \xi$: the normal region is much shorter than the coherence length, calculated for example through the BCS formula in eq. 2.11. In the opposite situation, the "long Junction" regime is obtained.

Since SNS junctions are a type of inhomogeneous systems, BCS theory cannot be used in their theoretical description, and a first approach can consist in using the Ginzburg-Landau theory, which:

- Is strictly correct only for $T \simeq T_c$
- Does not take into account quasiparticle excitations that actively contribute to transport properties.

A more complete treatment to the physics of these systems is provided by the Bogoliubov de Gennes (BdG) formalism, extending the space independent BCS Hamiltonian to a space dependent , allowing to have insights in the energy spectrum of the SNS junctions.

2.3.1 *Bogoliubov - de Gennes Hamiltonian*

To have a space dependent description of the superconducting coupling, the starting point is the BCS Hamiltonian [29]:

$$H_{\text{BCS}} = \sum_{\mathbf{k},\sigma} \xi_{\mathbf{k}} c^{\dagger}_{\mathbf{k}\sigma} c_{\mathbf{k}\sigma} - \sum_{\mathbf{k}} \mathbf{\Delta}^{*}_{\mathbf{k}} c_{-k\downarrow} c_{k\uparrow} - \sum_{\mathbf{k}} \mathbf{\Delta}_{\mathbf{k}} c^{\dagger}_{k\uparrow} c^{\dagger}_{-k\downarrow} + \text{const.}, \tag{2.15}$$

where $\xi_{\mathbf{k}}$ is the energy of the electron with momentum $\mathbf{k}$ with respect to the Fermi level and $\mathbf{\Delta}_{\mathbf{k}}$ is the energy gap at momentum $\mathbf{k}$ that is needed to excite quasiparticles from the BCS ground state (measured from the Fermi level). Introducing the Nambu spinor base:

$$|\Psi_{\mathbf{k}}\rangle = \begin{pmatrix} c^{\dagger}_{k\uparrow} \\ c_{-k\downarrow} \end{pmatrix} |\Psi_S\rangle \,, \tag{2.16}$$

and rewriting the BCS Hamiltonian in this base gives the BdG Hamiltonian:

$$H_{\text{BdG}}(\mathbf{k}) = \begin{pmatrix} \xi_{\mathbf{k}} & -\mathbf{\Delta}_{\mathbf{k}} \\ -\mathbf{\Delta}^{*}_{\mathbf{k}} & -\xi_{\mathbf{k}} \end{pmatrix} \tag{2.17}$$

The off-diagonal terms represent the superposition of electrons and holes and are key in the description of the quasiparticle excitations of the system. The real space description is obtained by a Fourier transform:

$$H_{\text{BdG}}(\mathbf{r}) \equiv \frac{1}{N}\sum_{\mathbf{k}} e^{i\mathbf{k}\cdot\mathbf{r}} H_{\text{BdG}}(\mathbf{k}) = \begin{pmatrix} H_0(\mathbf{r}) & -\mathbf{\Delta}(\mathbf{r}) \\ -\mathbf{\Delta}^*(\mathbf{r}) & -H_0(\mathbf{r}) \end{pmatrix}, \tag{2.18}$$

where $H_0(\mathbf{r})$ is the single-electron Hamiltonian. $H_0(\mathbf{r})$ can be tuned to account for the information specific to the systems under modeling. More specifically, this information can be encoded in the potential $V(\mathbf{r})$:

$$H_0(\mathbf{r}) = -\frac{\hbar^2}{2m}\nabla^2 - \mu + V(\mathbf{r}) \tag{2.19}$$

The eigenvalue equation of the Bogoliubov - de Gennes Hamiltonian is called Bogoliubov - de Gennes equation:

$$H_{\text{BdG}}(\mathbf{r})\Psi(\mathbf{r}) = E\ \Psi(\mathbf{r}), \tag{2.20}$$

and can be used to explicitly treat interfaces between normal and superconducting materials, providing a theoretical method to investigate the excitation spectrum of SNS Josephson junctions.

2.3.2 *(Multiple) Andreev Reflections*

To understand the charge transport process in these hybrid systems, the single SN interface has to be studied. The first treatment was done by Andreev in 1964 [30], who discovered that when an electron (hole) coming from the N material is impinging on a superconductor, if its energy lies in the superconducting gap where no single particle states are available ($|E| < \Delta$), then is reflected as a hole (electron), flipping the spin and with opposite momentum.[4] For sub-gap energies, the Andreev reflection (AR) process transfers a charge of $2e$ into the superconductor, giving a mechanism of current flow through these interfaces (Fig. 2.8). In the opposite case, when electrons carry an energy $|E| > \Delta$, they can directly enter the superconductor as Bogoliubov quasiparticles, without undergoing AR.

Mathematically, this process is derived by looking at the solutions at energy $|E| < \Delta$ of the BdG equations for a pair potential given by $\mathbf{\Delta}(\mathbf{r}) = \Delta\Theta(x)$. Since only one superconductor is involved, there is no necessity in specifying the phase in the order parameter. The Nambu spinor solution of the eigenvalue problem in the normal material, for an impinging electron with momentum $\mathbf{k_I} = (k_x, k_y, k_z)$ is:

$$\Psi(\mathbf{r}) = \begin{pmatrix} e^{i\mathbf{k_I}\cdot\mathbf{r}} + re^{i\bar{\mathbf{k}}\cdot\mathbf{r}} \\ ae^{i\mathbf{k_H}\cdot\mathbf{r}} \end{pmatrix}, \tag{2.21}$$

and consist in reflected electrons with amplitude r carrying the same momentum parallel to the interface $\bar{\mathbf{k}} = (-k_x, k_y, k_z)$, and in holes with $\mathbf{k_H} = (k_{hx}, k_y, k_z)$.

[4]Possessing opposite charge and momentum, the contribution of a hole to the current is in the same direction of the electron's contribution, and viceversa.

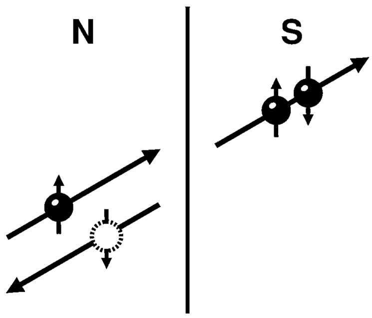

Figure 2.8: Schematic of the Andreev Reflection process: An electron (filled circle) impinging from the left to the NS interface is flipped into a hole (empty circle) with opposite spins and momentum, leading to a $2e$ charge transfer into the superconductor.

In the superconductor, the solutions are evanescent quasiparticle states that cannot contribute to charge transport. It is found that if $\Delta \ll E_F$, then $k_{hx} \simeq k_x$ and since the second component of the Nambu spinor (eq. 2.16) is given by $c_{-k\downarrow}$, it represents a hole with opposite momentum, thus carrying negative current as do the electrons.

In reality, interfaces present defects that serve as scattering centers for normal reflections. Even if the interface is very clean, the discontinuity in the Fermi velocity between the materials effectively creates a scattering center for normal reflections. To take into account these effects, Blonder Tinkham and Klapwijk (BTK) [31] considered a step pair potential but with the addition in the single-electron Hamiltonian of a delta barrier of height $Z\hbar^2 k_F^2/m$. The Z parameter is related to the transparency of the interface through:

$$T = \frac{1}{1+Z^2} \tag{2.22}$$

The BTK model explicitly calculates the probability of different scattering processes as a function of the Z parameter, as given in Fig. 2.9. When there is a barrier at the interface, the probability of Andreev reflection (curve A) is suppressed with respect to the probability of undergoing normal reflection (curve B).

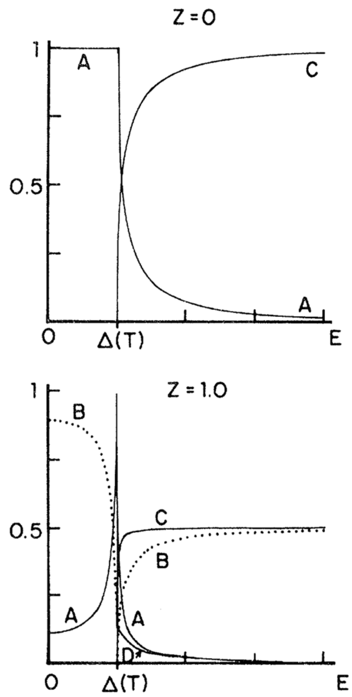

Figure 2.9: Reflection amplitudes in the BTK model for two values of the Z parameter. A: amplitude of Andreev reflection, B: amplitude of normal reflection. Adapted from [31].

SNS junctions present two SN-interfaces, and for sub-gap energies electrons and holes are allowed to undergo the AR process at each interface, providing a direct transport mechanism of Cooper pairs between the two superconductors. If an electric field (equivalently, a voltage difference V) is present, in traversing the channel electrons and holes are accelerated, gaining energy. Carriers in the channels keep undergoing AR processes until $|E| > \Delta$, where the probability of AR decreases (Fig. 2.9), and they can enter the superconductor as single-particle excitations. This process, known as Multiple Andreev Reflection (MAR), is represented in the left image of Fig. 2.10. It can be experimentally probed by looking at the differential conductance as a function of the voltage difference of the junction. The differential conductance presents a complex structure, with several resonant features. When these features appear at voltages $e|V| < 2\Delta$, they are called Subharmonic Gap Structures (SGS), and the current interpretation of Multiple Andreev Reflections was given by BTK, with a refined model by Octavio & BTK. [32, 33] In their model, the resonant structures appear at specific subgap voltages:

$$eV_n = \frac{2\Delta}{n}, \tag{2.23}$$

and follow a harmonic series. n is the number of Andreev reflection process taking place for that resonant voltage. In the left image of Fig. 2.10, a process with $n = 6$ is displayed.

So far, the physics discussed regarded a step-like pair potential, in which the superconducting region was independent from the normal region. Due to finite de-phasing and scattering times, when the electrons of a Cooper pair trespass the boundary between the S and the N region, the pairing (opposite spin and momentum) is kept for some time before randomization. At this point there are two electrons in the normal material that are effectively paired near the boundary, inducing correlations in the normal material and a superconducting gap Δ^*, weaker and different from the original. This is called proximity effect[5] and its effects can be seen in the subharmonic gap structures of the differential conductance. The induced gap Δ^*, allows for new resonant scattering processes at the interfaces between the Δ and Δ^* region, as depicted in the central and right images in Fig. 2.10. [34]. How the subharmonic gap structures appear in the dif-

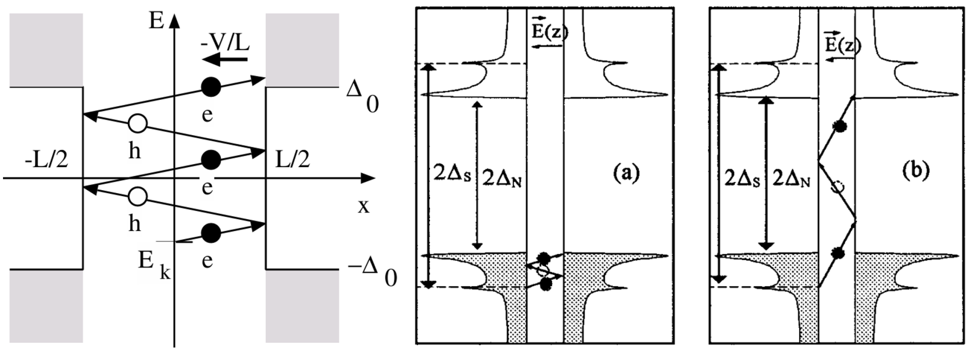

Figure 2.10: From the left: MAR in a SNS junction, showing $n = 6$ Andreev reflections (Adapted from [35]). MAR process at (a) $eV_n = (\Delta - \Delta^*)/3$ and (b) $eV_n = (\Delta + \Delta^*)/3$, 3 is the number of Andreev reflections. Adapted from [34]

ferential conductance depends explicitly on the quality of the interface. This is relevant because from the experimental point of view, an incorrect attribution of the subharmonic

[5]The opposite is also true and is called inverse-proximity, but for large superconducting banks can be neglected.

gap structures features to the harmonic series of MAR leads to a wrong estimation of the induced gap. Simulations of IV curves and differential conductance as a function of the interface transparency have been performed [36, 34] which show a transition from peaks to dips at high interface transparencies, underlining the pivotal role of MAR spectroscopy in characterizing and understanding the physics in SNS Josephson junctions.

2.3.3 *Andreev Bound States*

If there is a voltage difference between the superconducting electrodes, carriers in the N region can undergo up to $n \simeq eV_n/2\Delta$ Andreev reflections before being injected in the electrodes. If no voltage difference is developed between the electrodes, electrons and holes are allowed to undergo AR indefinitely, without being injected as a single particle excitation in the superconductor. Andreev reflections are a coherent process, and quantum interference between the electron and hole trajectories leads to the formation of discrete energy levels, in a similar way of what happens in an optical cavity. These levels are called Andreev Bound States (ABS) and since provide a charge tranfer mechanism when no voltage drop is developed, they are responsible for carrying the supercurrent in SNS structures.

A toy model used to understand the formation of these discrete energy levels in SNS junctions is to consider the pair potential in the electrodes to be given by $\Delta e^{i\varphi_L}$ for the left electrode and by $\Delta e^{i\varphi_R}$ for the right electrode. For energies within the superconducting gap ($|E| < \Delta$), no single-particle states are present in the S-electrodes, and exponentially decaying solution are formed, like in the AR process. In the normal material, the solution to the BdG equation can be written as a superposition of counter-propagating electron-like and hole-like states. Matching the solutions at the boundary gives the energy spectrum [37]:

$$\frac{\varepsilon}{|\Delta|} = (-1)^m \cos\left(\frac{L}{\xi_{\text{BCS}}}\frac{\varepsilon}{|\Delta|} + \frac{\varphi}{2}\right), \tag{2.24}$$

where L is the effective length of the normal region, φ is the superconducting phase difference between the two banks, and m can be 0 or 1. In reality, the spectrum of these excitations can be much different from the solutions of eq. 2.24, and the details of the system must be taken into account. Explicit treatment of spin-orbit coupling and magnetic fields in the Bogoliubov de Gennes equations has been performed, and spinful ABS as well as Zeeman-splitted ABS have been reported [38, 39].

For an SNS short junction ($L \ll \xi$) having N modes with transmission τ_i and conductance $G = 2e^2/h \sum_i \tau_i$, by using the BdG formalism it can be shown that the energy of the ABS is given by [40]:

$$E_j(\varphi) = \pm\Delta\sqrt{1 - \tau_j \sin{(\varphi/2)}^2}, \tag{2.25}$$

where the $\pm$ symmetry follows from the particle-hole symmetry underlying the theory, and each mode contributes to the formation of a pair of ABS. This simple model highlights how the energy of the ABS depends on the phase difference of the superconducting banks, a property that is key in understanding how they contribute to the current flow, by transferring Cooper pairs between the superconductors.

2.3.4 *Current Phase Relationship in SNS weak links*

The current phase relationship (CPR) in a Josephson junction connects the supercurrent flowing through the junction to the phase difference φ of the superconducting leads. It follows directly from the free energy:

$$I = \frac{2e}{\hbar}\frac{dF}{d\varphi} \tag{2.26}$$

and from its expression in terms of the excitation spectrum it is possible to write general relations between the current and the phase [41]. Since Andreev Bound States are responsible for carrying the supercurrent in SNS Josephson junctions, their energy dispersion (the excitation spectrum) contains all details required to calculate the CPR, and experimentally it has been demonstrated to be a viable strategy to obtain that information [14].

If the excitation spectrum is known, the supercurrent $I(\varphi)$ is the sum of three components:

$$I_1 = -\frac{2e}{\hbar}\sum_p \tanh\left(\frac{\varepsilon_p}{2k_bT}\right)\frac{d\varepsilon_p}{d\varphi} \tag{2.27}$$

$$I_2 = -\frac{2e}{\hbar}2k_bT\int_\Delta^\infty d\varepsilon \ln\left[2\cosh\varepsilon/(2k_bT)\right]\frac{d\rho}{d\varphi} \tag{2.28}$$

$$I_3 = \frac{2e}{\hbar}\frac{d}{d\varphi}\int d\mathbf{r}|\Delta|^2/|g| \tag{2.29}$$

The I_1 term follows from the discrete (ABS) spectrum, with sub-gap energies $\varepsilon_p \in (0, \Delta)$. The second contribution, I_2, is given by the continuum quasiparticle spectrum, which has a density of states ρ. The third contribution, present only for a phase dependent amplitude of the energy gap Δ, is usually neglected in the short junction limit. This theoretical method of calculating the CPR, not strictly related to SNS Josephson junctions, has demonstrated to be useful in studying the nontrivial physics of these superconducting-semiconducting hybrids, from spontaneous supercurrents to superconducting diode effects, and also to propose new devices. [42, 43, 44]. By making several assumptions on the transport properties of the device under study, several different types of CPR are obtained [45]. Each ABS carries a current:

$$I(\varphi) = 2ef_0\left[E(\varphi)\right]\frac{d}{d\varphi}E(\varphi), \tag{2.30}$$

proportional to the derivative of its energy dispersion and to its occupation, described by a Fermi-Dirac distribution. The most important property follows directly: since a pair of bound states at fixed phase have opposite energy (due to electron-hole symmetry) then each of those carries supercurrent in the opposite direction.[6] Net supercurrent transport across the SNS junction happens only if there is an unbalance in the occupation of the

[6] Each ABS of the pair can carry supercurrent in both directions. At a fixed phase difference φ they carry opposite current.

two states.

At zero-temperature, where the occupation is simply a step function, by summing over each ABS the following CPR is obtained:

$$I\left(\varphi\right)=\sum_{j}\left(\frac{\tau_{j}e\Delta}{h}\right)\frac{\sin\varphi}{\sqrt{1-\tau_{j}\sin\left(\varphi/2\right)^{2}}},\tag{2.31}$$

where it is highlighted that all ABS at negative energy are occupied while the positive energy ABS are unoccoupied, giving net supercurrent transport. At finite temperature, the CPR decays due to thermal occupation of the higher energy ABS. Explicit calculation with the derivative of the Fermi-Dirac distributions (eq. 2.30) gives the following, general case, CPR:

$$I\left(\varphi\right)=\frac{e\Delta^{2}}{2\hbar}\sum_{j}\frac{\tau_{j}\sin\varphi}{E_{j}}\tanh\frac{E_{j}}{2k_{b}T}\tag{2.32}$$

From this expression, several limits (diffusive, ballistic, ..) can be considered to derive specific-case relations.

2.3.5 *Dynamics of the single Josephson junction: RCSJ model*

Microscopic models, even if they provide an accurate picture of the devices, are cumbersome to use and provide only an equilibrium description of the properties of the system. Circuit effective models come to help in giving a first understanding of the dynamics of current flow through Josephson junctions.

To this end, the Resistively and Capacitively Shunted Junction (RCSJ) model is widely used to model the dynamics of a Josephson junction [46]. In this model, the physical Josephson junction is represented by the electrical parallel connection of three elements: a resistor (R), a capacitor (C), and a Josephson element with CPR $I\left(\varphi\right)$. In the common version, the ideal Josephson element with a sinusoidal CPR is used. The resistor accounts for the normal-state resistance and for quasiparticle current, the capacitor represents the junction's capacitance and displacement current, and the CPR describes the supercurrent flow. In addition to that, a thermal current noise component can be included in the model to take into account the finite temperature:

$$I=I(\varphi)+\frac{V}{R}+C\frac{dV}{dt}+\delta I_{th}\tag{2.33}$$

To keep the formalism simple at an analytical level, a sinusoidal CPR $I(\varphi)=I_0\sin\varphi$ is used, while for the more general case a numerical approach is needed. Neglecting thermal noise and using the Josephson equation, repeated here for convenience:

$$\frac{\partial\varphi}{\partial t}=\frac{2e}{\hbar}V,\tag{2.34}$$

it is possible to obtain:

$$\frac{I}{I_0}=\sin\varphi+\frac{d\varphi}{d\tau}+\beta_C\frac{d^2\varphi}{d\tau^2},\tag{2.35}$$

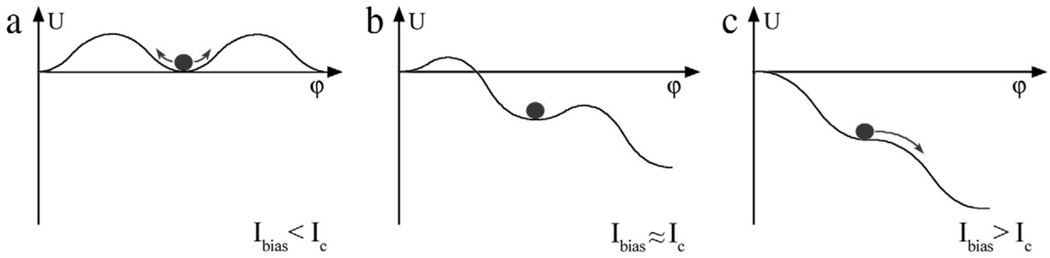

Figure 2.11: The motion of a particle in a tilted washboard potential. The change of phase difference across a Josephson junction shows an analogous behavior. Taken from [46].

where the reduced time $\tau = [h/(2eI_0R)]t$, and the hysteresis parameter $\beta_C = 2\pi I_0 C R^2$ have been introduced. The equation written above is formally equivalent to the motion of a "phase" particle in a tilted washboard potential $U(\varphi) \propto (1 - \cos\varphi + (I/I_0)\varphi)$. The position of the particle corresponds to the phase, and the tilt of the washboard is proportional to the applied current, as displayed in Fig. 2.11.

When the current is below a critical value, the phase particle is trapped in one of the potential wells. In this case $\dot{\varphi} = 0$, and by 2.34, corresponds to $V = 0$ for $I \neq 0$: the superconducting state. When $I > I_0$, the tilt is such that $\dot{\varphi}$ is always nonzero, giving a voltage difference across the junction: the dissipative state. When thermal fluctuations are taken into account [47], even if $I < I_0$, the phase particle can gain enough energy to escape from the well and being trapped in another, leading to a premature switching event. The premature switching is understood by using eq. 2.34: if $\dot{\varphi} \neq 0 \Rightarrow V \neq 0$. The rate of thermal excitations increases with temperature, as higher temperatures provide more thermal energy to the phase particle, up to a point at which even for $I < I_0$, there is always a finite voltage difference, since $\langle\dot{\varphi}\rangle \neq 0 \Rightarrow \langle V\rangle \neq 0$.

The RCSJ phenomenological model does not take into account phenomena like the quantum tunneling of the phase particle or Multiple Andreev Reflections in the resistive state, but even if with some limitations, it still represents a very useful instrument in having a clear picture of physics of the junction.

2.3.6 *Single junction interference*

The order parameter in a superconductor is characterized by an amplitude and a phase $\mathbf{\Delta}(\mathbf{r}) = \Delta(\mathbf{r})e^{i\varphi(\mathbf{r})}$ which both are in free to vary in space. In the Josephson junction treatment given so far, the SNS junction was modeled as one-dimensional, neglecting the finite area of the weak link. When a magnetic field is applied perpendicularly to a Josephson junction, and if the supercurrent distribution in the channel is uniform, then the critical current presents an interference pattern, resembling that found in single-slit

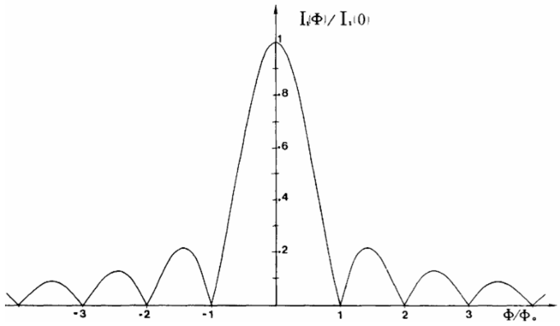

Figure 2.12: Theoretical magnetic field dependence of the maximum supercurrent for a rectangular junction with uniform supercurrent density. Adapted from [47].

optical experiments, and called Fraunhofer pattern,[7] described by:

$$I(\Phi_{\rm JJ}) = I_c \sin\left(\pi\frac{\Phi_{\rm JJ}}{\Phi_0}\right)\frac{1}{\pi\frac{\Phi_{\rm JJ}}{\Phi_0}}, \tag{2.36}$$

where $\Phi_{\rm JJ}$ is the magnetic flux enclosed by the junction. The theoretical Fraunhofer interference pattern is displayed in Fig. 2.12. From an experimental point of view, the shape of the interference pattern can be used to deduce the supercurrent spatial distribution in the junction [48]. It can be in fact shown that the supercurrent density spatial distribution is the Fourier transform of the interference pattern. By employing the inverse Fourier transform, it is possible to retrieve the supercurrent density distribution from the measured critical current modulation. However, the shape of the interference pattern does not always resemble what shown in Fig. 2.12 [49, 50]. In both ballistic and diffusive junctions, the period of the critical current interference pattern changes continuously as the length-to-width ratio of the junction increases or as the temperature decreases [51] and deviations from the expected Fraunhofer pattern are often reported.

2.4 Superconducting Quantum Interference Devices

Superconducting QUantum Interference Devices (SQUIDs) are a class of superconducting devices that combine the physics of two phenomena: the Josephson effect and flux quantization. Over the years, many kinds of SQUIDs were realized and proposed [52, 53], with different superconductors, weak links, and principles of working. In this thesis I discuss *dc*-SQUIDs, the variant in which two Josephson junctions are connected in a superconducting loop and operated by sending a constant current (*current biasing*) while measuring the voltage drop across the device.

2.4.1 *Flux Quantization*

Flux quantization in superconductors is a fundamental phenomenon arising from the quantum nature of the superconducting order parameter. There are different ways

[7] also called Fraunhofer "diffraction" pattern.

in which flux quantization can be derived, and one of the simplest is to use the Ginzburg-Landau formalism.

Consider a superconductor with a hole. The hole can be physical, e.g., in a ring geometry, or can be a part of the material that is not in the superconducting phase. Flux quantization states that the magnetic flux in the ring must be an integer multiple of a fundamental constant:

$$\Phi = n\frac{h}{2e} \tag{2.37}$$

The fundamental constant, $\Phi_0 = \frac{h}{2e}$, is called superconducting flux quantum: $\Phi_0 \simeq 2.069\,\mu\mathrm{m}^2\ \mathrm{mT}$. The quantization occurs because the macroscopic wave function, being associated with an observable, must be single-valued and continuous. More specifically, by integrating the supercurrent given by eq. 2.9 on a closed loop, the following relation is obtained:

$$\oint_C (\Lambda \mathbf{J_s}) \cdot d\mathbf{l} + \int_S \mathbf{B} \cdot ds = n\Phi_0 \tag{2.38}$$

called fluxoid quantization condition. Since supercurrents flow on the surface, if the path is taken deep in the bulk, a strict quantization of the magnetic flux is obtained. In the following, this assumption will be assumed to always hold, i.e., all superconductors are thick enough to neglect the first term in eq. 2.38.

2.4.2 *Supercurrent Interference*

The dc-SQUID (for the rest of the thesis, SQUID), shown in Fig. 2.13 (a), consist in connecting in parallel two Josephson junctions in a loop. Each junction is characterized by the superconducting phase difference of the order parameter φ_1, φ_2. The loop, with inductance L, encloses a magnetic flux Φ. The fluxoid quantization condition of eq. 2.38, when applied to the superconducting loop , allows to related the phase difference φ_1 and φ_2 according to how much flux is penetrating the loop Φ.

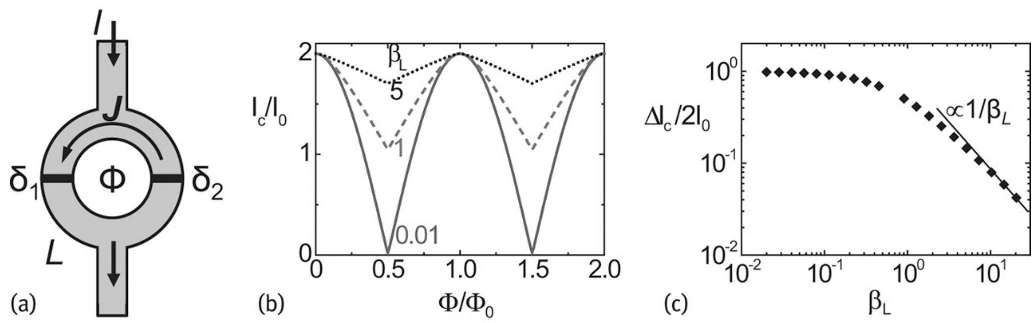

Figure 2.13: **(a)**, sketch of a SQUID in which a current bias of $\mathbf{I}$ is performed. The two phase drops δ_1 and δ_2 are connected by the flux quantization condition. Unbalance in the supercurrents between the two arms result in a screening current $\mathbf{J}$. **(b)** The minima in the interference pattern are lifted to a finite current value in case of non-negligible inductance. **(c)** Effect of β_L on the inteference pattern modulation normalized by the critical current of a symmetric SQUID.

$$\varphi_1 - \varphi_2 = 2\pi \frac{\Phi}{\Phi_0} \tag{2.39}$$

A current J circulating in the loop, due to the inductance L, generates an additional contribution to the flux :

$$\Phi = \Phi_{\text{ext}} + LJ \tag{2.40}$$

The current J is called the screening current and can be related to the current flowing in each arm by $J = I_1 - I_2$. The physical interpretation of the screening current is that the current flow in the loop can be seen as two arms carrying an equal amount of current $(I_1 + I_2)/2$ with a superimposed circulating (screening) current, that gives a positive contribution in one arm and negative in the other.

When applying a transverse magnetic field such that $\Phi \neq 0$ in the loop, the phase drops across the junctions are not independent. If a sinusoidal CPR is assuemd, the current through the loop can be written as:

$$I(\varphi_1, \varphi_2) = I_{c1} \sin \varphi_1 + I_{c2} \sin \varphi_2,$$

then, by using eq. 2.39 and maximizing on φ_1, the critical current of the SQUID is modulated in a periodic pattern :

$$I_c(\Phi) = \sqrt{(I_{c1} - I_{c2})^2 + 4I_{c1}I_{c2} \cos\left(\pi \frac{\Phi}{\Phi_0}\right)^2} \tag{2.41}$$

This effect, called superconducting quantum interference, leads to total suppression of the superconducting behavior ($V = 0$ for $I \neq 0$) when the two arms have equal critical current I_c. For simplicity, suppose that the loop inductance is negligible: when half flux quantum is applied, such that the two phase drops are shifted by π (eq. 2.39), then for every value of the phase no *net* supercurrent flows through the device:

$$I(\varphi_1, \varphi_1 - \pi) = I_c \sin(\varphi_1) + I_c \sin(\varphi_1 - \pi) = I_c \sin(\varphi_1) - I_c \sin(\varphi_1) = 0,$$

causing total destructive interference. When the two junctions possess different critical currents, the amplitude of the smaller one cannot cancel the other, leading to a minimum supercurrent of $|I_{c1} - I_{c2}|$. A similar effect is provided by finite inductance, as displayed in Fig. 2.13 (b). In this case, to understand how much the two phases are related by the flux quantization condition, the screening parameter is introduced:

$$\beta_L = \frac{2LI_c}{\Phi_0} \tag{2.42}$$

For large screening parameters, the critical current vs flux curve (*interference pattern*) show little modulations, estimated at first order by $\Delta I_c / I_c = 1/(1 + \beta_L)$. Furthermore, the relation between the applied and effective flux in the loop is solution to the nonlinear equation (written for the case $I_{c1} = I_{c2}$):

$$\frac{\Phi}{\Phi_0} = \frac{\Phi_{\text{ext}}}{\Phi_0} + \beta_L \cos\left(\frac{1}{2}(\varphi_1 + \varphi_2)\right) \sin\left(\frac{\Phi}{\Phi_0}\right) \tag{2.43}$$

that can be derived by imposing the flux quantization condition on the Φ vs. Φ_{ext} relation. Even for a symmetric SQUID with $I_{c1} = I_{c2}$, for $\beta_L = 1$ the critical current modulates at maximum by 50%.

To estimate to which extent this effect is important, a calculation of the total inductance of the loop is needed. This typically contains two contributions: one geometrical and one "kinetic". The kinetic inductance is a contribution to the inductance caused by the inertia of Cooper pairs.[8] Cooper pairs have finite mass and thus exhibit inertia when they accelerate. This inertia creates an additional inductive effect, which is particularly significant at high frequencies or in thin superconducting films. The kinetic inductance can be understood as the energy stored in the motion of the charge carriers, analogous to the energy stored in the magnetic field of a conventional inductance. This effect is crucial in the design of superconducting devices, not only SQUIDs but also resonators and detectors, where it can influence the device's performance and frequency response. For a superconducting wire of length l, width W, and thickness t, it can be estimated by the following formula [54]:

$$L_K = \frac{\mu_0 \lambda_L^2 l}{Wt} \tag{2.44}$$

As a rule of thumb, it is relevant only when the thickness of the superconducting strips are comparable to or smaller than the London penetration depth λ_L.

2.4.3 *Normal State Conductance of a SQUID based on SNS junctions*

If a SQUID is realized from SNS Josephson junctions with a 2D-semiconducting normal material, then the normal resistance can be modeled by using eq. 2.6, which also includes the interface between the superconducting metal and the semiconductor. In this case, the model for the semiconducting channel can be used, which is reported here for convenience:

$$\frac{1}{G_{\text{JJ}}} = \left(c_{ox} \frac{W}{L} \mu \left(V_{bg} - V_{th} \right) \right)^{-1} + 2R_c \tag{2.45}$$

For two Josephson junctions in parallel, i.e., the case of dc-SQUIDs, the total conductance is the sum of eq. 2.45 for the two junctions, which is plotted in Fig. 2.14:

$$G_{\text{SQUID}} = G_{\text{JJ},1}(V_{th,1}, \mu_1, R_c) + G_{\text{JJ},2}(V_{th,2}, \mu_2, R_c) \tag{2.46}$$

2.4.4 *SQUID interference at high magnetic fields*

The single junction Fraunhofer pattern was briefly introduced in Sec. 2.3.6. When two junctions are connected in parallel and when the magnetic field applied is such that Φ_{J1}/Φ_0, Φ_{J2}/Φ_0 , and $\Phi_{\text{loop}}/\Phi_0$ are non negligible, the interference effect of the SQUID superimpose with the one of the Fraunhofer giving a non trivial shape of the interference pattern [55, 56, 57].

[8] This contribution to the inductance is not restricted to superconducting strips, but it is usually neglected in metal wires at low frequency.

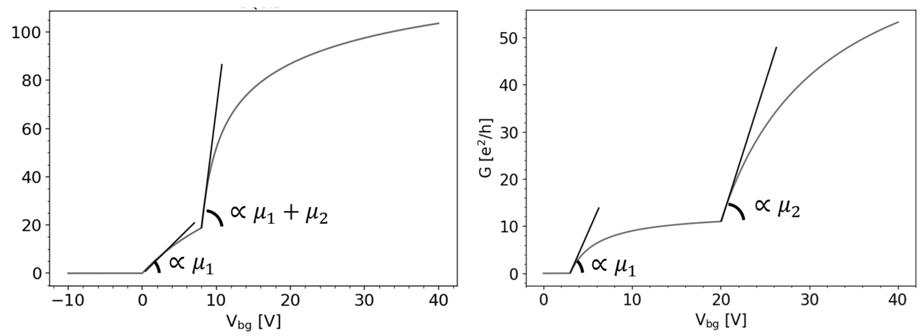

Figure 2.14: **Left:** Model of the conductance of a SQUID. The parameters used are $V_{th,1} = 0\,\text{V}$, $V_{th,2} = 8\,\text{V}$; $\mu_1, \mu_2 = 4000, 10\,000\,\text{cm}^2\text{V}^{-1}\text{s}^{-1}$; $R_{c1} = R_{c2} = 200\,\Omega$. For little difference in the voltage thresholds, the conductance at the upper threshold has a slope which is proportional to the sum of the effective mobilities. **Right:** The parameters used are $V_{th,1} = 3\,\text{V}$, $V_{th,2} = 20\,\text{V}$; $\mu_1, \mu_2 = 5000, 2000\,\text{cm}^2\text{V}^{-1}\text{s}^{-1}$; $R_{c1} = 1000\,\Omega, R_{c2} = 200\,\Omega$. For very different voltage thresholds, the slope of the conductance at the upper threshold is proportional only to the effective mobilities of one junction.

To calculate the interference patterns of a SQUID where also the flux over each junction has a contribution, I use the Ginzburg-Landau formalism. In the case of a sinusoidal CPRs, following the derivation of the Fraunhofer formula [47] and applying the fluxoid quantization condition (eq. 2.38), it is possible to plot the critical currents of SQUID in four cases. The pedagogical derivation is out of the scope of this work, and I limit myself in reporting the result of the calculation:

$$J_1 = J_{c1} \sin\left(\Delta\varphi_{11} + \pi\frac{\Phi_{J1}}{\Phi_0}\right) \frac{1}{\pi\frac{\Phi_{J1}}{\Phi_0}} \sin\left(\pi\frac{\Phi_{J1}}{\Phi_0}\right) \tag{2.47}$$

$$J_2 = J_{c2} \sin\left(\Delta\varphi_{11} + \pi\frac{\Phi_{J2}}{\Phi_0} + 2\pi\frac{\Phi_{\text{loop}}}{\Phi_0}\right) \frac{1}{\pi\frac{\Phi_{J2}}{\Phi_0}} \sin\left(\pi\frac{\Phi_{J2}}{\Phi_0}\right) \tag{2.48}$$

$$J_c = \max_{\Delta\varphi_{11}} (J_1 + J_2) \tag{2.49}$$

J_1 and J_2 are the current density flowing through the two SQUID arms. The phase $\Delta\varphi_{11}$ is a reference phase.[9] The results are displayed in Fig. 2.15, for four limiting cases, as listed below:

The four cases are the following:

- Panel (a): Two Josephson junctions with equal critical current density (in arbitrary units) and equal area: $J_{c1} = J_{c2} = 1$, $A_1 = A_2 = 0.1\,\mu\text{m}^2$. The loop area is 10 times larger than the area of the junctions: $A_{loop} = 1\,\mu\text{m}^2$. In this case the SQUID ("rapid") oscillations are visible with the envelope being modulated by the Fraunhofer pattern.

[9] Similarly to the SQUID, it is irrelevant where the reference phase is taken. For the SQUID, it is possible to obtain the critical current by maximizing the supercurrent with respect to the phase on a junction of choice. In this case, other than specifying a junction of choice, I have specified a position on the junction. To the calculation of the critical current, in the Ginzburg Landau formalism, it is irrelevant where is taken.

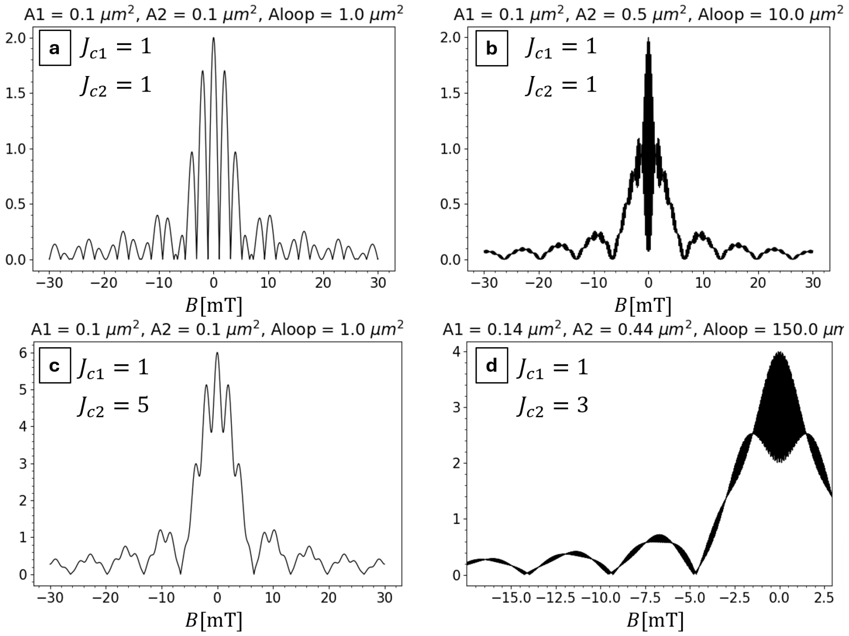

Figure 2.15: **(a)-(d)** Calculated interference patterns at high magnetic fields for SQUID with sinusoidal CPRs for different ratios of critical current densities and areas. The critical current densities are in arbitrary units.

- Panel (b): Two Josephson junctions with equal critical current density but different area: $J_{c1} = J_{c2} = 1$, $A_1 = 0.1\,\mu\mathrm{m}^2, A_2 = 0.5\,\mu\mathrm{m}^2$. The loop area is much larger than the area of the junctions: $A_{loop} = 10\,\mu\mathrm{m}^2$. The SQUID oscillations are very dense with respect to the modulations due to both the Fraunhofer patterns. Even if the SQUID is made with two junctions with the same critical current density, the different areas are such that the interference pattern modulates completely to zero only if $\Phi_{\mathrm{J}_1}/\Phi_0$, $\Phi_{\mathrm{J}_2}/\Phi_0$, and $\Phi_{\mathrm{loop}}/\Phi_0$ are integer numbers at the same time.

- Panel (c): Two Josephson junctions with equal area but different critical current density $A_1 = A_2 = 0.1\,\mu\mathrm{m}^2$, $J_{c1} = 1, J_{c2} = 5$. In this case the interference pattern modulates to zero only if $\Phi_{\mathrm{J}_1}/\Phi_0$ (that is equivalent to $\Phi_{\mathrm{J}_2}/\Phi_0$) is an integer.

- Panel (d): Two Josephson junctions with different area and different critical current density. $J_{c1} = 1, J_{c2} = 3$, $A_1 = 0.14\,\mu\mathrm{m}^2, A_2 = 0.44\,\mu\mathrm{m}^2$. The area of the loop three orders of magnitude larger than the area of the junctions $A_{loop} = 150\,\mu\mathrm{m}^2$. In this case the interference pattern modulates to zero only if $\Phi_{\mathrm{J}_1}/\Phi_0$, $\Phi_{\mathrm{J}_2}/\Phi_0$ are integer numbers at the same time. This does not happen if A_1/A_2 is not an integer. When one of $\Phi_{\mathrm{J}_1}/\Phi_0$ or $\Phi_{\mathrm{J}_2}/\Phi_0$ is an integer, the SQUID modulation goes to zero, as the supercurrent in one arm of the SQUID interferometer has been suppressed by the single junction interference.

From this model it is possible to conclude that inspecting the single junction interference regime of the SQUID interference pattern is useful to extract information on the single junctions parameters, like the effective area. This can be done even in extreme limiting situations where the SQUID interference pattern is very dense, providing valuable insights into the single junction physics of a SQUID.

2.4.5 *SQUIDs in magnetometry*

Since the discovery and demonstration of SQUID-type interference, the interest in SQUIDs has rapidly expanded into several fundamental research areas of quantum mechanics and condensed matter physics. Josephson junctions, *per se*, offer a vast playground for inventing new devices across various fields. Introducing a new tuning parameter to a Josephson junction opens up numerous combinations, expanding the range of possibilities. For example, SQUIDs acting as memories were proposed [58], arrays of dc-SQUIDs have been utilized to develop low-noise current sensors [59], and a differential amplifier based on a SQUID was proposed very recently [60]. SQUIDs currently provide invaluable contributions to the study of the Josephson effect, with novel measurement methods. The high sensitivity and precision of SQUIDs allow for the investigation of the interplay between superconductivity and magnetism, also making accessible the physics of magnetic moments and spins accessible to new levels.

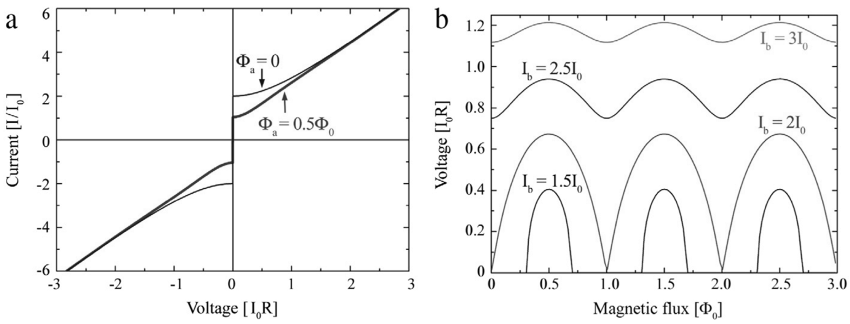

Figure 2.16: **(a)** Current–voltage characteristics computed for $\Phi_{\text{ext}} = 0$ and $\Phi_{\text{ext}} = \Phi_0/2$. **(b)** Voltage–magnetic flux characteristics computed for $i = 1.5, 2.0, 2.5$ and 3.0.

Starting from the basics, the most important application of SQUIDs consist in the measurement of small magnetic fields. In Fig.2.16, the IV characteristic of a SQUID with nonzero β_L are shown. By providing a constant current bias, a non-hysteretic ($\beta_C = 0$) SQUID works as a magnetic flux to voltage transducer and can be used as a magnetic flux detector.[10]

To explain the principle of working, suppose that a very small field is applied to the SQUID, such that $\Phi_{\text{ext}} \ll \Phi_0$, and the field is allowed to change in time. In this scenario, a current bias is applied to the SQUID in such a way that $V \neq 0$. When the magnetic field changes in time by a certain amount ΔB, the voltage drop across the SQUID changes by a small amount ΔV. The flux variation $\Delta\Phi$ can be linked to the variation in the SQUID voltage by a characteristic quantity of the SQUID, the voltage responsivity $V_\Phi = \partial V / \partial \Phi_{\text{ext}}$:

$$\Delta\Phi = \frac{\Delta V}{V_\Phi} \tag{2.50}$$

[10]Hysteretic SQUIDs can be used to measure magnetic fields, but in that case they are employed as critical current to flux transducers, as the well-define quantity is not the voltage, but the switching current. [61]

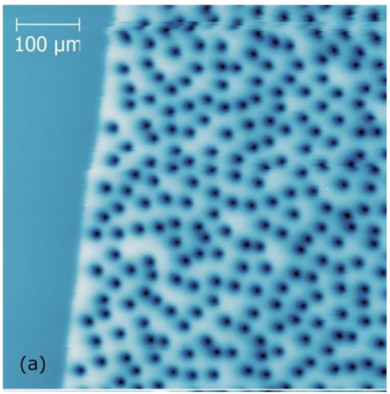

Figure 2.17: Scanning SQUID microscopy image of vortices in a 200 nm thick YBCO film taken at 6.93 μT and 4 K. Adapted from [63].

The voltage responsivity is the slope of the V–Φ curve at the magnetic bias point and represent how much the SQUID is sensitive to changes in the magnetic field. The magnetic field is obtained with the ratio of the measured magnetic flux to the SQUID effective area. Since the applied external flux to the SQUID is $\Phi_{\text{ext}} \ll \Phi_0$, to maximize the responsivity and enhance the signal-to-noise ratio an additional external magnetic flux is applied $\Phi_{\text{ext,add}} = \Phi_0/4$ [62]. The constant current bias, close to the critical current to have $V \neq 0$, is chosen to maximize the responsivity at the magnetic bias point.

The sensitivity reached by SQUIDs is extraordinary, and recently allowed by scanning SQUID microscopy (SSM) to image superconducting vortices in thin films of YBCO [63] shown in Fig. 2.17.

When the signals to be detected exceed the flux quantum, the SQUID response needs to be linearized. To achieve this, a Flux-Locked-Loop (FLL) configuration is commonly employed [64] with a scheme displayed in Fig. 2.18. The name originates from the fact that the effective flux needs to be less than one flux quantum: in this setup, the output voltage is transformed into a current using a resistor (R_F in figure) and fed back into the SQUID as a magnetic flux through an inductively coupled coil L_F, ensuring that the total magnetic flux is zero.

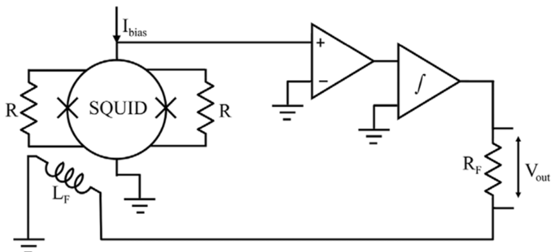

Figure 2.18: Flux locked loop circuit employed to increase the linear dynamic range of a dc SQUID. Adapted from [46].

In this discussions, the role of noise has not been considered. While it goes far beyond the scope of the thesis to give a full treatment of noise in SQUIDs, for the typical application the following conditions are required:

- in the operating regime of the device the Josephson energy associated with the supercurrent flow must be much larger than the effect of temperature k_bT:

$$E_J(T) = \Phi_0 I_0(T)/2\pi \gg k_bT \tag{2.51}$$

  This is equivalent in saying that, in the RCSJ picture, the critical current of the device I_0 must be much greater than the current thermal noise. At $T = 0.4\,\mathrm{K}$, the current thermal noise is $\delta I_{th} \simeq 18\,\mathrm{nA}$.

- The magnetic energy associated with the inductance must be also much greater than the thermal energy: $\Phi_0^2/4\pi L \gg k_bT$, which is equivalent to the condition:

$$L \ll L_F = \Phi_0^2/(4\pi^2 k_bT) \tag{2.52}$$

  L_F, the fluctuation threshold inductance, at $4\,\mathrm{K}$ takes the value of $\simeq 2\,\mathrm{nH}$ [65]

The origin of noise in quantum devices is known to depend on the transport regime. Shot noise is dominant when transport is limited by charge quantization while Johnson-Nyquist noise is given by the random thermal motion of carriers, plus many others.

In dc-SQUIDs, typically the noise is Johnson-Nyquist noise arising from finite temperature and by the resistive probe used to measure the voltage (that in Fig. 2.18 corresponds to the shunt resistors R). The effect of noise, anticipated in the RCSJ model, consist in a rounding of the IV curve below the critical current of the Josephson junctions. This rounding affects also the voltage responsivity V_Φ of the devices, degrading it. This directly affect the power spectral density (PSD) of the observable of the SQUID, the flux noise $S_\Phi = S_V/V_\Phi^2$. Using numerical simulations, assuming an average zero current thermal noise with a Gaussian spectra, allows to simulate both the voltage responsivity as a function of the current bias and the PSD of the voltage noise, as displayed in Fig. 2.19.

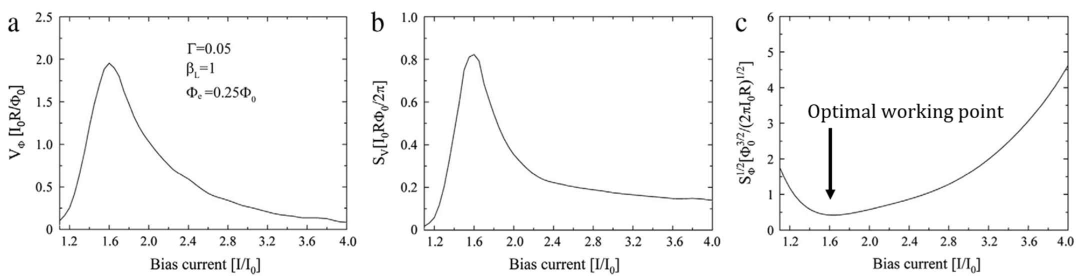

Figure 2.19: (a) Voltage responsivity as a function of the bias current. (b) Power spectral density value in the white region of the voltage noise as a function of the bias current. For bias current much greater than the SQUID critical current, the voltage noise tends to the Nyquist noise of the normal resistance ($R_s/2$). (c) Spectral density of the magnetic flux noise as a function of the bias current, the arrow indicates the minimum in S_Φ, obtained by taking the root square of the ratio S_V/V_Φ^2. Adapted from [46].

As shown in Fig. 2.19, there is a minima in the flux noise PSD S_Φ for a bias current of the SQUID of $\simeq 1.6 I_c$, as indicated by the arrow. Further numerical simulations allows to determine that the best condition for the SQUID operation as a magnetometer is obtained for $\beta_L = 1$ and for $\Phi = 0.25\Phi_0$. Specifically, to compare the performances of SQUID, another parameter is used, the noise energy per unit bandwidth:

$$\epsilon = \frac{S_\Phi}{2L} \tag{2.53}$$

and expressed in units of $\hbar$. The best SQUIDs reach ϵ of few $\hbar$, limited only by the uncertainty principle, and thus operate in the quantum limit [66, 67].

2.4.6 *SQUIDs in Current Phase Relationship Measurements*

SQUIDs are renowned not only for their exceptional sensitivity as magnetic field detectors but also for their pivotal role in probing the CPR of weak links. The fundamental principle underlying this type of measurements using the SQUID geometry is the strong asymmetry between the critical currents of the two arms [68, 69, 70, 71, 12].

There are different levels of analysis that can be pursued, one more refined than the other. I will begin with the most basic level, which, while ignoring some complexities, provides a solid foundation to build upon.

Strong asymmetry in the critical currents As mentioned, the CPR measurement relies on the fact that one arm of the SQUID presents a much higher critical current than the other arm, i.e.:

$$\max_{\varphi} I_1(\varphi) \gg \max_{\varphi} I_2(\varphi)$$

The idea is that the critical current of one junction is so large with respect to the other, that the critical current of the whole SQUID is maximized only if the current through the high-I_c junction is maximized.

In this way, when measuring the critical current of the SQUID while changing the flux density, the phase on the high-I_c junction is "locked" on value that maximizes the supercurrent and the modulation are entirely due to the CPR of the small-I_c junction: Thus, subtracting the dc-component from the measured pattern, the CPR of the small-I_c junction can be reconstructed.

$$I_c(\Phi) = I_1(\varphi = \varphi_{max}) + I_2\left(\varphi_{max} + 2\pi\frac{\Phi}{\Phi_0}\right) \tag{2.54}$$

Strong asymmetry in the critical currents $\&$ strong asymmetry in the derivatives The requirement of large asymmetry alone is not sufficient, and the precise shape of *both* the CPR must be taken into account [13]. Suppose that two junctions with CPR $I_1(\varphi_1)$ and $I_2(\varphi_2)$ are connected in a superconducting loop to form a SQUID. To find the critical current of the SQUID, the sum of I_1 and I_2 must be maximized taking into account the flux quantization condition, eq. 2.39:

$$I_c(\Phi) = \max_{\varphi}\left[I_1(\varphi) + I_2\left(\varphi + 2\pi\frac{\Phi}{\Phi_0}\right)\right],$$

which leads to requiring that φ is a stationary point:

$$\frac{\partial I_1(\varphi)}{\partial\varphi} + \frac{\partial I_2(\varphi + 2\pi\Phi/\Phi_0)}{\partial\varphi} = 0 \tag{2.55}$$

It is possible to explicitly factor out the critical currents from the CPR, by writing the CPR as:

$$I_i(\varphi) = I_{ci} f_i(\varphi) \tag{2.56}$$

To take into account the asymmetry in critical currents, the stationary condition, eq. 2.55, is rewritten in the following way:

$$\frac{I_{c1}}{I_{c2}}\frac{\partial f_1(\varphi)}{\partial\varphi} = -\frac{\partial f_2(\varphi + 2\pi\Phi/\Phi_0)}{\partial\varphi} \tag{2.57}$$

When the solution of this equation, φ^*, matches the "critical phase" φ_c for every value of the flux enclosed in the loop, such that $I_1(\varphi_c) = \max_\varphi I_1(\varphi)$, then the interference pattern (minus $I_1(\varphi_c)$) is the CPR of the small-I_c junction:

$$I_c(\Phi) = I_1(\varphi = \varphi_c) + I_2\left(\varphi_c + 2\pi\frac{\Phi}{\Phi_0}\right) \tag{2.58}$$

Alternatively, it is desirable for the function $\varphi^*(\Phi)$ to be well localized near φ_c. In such cases, the scenario depicted in eq. 2.58 will hold, and the CPR can be accurately reconstructed from the SQUID interference pattern.

From the condition of eq. 2.57, it is evident that to accurately describe the CPR, where every point of the $I_2(\varphi)$ relation is sampled, the following conditions on the derivatives must be satisfied:

$$\frac{I_{c1}}{I_{c2}}\max\left(\frac{\partial f_1}{\partial\varphi}\right) > -\max\left(\frac{\partial f_2}{\partial\varphi}\right)$$
$$\frac{I_{c1}}{I_{c2}}\min\left(\frac{\partial f_1}{\partial\varphi}\right) < -\min\left(\frac{\partial f_2}{\partial\varphi}\right)$$

If there is a point in the $I_2(\varphi)$ relation with a derivative that is too high, then no solution to eq. 2.57 exists, and that point cannot be accessed from the interference data of the SQUID.

Increasing the asymmetry ratio, which multiplies the derivative on the left side of eq. 2.57, expands the range of derivatives of the small-I_c junction that can be explored. At the same time, if the derivative of the high-I_c junction near φ_c is too small, then the function $\varphi^*(\Phi)$ is no longer well localized near φ_c, because in general eq. 2.57 will have a solution at a phase different than φ_c. A good example is the case of a sinusoidal CPR for $I_1(\varphi)$, where the derivative at the maximum of the CPR is zero.

The optimal scenario arises when the CPR of the high-I_c junction exhibits a high derivative near the maxima φ_c. This condition allows for minimal phase adjustments, thereby satisfying eq. 2.57. In this case, Josephson junctions exhibiting linear CPRs with a sawtooth-like shape are the most suitable candidates for serving as the high-I_c junction in a SQUID. This configuration facilitates the measurement of CPRs of various weak links, including those with moderate to high derivatives.

Further complications Some example of Josephson junctions exhibiting linear CPRs with a sawtooth-like shape are superconducting nanobridges. These are nanometers-sized constriction in a superconducting material (e.g. Niobium, Aluminum) that often can contribute with a non negligible kinetic inductance. In general, whenever the inductance has a sizable effect, the Φ_{ext} vs. Φ relation must be calculated taking into account these contributions. In the literature analytical approaches are described only in the case one junction has a known sinusoidal CPR [72], and in general a numerical methods must be used.

An additional problem that can occur is that the extracted CPR contains a low frequency Fraunhofer modulation. To avoid distortions in the CPR due to this effect, the low frequency contribution can be numerically filtered from the CPR in the Fourier $1/\Phi$ space, providing a more accurate results whenever the ratio $A_{\text{loop}}/A_{\text{JJ}}$ is not much larger than 1.

2.4.7 *SQUIDs as superconducting diodes*

The superconducting diode effect is a recently predicted [73] and observed [74] phenomenon in which by breaking inversion and time-reversal symmetry , the critical current for positive and negative current bias is different:

$$|I_{c+}| \neq |I_{c-}| \tag{2.59}$$

In this way there is a range of current bias values in which in one direction the superconductor is dissipative, and in the other superconducting. The discovery of this effect opens new possibilities for innovative applications in superconducting circuits, quantum computing, and other advanced technologies since a fundamental component of electronics, the analog of the pn-junction, is now available in a superconducting version. One of the possible physical origins in a homogeneous superconductor consist in breaking inversion and time-reversal symmetry applying a magnetic field while exploiting the magneto-chiral anisotropy, a property for which the electrical conductivity (resistance) differs depending on the direction of the applied magnetic field, resulting in non-reciprocal electrical properties according to the magneto-chirality coefficient γ:

$$R = R_0(1 + \gamma(\mathbf{B} \times \mathbf{z}) \cdot \mathbf{I}) \tag{2.60}$$

Here R_0 is the resistance in case of zero flux density $\mathbf{B}$, $\mathbf{z}$ is the direction where inversion symmetry is broken and $\mathbf{I}$ is the electrical current. If a nonzero flux density arises in a plane perpendicular to the $\mathbf{z}$ direction, the resistance is different according to the sign of $\mathbf{I}$, and when combined with superconductivity, this allows to obtain $|I_{c+}| \neq |I_{c-}|$.

The field of non-reciprocal transport in superconductors is active and very recent field of research, and there are several ways to obtain the superconducting diode effect. Vortices in superconductors, screening currents or self-field effects could be key and give a consistent contribution in the observation of this phenomena [75, 76, 77, 78, 79].

When the superconducting diode effect is combined with induced superconductivity in Josephson junctions, to emphasize the role of the Josephson effect, it is called Josephson Diode Effect. The first observation was performed in an array of Al-InAs quantum well-Al Josephson junctions [80]. The authors demonstrated that combination of magneto-chiral anisotropy, arising from the strong Rashba spin-orbit interaction along the perpendicular direction, and an asymmetric CPR are sufficient conditions for the device to show Josephson Diode Effect. Their findings are represented in Fig. 2.20, where by applying a magnetic field in-plane with the junction they were able to demonstrate a μA difference in the critical currents along the two opposite directions of transport. In recent works, the difference was reported both between the switching and the retrapping currents [81]. Moreover, one key property of the diode effect in proximized structures is the ability to be gate-tunable, which is used as argument in motivating that the Rashba SOI is key in visualizing this effect [82]. In the platform used in this thesis, the InSb nanoflag, Josephson Diode Effect was recently demonstrated by Turini et al. [11]. They found that for small magnetic fields, the supercurrent asymmetry $|I_{c+}| - |I_{c-}|$ increases linearly with the external field, saturating when the Zeeman energy becomes relevant. The diode effect was observed at $T = 30\,\mathrm{mK}$ and was found to be strongly suppressed by temperature, disappearing at T = $200\,\mathrm{mK}$.

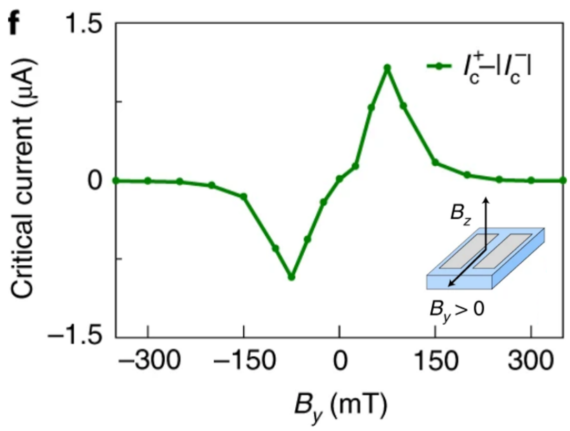

Figure 2.20: Difference between $|I_{c+}|$ and $|I_{c-}|$ as a function of the in-plane field B_y for an array of ballistic InAs quantum well Josephson junctions at a temperature of $100\,\mathrm{mK}$. Adapted from [80].

Paradoxically, that SQUIDs could demonstrate diode effect, it has been known for some time [83, 84] and formerly referred to as *voltage rectification*. However, after the Josephson diode effect demonstrations in Josephson junctions, the interest in the diode effect in asymmetric SQUIDs has been revived [85, 86]. The difference with respect to Josephson junctions is that in SQUIDs the effect can be demonstrated on smaller magnetic field scales, and also without invoking the physics of Rashba spin-orbit interaction,

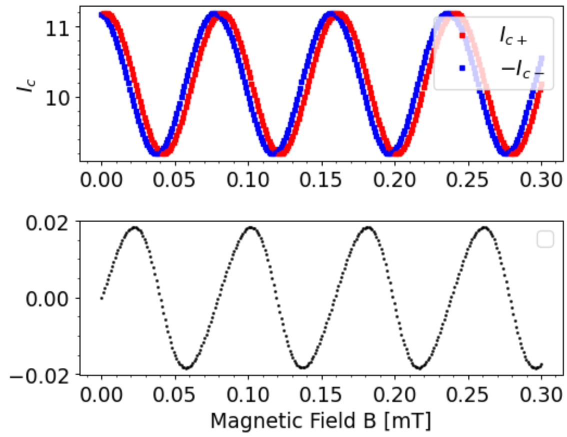

Figure 2.21: **Top** Positive branch I_{c+} (red) and reversed negative branch $-I_{c-}$ (blue) of a SQUID interference pattern. One junction has a sinusoidal CPR, while the other possess a sizable second harmonic content (10%). **Bottom**: rectification coefficient, calculated with eq. 2.61.

or more exotic phenomena. Both the time reversal simmetry and the spatial inversion symmetry are broken simply by requiring the flux quantization condition to hold and that one junction possess higher harmonics in the CPR. To show the simplicity with which the diode effect arises in SQUIDs, consider a SQUID made with two junctions:

$$I_1(\varphi_1) = 10\sin(\varphi_1) + \sin(2\varphi_1)$$
$$I_2(\varphi_2) = \sin(\varphi_2)$$

The calculated SQUID interference pattern is displayed in Fig. 2.21. In the top image, the positive critical current branch I_{c+} does not align with $-I_{c-}$, resulting in a periodic Josephson diode effect. The corresponding rectification η, defined below, is shown in the bottom panel:

$$\eta = \frac{|I_{c+}| - |I_{c-}|}{|I_{c+}| + |I_{c-}|} \tag{2.61}$$

The rectification is periodic with the interference pattern and shows the possibility to reverse the polarity of the diode by tuning the magnetic field. The rectification properties are enhanced as both the asymmetry and the higher harmonic content are increased. Experimental demonstrations of this effect were performed in SQUIDs formed by topological JJ with a 4π-periodic current-phase relationship and a topologically trivial JJ, in which by tuning properties of the trivial SQUID arm could lead to diode polarity switching [87]. Other investigations probed SQUIDs based on edge states transport in topological insulators and reporting efficiency as high as 73% [88]. However, being a really recent topic, not many experimental investigations have been carried out, which are indeed needed to optimize the conditions that enhance the JDE, including the effects of different materials and geometric configurations.

3

Experimental Details

3.1 InSb nanoflags

The III-V compound Indium Antimonide (InSb) is an interesting material, possessing large spin-orbit coupling, large Landé g-factor, and low effective mass, making it particularly important in spintronics and opto-electronics . In addition to that, it is a leading candidate for the implementation of topological qubits based on Majorana Fermions. The availability of this material, however, is not abundant. Due to an important lattice mismatch with other common semiconductor substrates, the Molecular Beam Epitaxy growth of InSb (in the form of quantum wells) has demonstrated to be a challenging task, as carefully designed buffer systems needs to be grown to overcome the lattice-mismatch, that with commons substrates, like GaAs, reaches even 14.6% [89, 90, 91]. To mitigate this problem, the growth of free-standing nanostructures was developed. Relaxing the strain caused by the lattice mismatch, the free-standing growth allows the development of large two-dimensional crystals.

One example of these nanostructures is provided by the InSb nanoflags, displayed in Fig. 3.1. These nanocrystals are grown on tapered indium phosphide nanowires using chemical beam epitaxy, resulting in high-quality, defect-free single crystals with electron mobilities up to $29\,500\,\mathrm{cm}^2\mathrm{V}^{-1}\mathrm{s}^{-1}$ [92]. With this method, lengths of $L = 2.8 \pm 0.2\,\mu\mathrm{m}$, width $W = 470 \pm 80\,\mathrm{nm}$, and thickness $t = 105 \pm 20\,\mathrm{nm}$ have been achieved. The Fermi wavelength of $\simeq 30\,\mathrm{nm}$ at typical electron densities of $10^{12}\,\mathrm{cm}^{-2}$ [11] places them in the quasi 2D limit, providing an interesting platform for quantum transport experiments.

3.2 Device Fabrication

The fabrication process of the SQUIDs begins with the as-grown sample of InSb nanoflags, which are attached to the Indium Phosphide stems. The initial step involves transferring the free-standing structures onto a highly conductive p-type Si(100) substrate, serving as a global back gate. A $285\,\mathrm{nm}$ thick SiO_2 layer covers the Si substrate, acting as a dielectric.

To detach the nanoflags from the stems, the sample is immersed in IPA and soni-

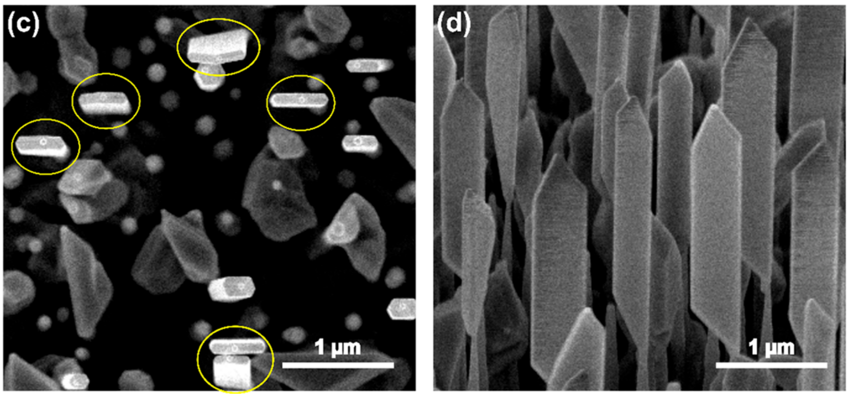

Figure 3.1: Top view and side view scanning electron micrographs of InSb nanoflags. Adapted from [92].

cated for 10 minutes. This procedure applies high-frequency vibrations to the sample, resulting in an IPA–Isopropyl Alcohol suspension of nanocrystals as the nanoflags detach from the stems and disperse in the IPA solution. This suspension is then drop-cast (20 µL) onto a clean pre-patterned substrate (cleaned in acetone and IPA for 5 minutes each via sonication) and allowed to dry for 2 minutes, followed by fresh IPA cleaning for 30 seconds prior to drying with N_2 flux. This drop-casting and drying process is repeated six times to ensure that a sufficient amount of nanoflags is transferred onto the substrate. The transferred InSb nanoflags are visualized by a Scanning Electron Microscope (SEM) to identify their coordinates on the substrate. High-resolution images (6144×4608 pixels^2) are captured, enabling further processing using a Computer-Aided Design (CAD) process in the Elphy software. The left image of Fig. 3.2 shows the result of the deposition process. The nanoflags are randomly scattered, with some impurities (mainly nanowire stems) remaining as residues from the transfer.

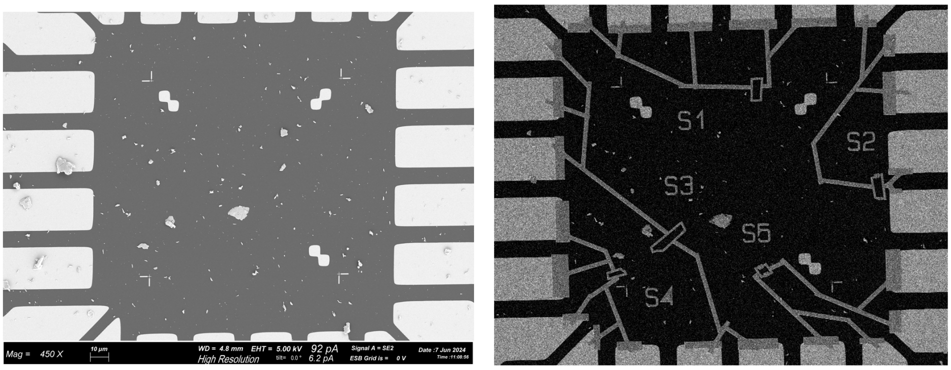

Figure 3.2: **Left**: Scanning electron micrograph of the chip after the deposition of InSb nanoflags. **Right**: Scanning electron micrograph after the fabrication of contacts lines to the nanoflags.

Based on the coordinates of the nanoflags observed in the SEM image, an exposure pattern for the SQUIDs is designed, where the geometry and shape of the superconducting stripes, as well as the area of the SQUIDs, are planned. This pattern is applied to the substrate using electron beam lithography (EBL), a fabrication procedure which directs a focused beam of electrons onto a polymeric resist material to apply the designed pattern. The exposed areas of the resist undergo a physical reaction that changes their structure, allowing them to be selectively removed so that a material, in this case Niobium, at the end of the process will be present only in specific regions.

For the SQUIDs used in this thesis, the AR 679.04 resist is spin-coated at 4000 rpm for 1 minute followed by baking the sample at $170\,^{\circ}\mathrm{C}$ for $90\,\mathrm{s}$. EBL is performed at $20\,\mathrm{kV}$ accelerating voltage of electrons, $10\,\mu\mathrm{m}$ aperture, $\approx 33\,\mathrm{pA}$ current, and $290\,\mu\mathrm{C\,cm^{-2}}$ dose using a $200 \times 200\,\mu\mathrm{m}^2$ write field. After EBL, the pattern is developed in AR $600 - 56$ for 1 minute, followed by rinsing in IPA for 30 seconds prior to drying with N_2 flux. The developed pattern is then exposed to O_2 plasma ($15\,\mathrm{W}$ for 75 seconds) for descum to remove any residual resist in the pattern. Prior to sputtering Niobium on the EBL-patterned sample, to achieve ohmic contacts [93], the exposed area of the InSb nanoflags is passivated by immersing the sample in $[NH_4)_2S_x$ (290mM$(NH_4)_2$S and 330mM S in deionized water] at $45\,^{\circ}\mathrm{C}$ for 60 seconds, followed by cleaning in deionized water for 30 seconds prior to drying with N_2 flux. The sample is then quickly transferred (80 seconds in air) to the sputtering chamber. [1]

Niobium sputtering is performed at $150\,\mathrm{W}$ for 240 seconds at a base pressure of 8×10^{-8} mbar and a working pressure of 5×10^{-3} mbar in the presence of Ar. The sputtered sample is then kept in acetone overnight for the lift-off process, followed by cleaning in IPA for 30 seconds. The final device, after the lift-off process, is displayed in the right image of Fig. 3.2.

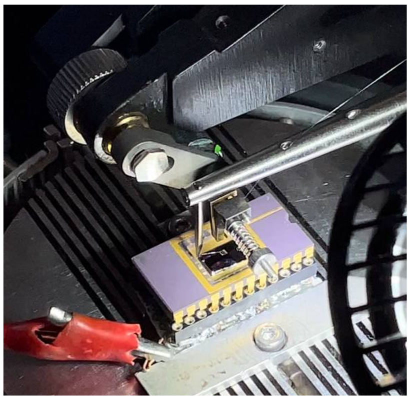

Figure 3.3: *Bonding* procedure. Aluminum wires are connected from gold pads to the chip carrier lines.

After completing the fabrication process, the sample chip is glued to a dual-in-line chip carrier using highly conductive silver paste, which enables the operation of the back gate. The individual SQUIDs are then connected to the chip carrier's lines by Aluminum wire bonding (as shown in Fig. 3.3) that represents the link between the μm-sized SQUIDs, to the macroscopic experimental apparatus that is used to probe their physical properties.

[1] Even if quickly is not a scientific term, there are some limitations in what is achievable in the fabrication facility. Studies have shown that the passivation effect does not last very long, and exposure to light and atmosphere rapidly degrades the passivating layer [94, 95]. Given that not everything is done *in situ*, between the fabrication steps there is the necessity to transfer the sample from one location to another. Thus, there is a minimal amount of time (compatible with security measures) required to move the sample to the magnetron sputtering machine.

3.3 Cryogenic Setup

The physics that is studied in this thesis involves cooling down electrons to low temperature. While at room temperature there is no need in specify *which* temperature, at low lattice temperatures, the interaction between electrons and phonons (quantized vibrations of the lattice) becomes weaker. This means that energy exchange between the electrons and the lattice is less efficient, allowing the electrons to maintain a different temperature from the lattice. In the experiments presented in this thesis, the electrons are not directly cooled. The cooling is achieved by lowering the temperature of the sample holder, which then by thermal coupling leads to cooling of electrons in the sample [96]. [2]

Initially, a detailed description of the cryostat is provided. This is followed by an explanation of the techniques employed to cool down the electrons in the sample.

3.3.1 *Closed Cycle Dry Cryostat*

The cryostat used in this thesis is the "DRY ICE 300 mK Continuous He-3 Cryostat" which is a closed cycle system designed to operate continuously at 300 mK. A closed cycle cryostat is a system where there is no need for continuous replenishment of cryogenic fluids like liquid helium, which in recent years as become more expensive. It features a single shot base temperature of 300 mK and a continuous base temperature of 350 mK. Photographs displaying the inside of the cryostat are provided in Fig. 3.4. To cool electrons to sub-kelvin temperatures, a He4-based pulse-tube cooler and a combination of cryogenic fluids, He4 and He3, are employed. They act in synergy to enable the sample to reach the target temperature. This is achieved through different temperature stages, which isolate the sample from the room-temperature environment and provide progressive cooling.

Pulse-tube cooler To achieve a temperature of few K, the basic apparatus consists in using a Pulse-Tube cryocooler, that includes a compressor, a cold head, and a heat exchanger. The principle of working consist in the compressor that pressurizes the cryogen (in this thesis He4, but also versions with He3 are present [98]), which is then expanded in the cold head to produce cooling. The heat exchanger facilitates the transfer of heat from the sample to the cryogen, allowing the system to reach and maintain the desired low temperatures. The heat is then dissipated by further water cooling the compressor. Such systems can operate continuously and for extended periods, reducing the need for frequent maintenance. [99]

Cryostat schematic The different temperature stages are represented by different plates, displayed in Panel (a) of Fig. 3.4 from high temperature to low temperature. The room temperature plate is not shown and resides on top of the cryostat. It is important as electrical grounding of the sample holder originates from there. The following stages are present:

[2] Today this is not the only way possible, it is also possible to cool-down electrons directly [97] by combining on-chip coolers with substrate cooling.

- First Stage (50-80K) : The first stage is cooled by the initial expansion of the refrigerant gas, using the pulse tube cooler described above. The cycle of expansion and compression of the pulse-tube cooler is repeated continuously, creating a steady-state cooling effect. This stage is responsible for removing the bulk of the heat from the sample and from the lower plates. The temperature is usually around 50-80K.
- Second Stage (4-10K): The second stage is also cooled by the compressor. This stage brings the temperature down to around 4K. The importance of this stage is that, below 4.2K, the He4 liquefies, condensing in the 1K pot (panel (b)).
- Base Temperature Stage (below 1K): The sample resides on the bottom of this plate and is thermally coupled to the He3 pot (panel (b)), which below a certain temperature[3], holds liquid He3.

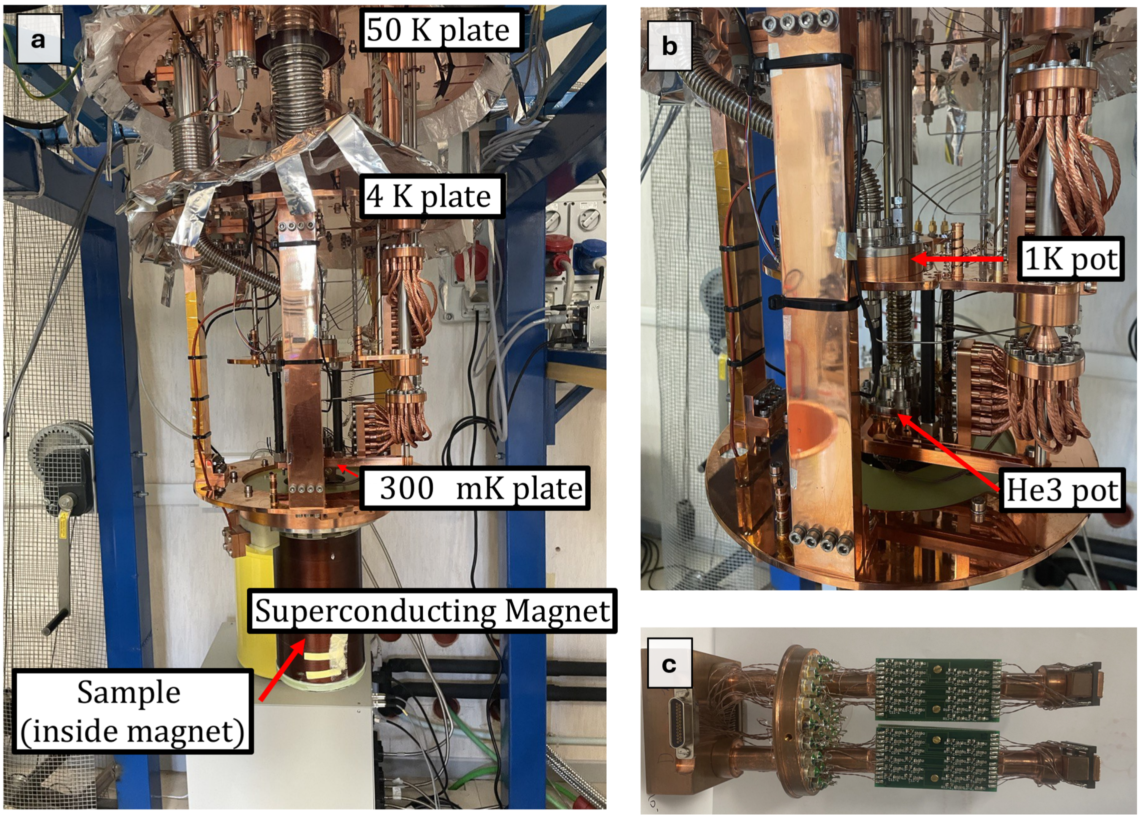

Figure 3.4: **(a)** Photograph highlighting the different plates of the cryostat. **(b)** Photograph highlighting the 1K (He4) pot and the He3 pot. **(c)** Cold findger with the low-pass filtering system.

To suppress thermal leaks from black body radiation, the cryostat is equipped with two stages of radiation screens. These screens are crucial in minimizing the heat load from thermal radiation. At low temperatures, even small amounts of heat can significantly impact the performance and stability of the cryostat. The radiation screens act as barriers, reflecting and absorbing thermal radiation from warmer components, protecting the

[3]according to the He3 pot pressure

colder stages of the cryostat. This helps maintain the desired low temperatures and improves the efficiency of the cooling system. Moreover, even with the right temperature conditions of the sample holder bath, thermal radiation actively suppresses the Josephson effect investigated in this thesis, and hence a good radiation screening is required in any low noise setup for superconductivity.

The sample, as shown in Fig. 3.3, is mounted on the cold finger depicted in panel (c) and attached to the lowest plate. It is not visible in panel (a) due to the necessity of placing the sample inside the superconducting magnet.

Cooling to 300 mK As mentioned before, by employing the pulse tube only temperatures of few K are reached due to its limited cooling power. The use of two additional circuits of cryogenic fluids, He3 and He4, allows for further cooling by exploiting the fundamental difference between them. At the thermodynamical level, the main difference between He3 and He4 is their vapor pressure as function of the temperature and represented by the phase diagrams in Fig. 3.5.

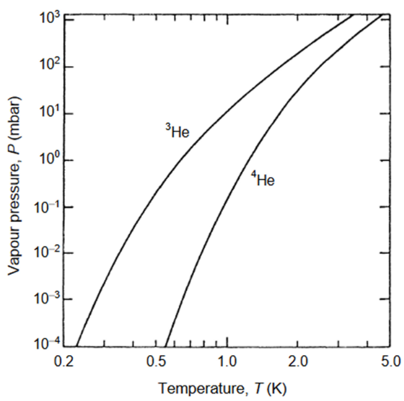

Figure 3.5: Vapor pressure *vs* temperature phase diagram for He3 and He4. At equilibrium, above the solid line the liquid phase is present, while below the gas form is the stable phase. Adapted from [100].

He3 is lighter, resulting in a weaker binding energy between atoms and a lower latent heat of evaporation L, $p \propto \exp(-L/RT)$, allowing for the evaporation process to occur more easily. This leads to a higher vapor pressure for He3 compared to He4, enabling lower liquid temperatures at the same vapor pressure. [4] At the base temperature achievable by the pulse tube, liquid He4 at atmospheric pressure ($\approx 1000\,\mathrm{mbar}$ in the figure) can be formed and deposited in the 1K pot. By pumping on the 1K pot and reducing its pressure, a temperature of approximately 1.5 K can be achieved, allowing the condensation of He3 gas into its liquid form. By reducing the pressure above the liquid He3, the system reaches the base temperature of 300 mK. This process is known as single-shot mode. In this mode, the cooling power is derived from the latent heat of evaporation of the He3, which is continuously pumped away, maintaining the low temperature. This method is particularly useful for experiments requiring low temperatures for a limited duration, as it provides a stable and efficient cooling environment. However, for long measurements, this method cannot be followed, as the liquid He3 is consumed and will eventually be depleted. In such cases, the continuous mode is employed. In continuous mode, the evaporated He3 gas from the liquid is collected and re-cooled by the 1K pot (liquid He4) to be condensed back into the liquid form. To facilitate this process, liquid nitrogen cold traps are also employed. These cold traps use the cryopumping effect to freeze any impurities in the gas, which may arise from contaminants in the pipelines. This ensures

[4] Additionally, He3 consists of three nucleons, making it a Fermion, while He4, with four nucleons, is a Boson—a difference that can be used in more advanced cooling method: the dilution refrigeration.

that the He3 gas is purified before being re-condensed, maintaining the efficiency and effectiveness of the cooling system. By continuously recycling the He3 gas, the system can sustain low temperatures for extended periods, making it suitable for long-term experiments and measurements. Following the procedure described above allows the obtain a bath temperature of $350\,\mathrm{mK}$.

Low-pass filtering As mentioned before, at low temperatures there may be a discrepancy between the electronic temperature and the bath temperature. Experimentally, because the thermometers are thermally anchored to the sample holder, the accessible quantity is the temperature of that part of the experimental setup, which is distinct from the system of interest: the electrons in the sample. To ensure that the electronic temperature reaches the bath temperature, all forms of excitations that can heat the electrons must be eliminated. Previously, the role of radiation screens in suppressing black body radiation was mentioned, but that is not the only source of excitation. The sample is connected to room temperature instrumentation, which injects high frequency noise that indirectly heats the electrons. To suppress that type of noise, the cold finger is filtered using two stages of RC and π filters, as represented by the two green boards in panel (c). It has to be underlined that the filtering is applied to each line, not just the measurement lines, as the key point of the filtering is not just to achieve more sensitive measurements.

It is important to note that improper filtering may result in suppressing superconductivity, even in samples that do possess this property [101]. The π filters are used to eliminate RF noise, and the RC filters eliminate the noise at lower frequency, with a cut-off frequency of 8 KHz. This ultimately allows to observe superconductivity.

3.4 Measurement Setup

3.4.1 *Instruments*

To perform transport measurements, the experimental setup must be capable of injecting and detecting currents, as well as applying and detecting voltages, both as AC excitations with a specific frequency and as DC with a constant bias. The key component, as well as their roles, are the following:

- Voltage source: provides a constant or variable voltage to a circuit. It maintains a fixed potential difference between two terminals, regardless of the current drawn by the load. We used are the *Yokogawa GS200* , and the *Keithley 2614B* voltage source.

- Current source: supplies a constant or variable current to a circuit. It maintains a fixed current through its terminals, regardless of the voltage across the load. In the experiments we used a *Keithley 2600B* (it can serve both as current and voltage source), to feed a current through the superconducting magnet.

- Lock-in amplifier: A lock-in amplifier detects and measures small AC signals in the presence of noise. It uses phase-sensitive detection to extract the signal at a specific reference frequency, effectively filtering out noise at other frequencies. This is done by multiplying the input signal with a reference signal and then passing it through a low-pass filter. The *Stanford Research SR850* is used in the experiments.

- Current Preamplifier: A current preamplifier amplifies small current signals to a measurable voltage level. It converts the input current to a voltage using a transimpedance amplifier, which consists of an operational amplifier with a feedback resistor. This allows for accurate measurement of low current signals. In the experiments we used the *Stanford Research SR570.*

- Voltage Preamplifier: A voltage preamplifier amplifies small voltage signals to a higher level for further processing or measurement. Such an amplifier uses an operational amplifier with high input impedance and low output impedance to boost the signal without significantly loading the source. The *Stanford Research SR560* was employed.

- Multimeters: used to measure voltage, current, and resistance. They operate by selecting the appropriate measurement mode and range, and then using internal circuitry to measure the desired parameter. In the experiments presented in this thesis, they are used to measure the voltages, and operate by employing analog-to-digital converters. Two *Agilent 34000 series 6 $\frac{1}{2}$ Digit Multimeter* are employed.

- Temperature controller: The controller allows to control the temperature of the sample. It increases the temperature through *heaters*, resistors that inject heat by Joule dissipation. It uses thermometers to monitor the temperature and adjusts the heating elements accordingly to maintain a stable temperature. This is achieved using a feedback loop, where the controller continuously compares the measured temperature to the setpoint and makes necessary adjustments to keep the temperature within the desired range (PID control). The *Lakeshore Model 340 Temperature Controller* is used.

3.4.2 *Voltage bias and Current bias*

Investigating the properties of the devices involves typically the measurement of the resistance of the system as a function of external parameters.

How to measure the resistance can greatly vary according to the transport regime and to the absolute value of the resistance, and different methods are available. When taking the voltage - current characteristics, mainly two methods are used: *current-bias* and *voltage-bias.*

Current bias involves applying a fixed current to the device and measuring the resulting voltage drop. This method is particularly useful for studying the voltage response of a system under a controlled current flow, and allows to study the differential resistance ($\delta V/\delta I|_{I_{bias}}$). Instead, Voltage bias consist in applying a fixed voltage to the device and measuring the resulting current.

One method is not strictly better than the other. For example, if the measurement of a large resistor is needed, the voltage-bias method would be more appropriate, as current sources would typically fail in applying reasonable value of currents for very large loads. At the same time, when studying the physics of Josephson junctions and SQUIDs, using one method over the other changes the behavior of the device. Using the second Josephson relation ($\dot{\varphi} = 2e\bar{V}/h$), a fixed voltage drop across the junction results in high frequency supercurrents, that average to zero when measured with a DC setup.

In the typical measurement performed in this thesis, a current bias is realized through a bias resistor, R_{bias}, typically $1 - 10\,\mathrm{M\Omega}$. The bias resistor is connected in series with the sample and the wiring of the cryostat. For a constant applied voltage $\bar{V}$, if the impedance of the sample is much smaller than the impedance of the bias resistor, such that: $R_{\text{sample}} \ll R_{\text{bias}}$ the following approximation holds:

$$I_{\text{bias}} = \frac{\bar{V}}{R_{\text{sample}} + R_{\text{bias}}} \simeq \frac{\bar{V}}{R_{\text{bias}}},$$

resulting in a bias current that does not depend on the specifying load of the device, providing a simple and efficient way to set a fixed current working point.

4

Results

This chapter is devoted to the original results obtained in this thesis. Two different geometries of SQUIDs based on InSb-nanoflags will be presented and characterized. A symmetric configuration, where the two nanoflags have the same geometrical area, and an asymmetric configuration, with different nanoflag widths. To begin with, characterization as a function of back gate voltage is discussed, and after that, the magnetic field response is presented.

4.1 Devices

dc-SQUIDs with different geometries were fabricated, following the process described in Sec. 3.2. The superconducting material of the SNS junctions is Niobium (Nb), and the semiconducting material are nanoflags of InSb. The scanning electron micrographs of two representative devices are shown in Fig. 4.1 and Fig. 4.2. The geometrical parameters (length, area) are measured with the Image Processing Toolbox offered by MATLAB, using the scale bar included in the images, and are reported in Table 4.1. In this chapter, the results for the devices C2S4 and H6S4 are reported. I will refer to them as the symmetric SQUID and the asymmetric SQUID, respectively, where the terms symmetric and asymmetric refer to the geometrical features of the devices. Notice that control of the carrier density in the semiconductor is obtained by a global back gate made from p-doped Silicon, placed $285\,\mathrm{nm}$ below the SiO_2 substrate. I underline that the control of each semiconducting channel in the two Josephson junctions forming a SQUID is not independent, and is performed globally by the back gate.

	L1	L2	W1	W2	A_{JJ1}	A_{JJ2}	A_{loop}
SYMM.(C2S4)	200	200	380	380	0.11	0.11	13.6
H6S1	120	200	1500	250	0.30	0.07	75
ASYMM.(H6S4)	180	190	1700	530	0.44	0.14	118

Table 4.1: Geometrical parameters of the devices presented. Subscripts i refer to the Josephson junction i, visually displayed in Fig. 4.1 and Fig. 4.2. Lengths in nm, areas in $\mu\mathrm{m}^2$. For the area of the junctions, A_{JJi}, twice the London penetration depth of Niobium has been included ($\lambda_{\mathrm{L}} = 43\,\mathrm{nm}$ [102]).

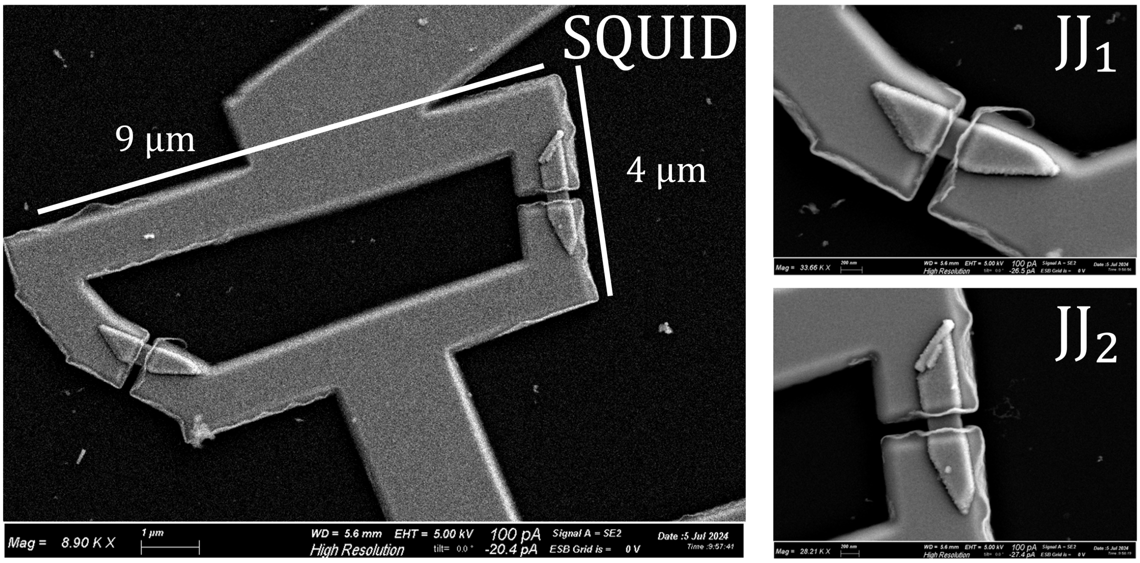

Figure 4.1: SQUID designed in a symmetric geometry. A zoom of the single junctions is displayed in the right panels. [C2S4]

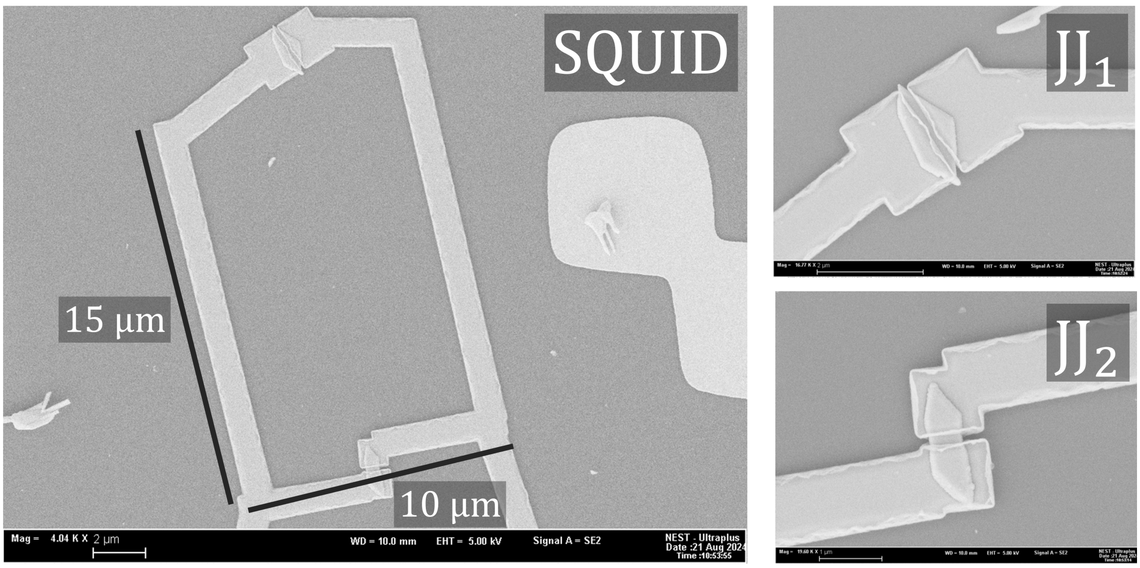

Figure 4.2: SQUID designed in asymmetric geometry. A zoom of the single junctions is displayed in the right panels. [H6S4]

SQUID in symmetric geometry In the left panel of Figure 4.1, a SQUID with a symmetric geometry is shown. Zoom on the single Josephson junctions is displayed in the right panels. The geometrical parameters of both junctions, measured from the SEM images, are equal within the experimental error. The loop inductance is calculated to be $L_{geo} = 9.4\,\mathrm{pH}$, using the tool provided at [103], which considers the loop as rectangular with sides of $9\,\mu\mathrm{m}$ and $4\,\mu\mathrm{m}$ and with circular cross section of radius[1] $r = 0.36\,\mu\mathrm{m}$. The kinetic inductance is instead estimated to be around $L_{kin} = 0.3\,\mathrm{pH}$ using eq. 2.44, leading to a total inductance $L = 9.7\,\mathrm{pH}$.

To understand the contribution of the loop self inductance to the behavior of the device, an estimate of the screening parameter, $\beta_L = 2\pi\frac{LI_c}{\Phi_0}$, is required. If this parameter is not negligible, then the flux inside the loop can differ by a substantial amount from the applied flux, and precise calculations of the inductance are needed. Considering $I_c = 100\,\mathrm{nA}$, which is the order of magnitude of the measured critical currents in the following, the screening parameter is calculated to be of order $\beta_L \approx 10^{-3}$. As such, the correction to the flux due to the self-inductance is considered negligible leading to $\Phi_{\mathrm{ext}} \approx \Phi$, where Φ_{ext} is the applied "macroscopic" flux and Φ is the effective flux penetrating the loop.

SQUID in asymmetric geometry In the left panel of Figure 4.2, the SQUID with an asymmetric geometry is presented. Zoom on the single junctions is also displayed in the right panels. In this device, one junction is three times wider than the other, while maintaining the same distance between the electrodes. Following a similar analysis as for the symmetric geometry, the total inductance is estimated to be $L \approx 20\,\mathrm{pH}$, still giving $\beta_L \approx 10^{-3}$. Thus, the assumption $\Phi_{\mathrm{ext}} \approx \Phi$ is valid also for this device.

4.1.1 *Superconducting Parameters*

A description of induced superconductivity in the semiconductor cannot begin without briefly discussing the properties of the superconducting banks. The sputtered Nb electrodes can be characterized first by two quantities: the critical transition temperature at zero magnetic field (T_c) and the upper critical magnetic field at low temperature, $H_{c2}\,(T)$.

In Fig. 4.3 and Fig. 4.4, measurements of the superconducting properties of the Nb strips are presented. The measurements are performed on different devices on the same chip of the symmetric SQUID, and are done by current biasing the Nb strips with $1\,\mu\mathrm{A}$, measuring the voltage drop while changing the temperature (Fig. 4.3) or the applied perpendicular magnetic field (Fig. 4.4). The critical temperature measurement shown in Fig. 4.3 displays a sharp transition at $8.1\,\mathrm{K}$, while the upper critical field transition displayed in Fig. 4.4 is $2.9\,\mathrm{T}$, both consistent with values reported in literature [104]. A residual resistance below the transition is observed in Fig. 4.3, a feature observed also in other Nb strips and attributed to superconducting domains presents in the strips with

[1]In the case discussed, the cross section is not circular, but an effective radius can be calculated by taking the perimeter of the cross section $C = 2.3\,\mu\mathrm{m}$ (strip width $1\,\mu\mathrm{m}$ and thickness $0.15\,\mu\mathrm{m}$) and dividing it by 2π.

other critical temperature and resistance.

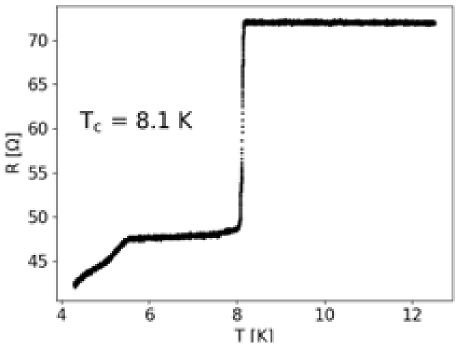

Figure 4.3: Critical temperature of Nb strips, measured on a device (D2S5) on the same chip as the symmetric SQUID and at zero applied magnetic field. Since it was not possible to measure the voltage drop just across Niobium, the resistance of the device is included. $T_c = 8.1\,\mathrm{K}$.

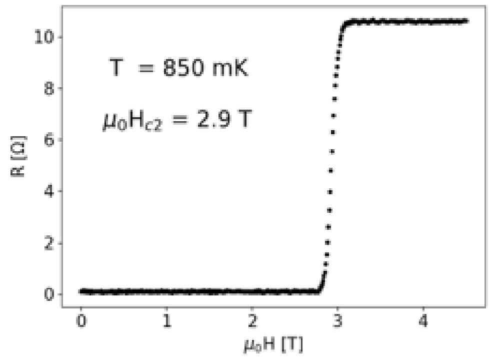

Figure 4.4: Upper critical field measured at T = $850\,\mathrm{mK}$, on a device (C2S3) on the same chip as the symmetric SQUID. The magnetic field is applied along the perpendicular direction to the device plane. $\mu_0 H_{c2} = 2.9\,\mathrm{T}$.

With a superconducting critical temperature of $8.1\,\mathrm{K}$, I can use eq. 2.12 to get the superconducting gap in the leads, obtaining $\Delta(0\,\mathrm{K}) = 1.2$ meV. At the same time, by using the Fermi velocity of InSb, an estimate of the coherence length in the ballistic limit is provided with the BCS relation:

$$\xi_\mathrm{N} = \frac{\hbar v_{F,N}}{\pi\Delta^*} \geq \frac{\hbar v_{F,N}}{\pi\Delta}$$

Using $v_F = 1.5 \cdot 10^6$ m s^{-1} in InSb [9], $\xi_\mathrm{N} \geq 420\,\mathrm{nm}$ is obtained. Comparing the coherence length with the electrode distance $L = 200\,\mathrm{nm}$ provided in Table 4.1, sets the devices in the short-junction regime.

4.2 Two Josephson Junctions in parallel

Two Josephson junctions embedded in a superconducting loop form a superconducting quantum interference device, in which the phase drop across the two junctions is not independent, but rather connected by the flux quantization condition discussed in Sec. 2.4.1. If the flux enclosed in the loop is zero, i.e., there is no external magnetic field applied and the self-inductance of each arm is negligible, the SQUID is well summarized by describing it as two Josephson junctions in parallel.

The first characterization of the devices is a description of the field effect in the normal state. After that, I'll present the field effect on supercurrent. The section is concluded commenting the features of the differential conductance as a function of the voltage bias.

4.2.1 *Conductance measurements*

As described in Sec. 2.4.3, from the transfer curves of semiconductors (conductance vs back gate voltage) information on field effect mobility, contact resistance, and channel threshold voltage is obtained. Using dc-SQUIDs with parallel Josephson junctions, the total conductance is just the sum of the two conductances of the single junctions:

$$G_{\text{SQUID}} = G_{\text{JJ,1}}(V_{th,1}, \mu_1, R_c) + G_{\text{JJ,2}}(V_{th,2}, \mu_2, R_c), \tag{4.1}$$

where $G_{\text{JJ,i}}$ is the conductance of junction i, $V_{th,i}$ is the channel opening threshold, μ_i is the field-effect mobility, and R_c is the effective contact resistance. The expression for the single junction conductance is given by eq. 2.45.

The contact resistances are assumed to be the same for all interfaces, keeping the number of parameters reasonable. A physical motivation for this assumption is the fact that, being an asymptotic parameter at high back gate voltages where $R_N \ll R_c$, two different contact resistances in parallel could not be distinguished without having very different channel thresholds or without being able to control the single junctions.

To measure the conductance in the normal state, an AC setup in current bias is used with an excitation of $1\,\text{V}$ amplitude on a bias resistor of $R_{\text{bias}} = 10\,\text{M}\Omega$ (that, when $R_{\text{bias}} \gg R_N$ corresponds to $100\,\text{nA}$ of current bias) at a frequency of $13.321\,\text{Hz}$, measuring both the voltage and the current with lock-in amplifiers. The conductance is obtained dividing the amplitude of the current signal by the amplitude of the voltage signal. While in the symmetric SQUID the conductance was measured up to $V_{bg} = 40\,\text{V}$, due to higher leakage currents, the measurements on the asymmetric SQUID are limited to $V_{bg} < 20\,\text{V}$. When the temperature is below the Nb critical temperature, the normal state is obtained by suppressing the induced superconductivity in the semiconductor with the current bias.

Symmetric SQUID The normal state conductance of the symmetric SQUID at a temperature of $2\,\text{K}$ is presented in Fig. 4.5. Going from lower to higher back gate voltages, zero conductance is observed where the chemical potential is in the band gap, followed by a quasi linear increase and ending with a saturation value. From this description, no notable differences are found with respect to the same trace of a single Josephson junction [105], confirming the symmetric behavior of the SQUID.

To get the mobility and other physical parameters, first the fit procedure was performed with the asymmetric model given by eq. 4.1. The threshold parameters $V_{th,1}$ and $V_{th,2}$ as well as the field effect mobilities μ_1 and μ_2 were very similar and not different enough to motivate one or two additional parameters. This result is also supported by the symmetric geometry under study. Therefore, a symmetric model consisting in the parallel of two identical Josephson junctions is employed. The result of the fit is shown in Fig. 4.5 with the residuals of the fit below. The optimal parameters are given in Table 4.2. An effective field effect mobility of $\mu = 8900(300)\,\text{cm}^2\text{V}^{-1}\text{s}^{-1}$ corresponds to a mean free path of $\approx 150\,\text{nm}$ at back gate voltages around $20\,\text{V}$. Comparing this length with the electrodes distance of $200\,\text{nm}$ places the device in a crossover regime between the ballistic and diffusive cases. The threshold $V_{\text{th}} = 1.9(1)\,\text{V}$ obtained from the fitting procedure is overestimated due to the fact that the two semiconducting channels truly open at slightly different voltages.

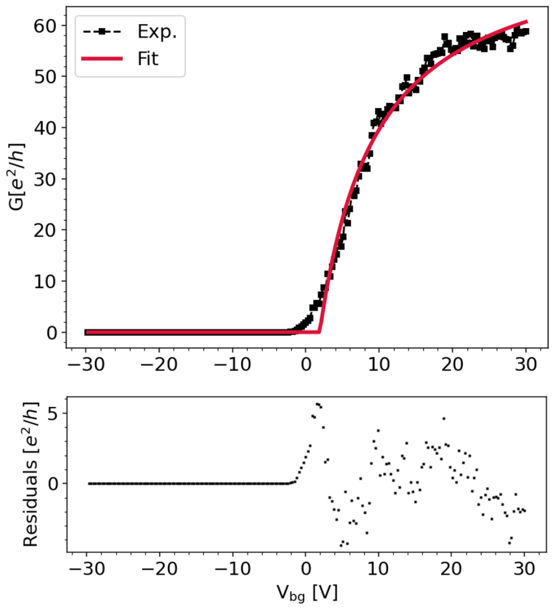

Figure 4.5: **Top**: Conductance trace measured at $T = 2\,\text{K}$ of the symmetric SQUID. The fit (red line) is superimposed on the experimental data (black squares). **Bottom**: Residuals of the fit.

Symmetric SQUID	JJ1 (= JJ2)
μ [$\text{cm}^2\text{V}^{-1}\text{s}^{-1}$]	8900 ± 300
V_{th} [V]	1.9 ± 0.1
R_c [Ω]	334 ± 5

Table 4.2: Optimal parameters of the fit procedure using the model of eq. 4.1 for the symmetric SQUID using twice the conductance of a single channel. The geometrical parameters used are indicated in Table 4.1.

Asymmetric SQUID The conductance trace of the asymmetric SQUID at $T = 2\,\text{K}$ is reported in Fig. 4.6 together with the fit. Using an asymmetric model, two different channel thresholds and two different mobilities are obtained as optimal fit parameters, reported in Table 4.3. It is not possible to assert which junction has the higher field-effect mobility between the two. It is possible to link the mobilities to the threshold voltages, since the slope of the conductance near the channel opening thresholds is related to that channel mobility.

Using the values of the mobilities and channel thresholds, at a back gate voltage of $15\,\text{V}$, one nanoflag has an elastic mean free path of $l_{\text{mfp}} = 300\,\text{nm}$ (the one with higher mobility), while the other one has $150\,\mathrm{nm}$, placing one junction in the ballistic regime and the other in a crossover regime. Notice that the latter value is consistent with the one obtained earlier in the case of the symmetric SQUID, where both single Josephson junctions are fabricated with the same geometry as the narrower junction in this asymmetric configuration.

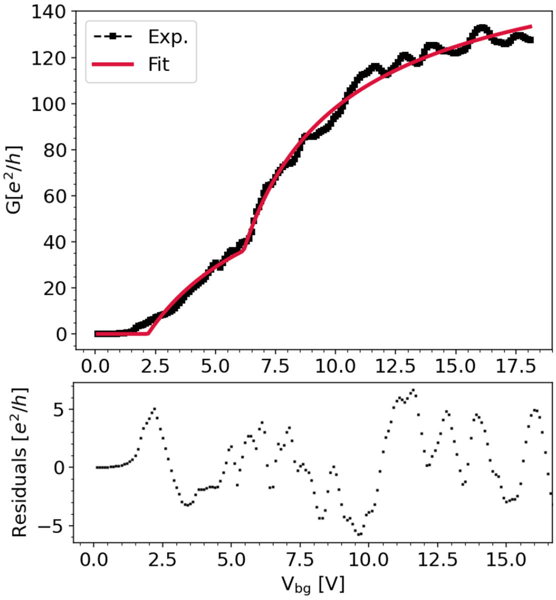

Figure 4.6: **Top**: Conductance trace measured at $T = 2\,\mathrm{K}$ of the asymmetric SQUID. The fit (red line) is superimposed on the experimental data (black squares). **Bottom**: Residuals of the fit.

Asymmetric SQUID	JJ1	JJ2
μ [$\mathrm{cm^2V^{-1}s^{-1}}$]	18600 ± 950	9700 ± 500
V_{th} [V]	2.2 ± 0.1	6.2 ± 0.1
R_c [Ω]	147 ± 2	147 ± 2

Table 4.3: Optimal parameters of the fit procedure using the model of eq. 4.1 for the asymmetric SQUID using two different channels. The geometrical parameters used are indicated in Table 4.1. The normal state conductance was measured at $T = 2\,\mathrm{K}$.

This would suggest that the junction with the higher threshold of $V_{th} = 6.2$ V is the narrow one. However, based on normal state characterization alone, it is not possible to confirm this definitively; additional characterization in the superconducting state is required for further insights.

4.2.2 *Voltage - current characteristics*

To characterize the dissipationless regime, a DC current bias setup is used. By changing the current bias and measuring the voltage drop across the devices, $V - I$ curves are obtained. Two examples of $V-I$ curves are shown in Fig. 4.7 and Fig. 4.8, for the two investigated devices, respectively.

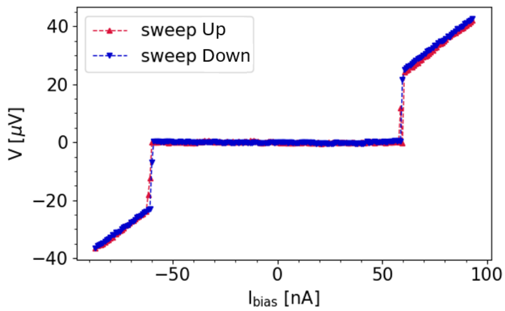

Figure 4.7: Voltage drop measured as a function of the current bias for the symmetric SQUID. $V_{bg} = 20\,\mathrm{V}$, $T = 350\,\mathrm{mK}$. The applied magnetic field is adjusted such that reductions in the critical currents due to quantum interference are not present.

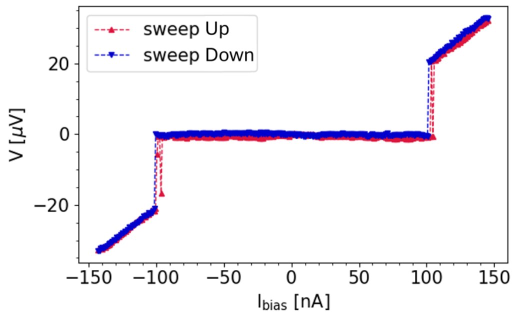

Figure 4.8: Voltage drop measured as a function of the current bias for the asymmetric SQUID. $V_{bg} = 18\,\mathrm{V}$, $T = 350\,\mathrm{mK}$. The applied magnetic field is adjusted such that reductions in the critical currents due to quantum interference are not present.

As a general trend, going from negative values of current to positive, first a linear relation between current and voltage drop is seen, followed by a sudden jump to zero of the voltage for a finite value of current bias, showing finite supercurrent. When measuring $V-I$ curves, a difference is often observed in the current value at transition depending on whether the transition is measured from the resistive state to the superconducting state or vice versa. The current at the transition from the superconducting to the dissipative state is called the *switching current*, while for the reverse situation, it is called the *retrapping current* [23]. This different, hysteretic behavior is a common feature of superconducting devices such as Josephson junctions and tends to disappear (resulting in equal switching and retrapping currents) as the temperature increases. The value of the switching currents depends on several variables, including the current bias ramp rate, the switching mechanism, the presence of noise, and others. A more detailed discussion is provided in Appendix A, where this topic is addressed in more detail. In this thesis, the switching current is the one used to estimate the critical current.

Differences between switching and retrapping currents have been attributed to the difference in the electronic temperature when going from the resistive state to the superconducting one; the power injected in the device $P_{in} = VI_{\mathrm{bias}}$ is non-zero in the resistive state and zero in the superconducting state [106], resulting in electron heating in the first case. It is also known [47] that a finite capacitance of the junction can cause a difference between switching and retrapping current (*underdamped* regime). Besides, the presence of a consistent thermal current noise component $2ek_bT/\hbar$ in the current bias might reduce this difference. In the performed experiments, no notable difference was typically seen between switching and retrapping current at $T = 350\,\mathrm{mK}$ and above. In one case, at the base temperature of $T = 310\,\mathrm{mK}$, I report a substantial difference between these two values, as displayed in the $V-I$ curve in Fig. 4.9.

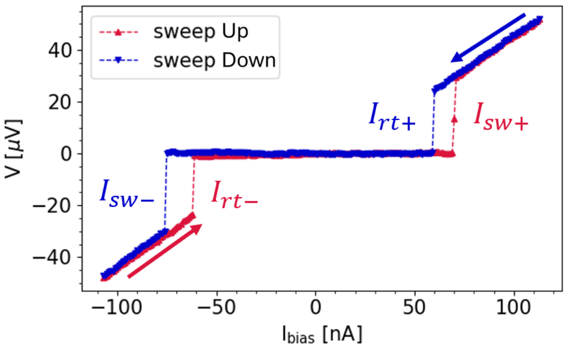

Figure 4.9: Voltage drop measured as a function of the current bias for the symmetric SQUID. $V_{bg} = 20\,\mathrm{V}$, $T = 310\,\mathrm{mK}$.

At a temperature $T = 350\,\mathrm{mK}$, the thermal current noise is $14.7\,\mathrm{nA}$, enough to suppress hysteresis. The role of the thermal noise in the $V - I$ curve can also be appreciated in Fig. 4.10. At a temperature of $350\,\mathrm{mK}$, premature switching events are seen. These features can be explained with the tilted washboard potential model discussed in Sec. 2.3.5. When the phase particle is thermally excited, it can move out of one local minima towards another one, where it stops. In this way, when using the second Josephson relation, $\dot{\varphi} = 2eV/\hbar$, the phase acquires a non-zero average derivative, giving rise to a non-zero average voltage drop that can be detected in a DC setup. The thermal excitation measured in the figure has a range consistent with the expected theoretical prediction, $\delta I_{th} \simeq 15\,\mathrm{nA}$.

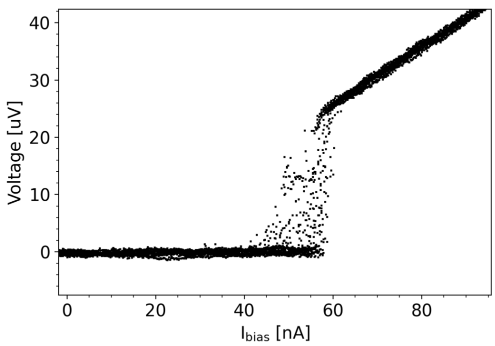

Figure 4.10: Positive branch of the $V - I$. Premature switching events to the normal state are due to thermal current noise $\delta I_{th} = 2ek_bT/\hbar$. Here seen at $T = 350\,\mathrm{mK}$.

If the supercurrent features originate from the Josephson effect, the combination with the field effect of semiconductors allows for the implementation of the Josephson Field Effect Transistor (JoFET). By acting on a back gate, the carrier concentration in the normal part (the semiconductor between the superconducting leads) can be varied, directly impacting on the amplitude of the supercurrent flow. To demonstrate that the fabricated SQUIDs also behave as JoFETs, $V - I$ curves as a function of the back gate are measured. The results are shown in the color maps in Fig. 4.11 for the symmetric SQUID and in Fig. 4.12 for the asymmetric SQUID.

The differential resistance, obtained *via* numerical differentiation of the $V-I$ curves, is plotted against back-gate voltage and current bias. Dark regions, representing the superconducting phase, are separated from the normal region by the coherence peak, visually displayed as a bright line highlighting the transition. The same features found in the normal state transfer curve are observed in these supercurrent transfer curves, reinforcing the connection between conductance (number of modes, transmission coefficients) and supercurrent amplitude. Supercurrent pinch-off is demonstrated in both devices, excluding Nb accidental shorts or other transport channels different from the InSb nanoflags, confirming their behavior as JoFETs. Interestingly, the pinch-off point for the supercurrent does not coincide with the channel opening threshold. This indicates that the supercurrent transport regime is changing from the SNS-type regime to an exponentially suppressed tunneling regime as the semiconductor chemical potential is brought in the band gap.

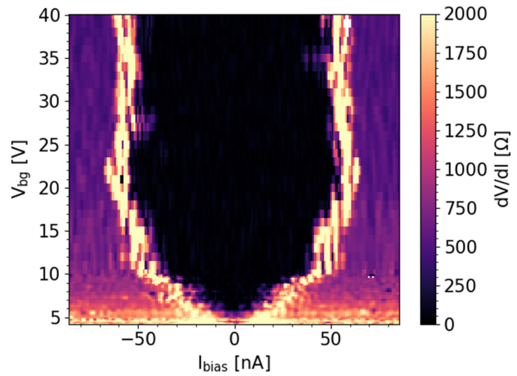

Figure 4.11: Back gate control of the critical current for the symmetric SQUID at $T = 350\,\mathrm{mK}$.

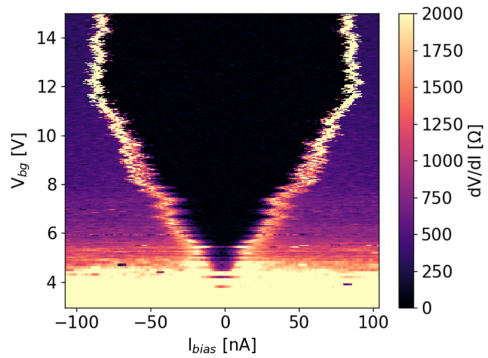

Figure 4.12: Back gate control of the critical current for the asymmetric SQUID at $T = 350\,\mathrm{mK}$

The connection between the conductance (inverse of resistance) of the devices and the critical current can be further explored using an important parameter for superconducting electronics: the $I_c R_N$ product. In Josephson junctions, this characteristic voltage gives information on the quality of the superconducting coupling to the banks, and its parametrization has been often used to gain insight to the physics of Josephson junctions [23, 107, 108]. For the case of SQUIDs at zero magnetic field, having two junctions in parallel we expect:

$$I_c = I_{c,1} + I_{c,2} \tag{4.2}$$

$$R_N = \frac{R_{N,1} R_{N,2}}{R_{N,1} + R_{N,2}} \tag{4.3}$$

Defining $x = \frac{R_{N,2}}{R_{N,1}+R_{N,2}}$, the fraction of the normal resistance of junction 2 over the sum of the two normal resistances, and expanding the product, is possible to show that:

$$I_c R_N = V_1 \cdot x + V_2 \cdot (1-x)\,,$$

i.e. the I_cR_N product of a SQUID is the weighted average of the $V_i = I_{ci}R_{Ni}$ products of the two junctions.

To measure the normal resistance R_N of the SQUIDs, superconductivity should be totally suppressed; one way of doing this is by applying a large voltage to the junction, such that $eV > 2\Delta$. In measuring the $V - I$ curves as a function of back gate voltage of Fig. 4.11 and Fig. 4.12, this condition is not satisfied, as at most tens of microvolts of voltage drop are developed. Hence, the displayed resistance in the figures is not the normal resistance, R_N, but provides a lower bound for its value and I will be referring to it as the switching resistance, R.

When using the switching resistance R to calculate the I_cR product, the lower bound on the normal resistance translates into a lower bound on the I_cR_N product. In the case of the symmetric SQUID, the normal state resistance satisfying $eV > 2\Delta$ was also measured for a few values of the back gate, and only small deviations are observed from the corresponding switching resistance, as shown in Fig. 4.13.

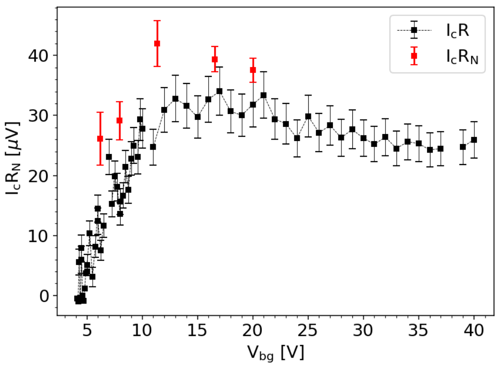

Figure 4.13: Product of the critical (switching) currents times the normal resistance R_N (red squares) and times the switching resistance R (black squares) for the symmetric SQUID.

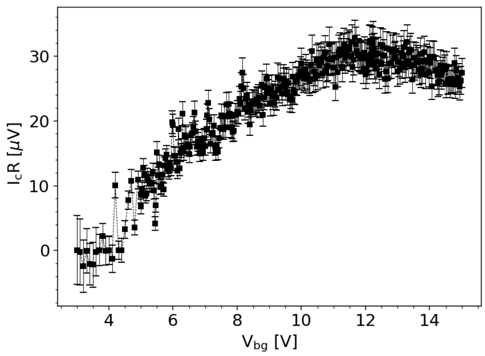

Figure 4.14: Product of the critical (switching) current times the switching resistance R for the asymmetric SQUID.

In the Figure, the I_cR_N product is displayed in red, while in black the value of the I_CR product. The latter was computed from the measurements of Fig. 4.11. The difference between the two values is limited to O($10\,\mu$V), motivating the use of R to have an estimate of the characteristic voltage I_cR_N. For the asymmetric SQUID, the switching current times the switching resistance is plotted in Fig. 4.14. The values obtained for the two devices do not differ and completely overlap, suggesting similar superconducting coupling. Both the I_cR product are modulated with the field to a saturation value, a trend consistent with what is reported in the literature[109, 108]. The value of I_cR_N of $\approx 30\,\mu$V is larger with respect to previous devices reported in the literature. In [9] an $I_cR_N = 16\,\mu$V was measured in similar junctions with a titanium inter layer between the semiconductor and the superconductor. This larger number is not due to having two junctions in parallel, as we expect half of the normal resistance and double the critical current. We attribute it to the fact that having eliminated the Ti interlayer from the fabrication process, the induced superconductivity has been strengthened. Indeed, most models of CPRs in different limits predicts I_c to be proportional to Δ^*/R_N [110, 45], with a proportionality factor that depends on the temperature, on the transparency of the interface, and on the number of modes [111, 112]. The induced gap Δ^* arises *via* the proximity effect, described in Sec. 2.3.2. A schematic of the induced gap region in the SNS junctions used in this thesis, is represented in Fig. 4.15.

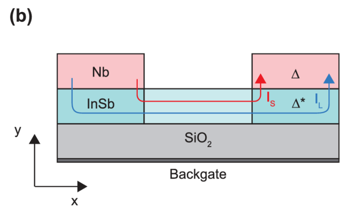

Figure 4.15: Adapted from [10]. The superconducting Nb has a gap of Δ, while the InSb nanoflag proximized has a renormalized gap Δ^*

To quantify the induced superconducting gap Δ^*, measurements of subharmonic gap structures are often performed. This kind of investigation consist in measuring dips or peaks in the differential conductance of the $I-V$ curve and possibly look for structures with harmonic periodicity. These structures, if corresponding to multiple Andreev reflections (MARs), allow to estimate the induced gap, as they depend on $2\Delta^*/n$, where n is the order of the Andreev reflection. The simple physical picture of MAR is complicated by the finite transparency of the junctions that leads also to normal reflection processes. For SQUIDs, having two junction in parallel, the same voltage drop is not guaranteed to give rise to the same coherent processes in the two junctions, and a rigorous theoretical treatment should take into account the differences between the two junctions.

An $I-V$ curve measured up to high voltage bias region ($V > 3\,\text{meV}$) is shown in panel (a) of Fig. 4.16. Panel (b) shows the differential conductance of the $I-V$ curve, measured with the lock-in amplifier technique. This measurement is performed at $20\,\text{V}$ of back gate voltage and a temperature of $440\,\text{mK}$.

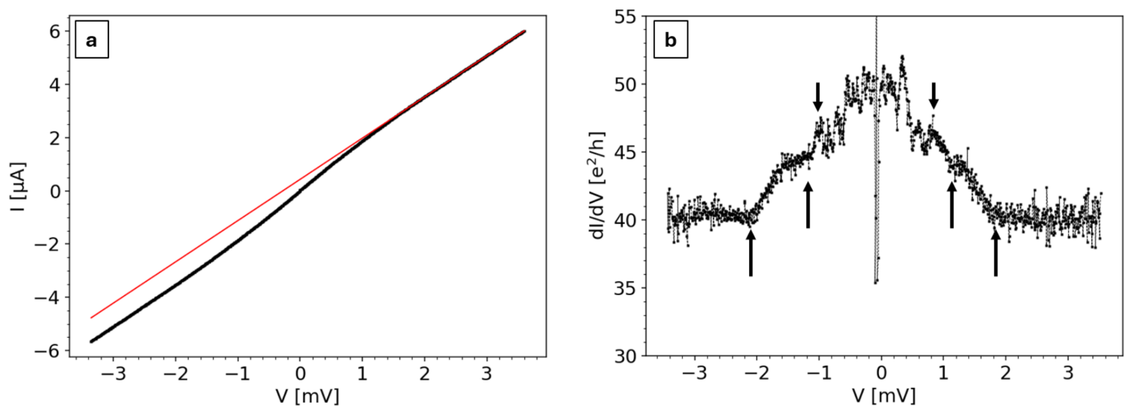

Figure 4.16: **(a)** current as a function of the voltage applied to the symmetric SQUID (black line) at $T = 440\,\text{mK}$. and $V_{bg} = 20\,\text{V}$ A linear fit in the region of high voltage bias is superimposed (red). $I_{exc} = 427\,\text{nA}$, $1/R_N = 40e^2/h$. **(b)** Differential conductance, measured with a lock-in amplifier. Subharmonic gap structures are visible and indicated by arrows.

From the linear fit of the $I-V$ curve of Fig. 4.16 (a) in the region where $eV > 2\Delta$, the normal resistance can be extracted. In addition to that, typically a non-zero intercept is estimated, called *excess current* if it is positive, *defect current* if it is negative. It originates from the fact that each electron that is Andreev-reflected contributes to a transfer of charge $|\Delta q| > e$, resulting in deviations from the normal state current [113]:

$$I_{exc} = I - V/R_N \tag{4.4}$$

The intercept estimated from the linear fit is $I_{exc} = 427\,\mathrm{nA}$, with a corresponding $I_{\mathrm{exc}}R_N$ product of $280\,\mathrm{\mu V}$. For a Josephson junction, this quantity is proportional to the induced gap by the superconductor. Not including the effect of a proximity layer with an induced gap Δ^*, the excess current is proportional to the superconducting gap with a coefficient that is $8/3$ in the ballistic regime [31] to $(\pi^2/4 - 1)$ in the diffusive transport regime [114]. It is important to underline that these results were obtained not including a proximity layer, as its presence decreases the excess current[34]. Therefore, are not directly applicable to the SNS junctions discussed in this thesis.

For SQUIDs, following a similar analysis done for the I_cR_N product, it is an average of the product of the single junctions. In fact, since excess currents in the two junctions arise from contribution to the current due to Andreev reflections–a process of charge transport where one electron is converted to a Cooper pair–they sum up linearly for parallel channels of transport. In the presence of a proximity layer, no simple relation between the excess current and the induced gap has been derived, and explicit calculations are needed. The transparency of the interface between Nb and InSb must be taken into account, along with the critical temperatures T_c of the electrodes and the proximized layer T_c^*. These parameters are not available and must be estimated from further measurements. Therefore, from the numbers estimated it is possible to provide a lower bound for the induced gap, which is different according to the transport regime. From $\Delta^* > 105\,\mathrm{\mu eV}$ in the ballistic regime to $\Delta^* > 190\,\mathrm{\mu eV}$ in the diffusive regime.

As mentioned above, from the differential conductance curve it is possible to estimate the induced gap. In particular, if the subharmonic gap structure features follow an harmonic series (the one of MARs), the induced gap is the proportionality coefficient of the series. The correct and complete investigation should look for the structures in the differential conductance (peaks and dips) and follow their evolution changing different parameters as back gate, temperature, and magnetic field, which was beyond the scope of this work.

To interpret the subharmonic gap structures (SGS) shown in panel (b) of Fig. 4.16, it is insightful to analyze each feature. The normal state resistance R_N is reached for $|V| > 2\,\mathrm{meV}$, and several other SGS features are visible, indicated by arrows. These features are present also in the differential conductance spectra below $0.5\,\mathrm{meV}$. Previous investigations of the differential conductance did not report subharmonic gap structures at voltages above $0.5\,\mathrm{mV}$.

To interpret these SGS features, a model is needed that takes into account the entire spectra displayed by the measurement. The model that takes into account the proximity effect in ballistic SNS Josephson junction is the one developed by Aminov et al.

[34]. Their theory predicts in the case of a superconductor with gap Δ_S and a proximity layer with induced gap Δ_N a harmonic series at $eV_n = 2\Delta_N/n$, a series at $eV_n = (\Delta_S + \Delta_N)/n$, and another series at $eV_n = (\Delta_S - \Delta_N)/n$, the latter series appearing as peaks. The height of these peaks depends on the transparency between the superconductor and the normal material. The physical picture behind these resonant voltages, discussed in Sec. 2.3.2, is that the Andreev reflection processes are occurring between the Δ_S and Δ_N interfaces.

To compare the results with their theory, the signal-to-noise ratio is improved by averaging between positive and negative bias values of the differential conductance. The result is displayed in the panel (a) of Fig. 4.17. In panel (b), the theoretical calculated

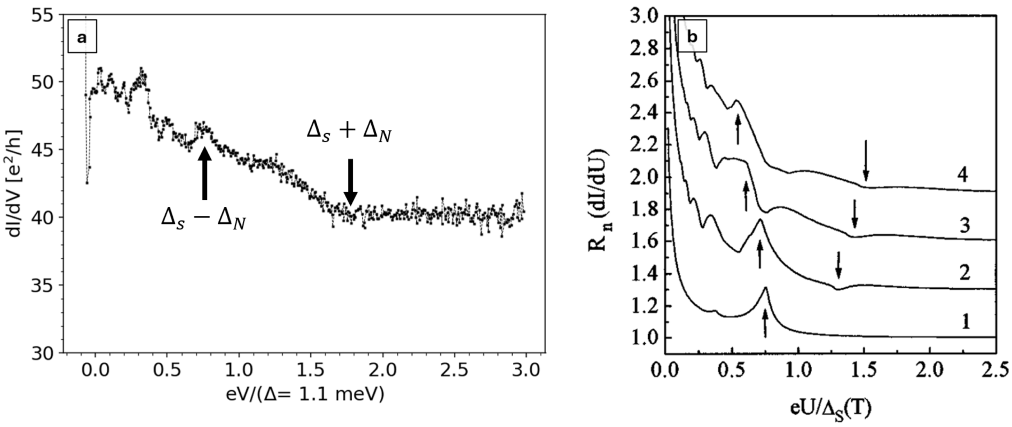

Figure 4.17: **(a)**: Differential conductance data, averaged between positive and negative values. The arrows indicate the value predicted by the theory of Aminov et al. [34] for $\Delta_S - \Delta_N$ and $\Delta_S + \Delta_N$. **(b)**: Normalized differential conductance calculated in [34] including the proximity effect. Curve 1 is at $T = 0$, curve 2 is at $T/T_c = 0.7$, curve 3 at $T/T_c = 0.9$, and curve 4 at $T/T_c = 0.95$. The upward and downward arrow indicate the SGS at $\Delta_S - \Delta_N$ and $\Delta_S + \Delta_N$.

curve for the normalized differential conductance is shown. Indeed, several features are reproduced. From their treatment it follows that the series of SGS at $2\Delta_S/n$ should not be visible and the dip at features reported above for $2\Delta/n$ should be understood as $\Delta_S + \Delta_N$. Comparing the experimental data with the prediction of the theory of Aminov et al., displayed in Fig. 4.17, would imply that, at the temperature of $440\,\mathrm{mK}$ and back gate $20\,\mathrm{V}$:

- $\Delta_S - \Delta_N = 0.75\,\mathrm{meV}$
- $\Delta_S + \Delta_N = 1.7\,\mathrm{meV}$

which means $\Delta_S = 1.22\,\mathrm{meV}$ and $\Delta_N = 475\,\mu\mathrm{eV}$. The Δ_S is in strong agreement with the BCS Niobium gap, while Δ_N confirms the order of magnitude of previous estimates.

4.3 Interference in a magnetic field

In this section I will present experimental results in presence of an external magnetic field perpendicular to the plane defining the SQUID geometry. I will thus show and discuss interference phenomena for both SQUID geometriesa. The physical reasons behind superconducting quantum interference were widely discussed in Sec. 2.4. For convenience, I briefly repeat here the key points:

1. The total supercurrent flowing through the SQUID is the sum of the individual supercurrents carried by each junction, and is a function of the superconducting phase drop across each junction φ_i :

$$I_{\text{SQUID}}(\varphi_1, \varphi_2) = I_1(\varphi_1) + I_2(\varphi_2) \tag{4.5}$$

2. Neglecting the magnetic flux penetrating each Josephson junctions, the superconducting phase drops φ_1 and φ_2 are not independent, but related via the flux quantization condition:

$$\varphi_1 - \varphi_2 = 2\pi\frac{\Phi}{\Phi_0}, \tag{4.6}$$

where Φ is the flux enclosed in the SQUID loop and Φ_0 the superconducting flux quantum. In this way the critical current of the SQUID reads:

$$I_c(\Phi) = \max_{\varphi_1} I_{\text{SQUID}}(\varphi_1, \Phi), \tag{4.7}$$

and is only a function of the enclosed flux. Thus, the specific interference pattern $I_c(\Phi)$ depends directly on the current phase relationship $I(\varphi)$ of the two junctions.

To obtain interference patterns, $V - I$ curves are measured at each applied magnetic field by sweeping the current bias. The magnetic field $\vec{\mathbf{H}}$ is applied perpendicularly to the device plane with a superconducting magnet, and a linear relation is assumed with the flux density, $\vec{\mathbf{B}} = \mu_0\vec{\mathbf{H}}$. In this way, the two quantities are interchangeable and for convenience I will only be using the magnetic flux density, $\vec{\mathbf{B}}$. First the experimental results for the symmetric SQUID are reported, followed by the result on the asymmetric SQUID.

4.3.1 *Symmetric SQUID*

The approach followed in presenting the experimental data is as follows: the impact of the magnetic flux on the loop is discussed separately from its effect on individual junctions. When discussing the SQUID interference caused by the area enclosed by the loop, the magnetic field values are such that the Fraunhofer pattern effects are negligible. [2] Afterward, the single junction interference effects are presented.

Loop Interference In Fig. 4.18, from panel (a) to panel (d) the superconducting quantum interference patterns at four different back gate voltages for the symmetric device are shown, at a temperature $T = 350\,\text{mK}$. The scale bar on the right, indicating the differential resistance, is the same for all four back gate voltages. The differential resistance is calculated by numerical differentiating the voltage along the current direction,

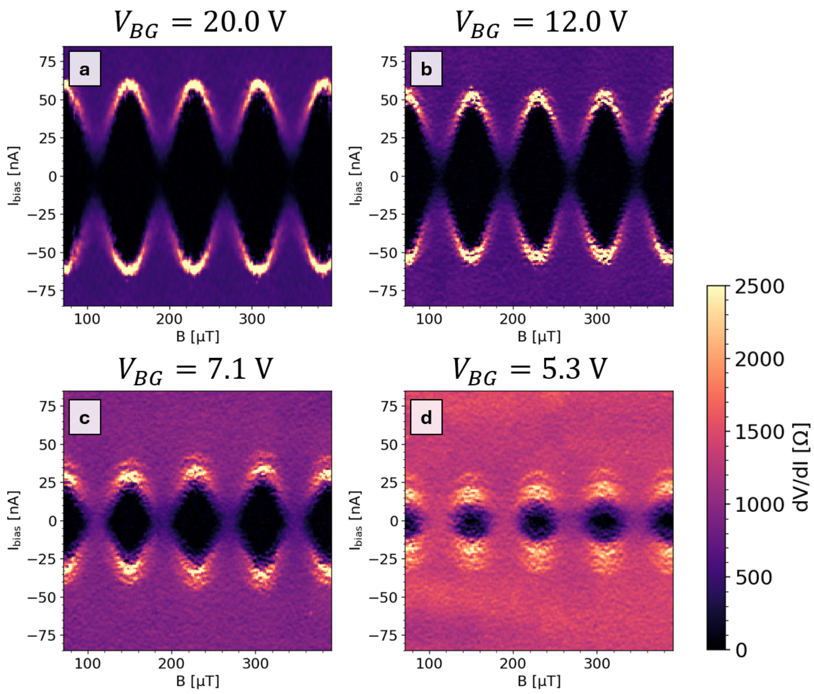

Figure 4.18: **(a)** - **(d)** Color-maps of the differential resistance as a function of the current bias and magnetic field applied perpendicularly to the symmetric SQUID. **(a)**, **(b)**: The two interference patterns show partial destructive interference. **(c)**, **(d)**: Interference patterns showing total destructive interference.

and dividing it by the step used in the current sweep.

The black regions, representing the superconducting regime, are periodically modulated with the applied magnetic field. This behavior is typical of a SQUID interferometer. When the switching currents are higher than $50\,\mathrm{nA}$, the type of switching is sharpest, so that the separation between normal and superconducting regime appears more distinct, while for smaller values such separation appears more blurry as thermal excitations are non negligible and carry finite voltage, making the transition to the superconducting state more rounded. This causes the maxima of the interference pattern to appear more bright, while the transition from the superconducting state to the normal state in the minima is more smooth.

In panel (a) at a back gate of $20\,\mathrm{V}$, for every value of the magnetic field shown, superconductivity is not completely suppressed by destructive interference. In fact, the minima of the interference pattern occur for finite value of current bias. The periodicity of the pattern, ΔB, corresponds to an area $A_{\text{eff}} = \Phi_0/\Delta B \approx 26\,\mu\mathrm{m}^2$. In panel (b), at a back gate of $12\,\mathrm{V}$, this effect is reduced, as the minima in the critical current interference pattern move towards zero current. In addition to that, as the field effect reduces the amplitude of the supercurrent by lowering the back gate voltage, the amplitude of the modulation of the interference pattern, and its average value are reduced. Further

[2] For areas $A = 0.1\,\mu\mathrm{m}^2$, at an applied perpendicular field of magnitude $B = 100\,\mu\mathrm{T}$, the flux penetrating the junction would be $\Phi_{\text{JJ}} = 0.004\Phi_0$.

decreasing the back gate voltage in panel (c), the interference pattern does not only decrease its amplitude, slowly fading away, but it is also modulated to zero, as the minima in the supercurrent amplitude reach zero current.

For the values of magnetic fields in which the interference pattern shows minima causing total destructive interference ($I_c(\Phi) = 0$), there is a balanced situation in which each arm of the SQUID carries equal amounts of supercurrent with opposite sign (i.e., opposite direction), canceling the net supercurrent transport across the device and giving an overall ohmic shape of the $V - I$ curves. This effect is also reported in panel (d), where the region where the $V - I$ curves are ohmic is wider compared the same region in panel (c). In each period, a region with a developed superconducting plateau in the $V - I$ curve corresponds to approximately half the period.

Changing the back gate voltage does not change the periodicity, which remains constant to a value of $A_{\text{eff}} =\approx 26\,\mu\text{m}^2$ for all the explored back gate voltages.

Further investigation of the interference phenomena was performed exploring the temperature behavior of the SQUID pattern. This is reported in Fig. 4.19, where the back gate voltage was fixed at $20\,\text{V}$ and four different temperatures are plotted. As the temperature is increased, the supercurrent amplitude of the interference decreases, along with its modulation. Near $T = 1.55\,\text{K}$ the minima have reached zero current, displaying total destructive interference and giving a symmetric behavior of the device. Since higher harmonics in the CPR tend to decay faster with increasing the temperature[45], the simple physical picture of the sinusoidal CPR is expected to hold at higher temperature, where the observed interference pattern is symmetric.

Before analyzing further the experimental data, it is worth to linger on one important parameter in a SQUID: the effective area. From the figure it is evident how also changing the temperature does not affect the periodicity, which is consistent with the one of the back gate, thus the effective area, calculated with the ratio of the flux quantum to the magnetic field periodicity, $A_{\text{eff}} = \Phi_0/B_{\text{periodicity}}$, has remained constant in every measurement. The observed periodicity in both Fig. 4.18 and Fig. 4.19 corresponds to an effective area $A_{\text{eff}} = 26.1\,\mu\text{m}^2$, which is larger than the geometrical area measured from the SEM images of $A_{\text{geo}} = 13.6\,\mu\text{m}^2$. The difference in the two areas is a factor $A_{\text{eff}}/A_{\text{geo}} = 1.9$. For consistency, it is worth investigating the origin of this difference. One hypothesis that is often proposed to explain this effect is a phenomenon called *flux-focusing*.

This is a peculiar effect caused by having superconducting Nb stripes, which show both zero resistance and also the expulsion of the flux density $\vec{\mathbf{B}}$ from the bulk (Meissner effect). Due to the Meissner effect, the uniform magnetic field $\vec{\mathbf{H}}$ applied to the device corresponds locally to a different distribution of the flux density, which can increase (*focus* , $A_{\text{eff}}/A_{\text{geo}} > 1$) or decrease (*defocus* , $A_{\text{eff}}/A_{\text{geo}} < 1$) the effective magnetic flux enclosed in the superconducting loop. The ratio of the effective area to the geometrical one is called focusing factor and, when its origin lies only in the Meissner effect of

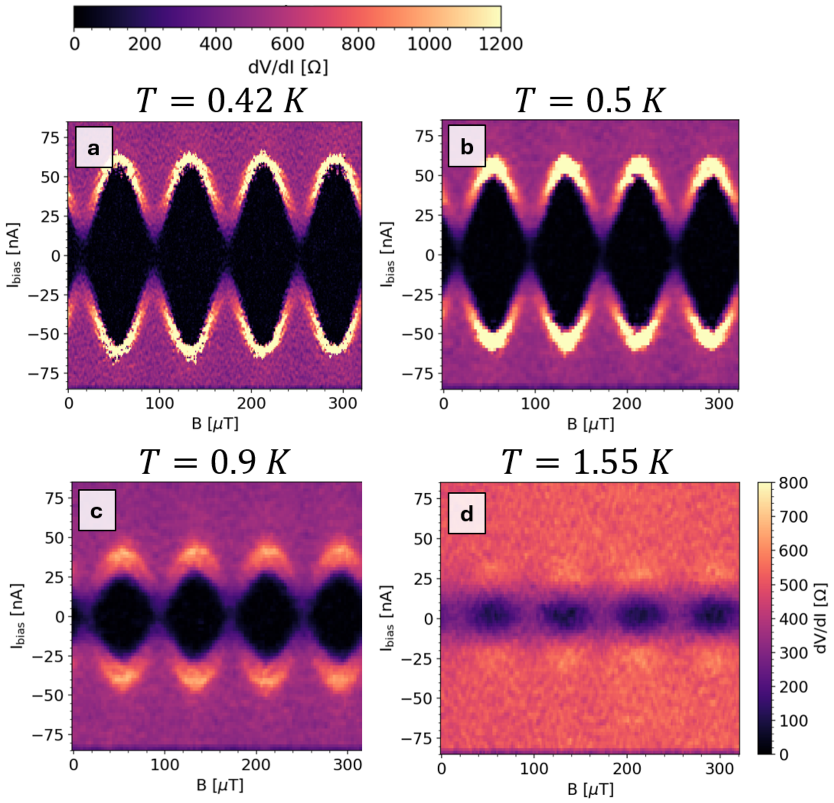

Figure 4.19: **(a)** - **(d)** Supercurrent interference patterns measured at different increasing temperatures, at a back gate voltage of $20\,\mathrm{V}$. Panel **(a)** to **(c)** refer to the color-bar on top, while to increase the visibility, the color-bar for panel (d) was changed and is displayed next to the panel.

the superconductors around the device [3], it can be completely determined from the geometrical features by performing electrostatic simulations with commercial softwares. Since this goes beyond the scope of this work, a qualitative agreement can be sought with a model that contains the essential physics. The model consist in assuming a symmetric screening for the superconducting strips, such that the half the width of the Nb strips deviates the flux density inside the loop and the other half outside the loop. This is displayed in Fig. 4.20, where half of the Nb strip area has been included for the calculation of an effective area that takes into account the focusing effect. The estimated area this way is $\approx 24.2\,\mathrm{\mu m}^2$, in good agreement with the area estimated from the interference pattern $26.1\,\mathrm{\mu m}^2$. Thus, I conclude that deviations from the geometrical area of the interference pattern area are caused by the Meissner effect of the Nb loop, and that at low magnetic field the only cause of the interference is the flux quantization condition (eq. 2.39) occurring in the loop. Hence, SQUID-type interference on the device is demonstrated. Additional insight on the physics of the device is provided by increasing the applied magnetic field, entering in a regime in which one previous assumption–the

[3]There may be cases in which deviations from the expected periodicity happen due to other phenomena, like crossed-Andreev reflections, which here are negligible as the distance between the arm in the interferometer ($4\,\mathrm{\mu m}$) is very large compared to the size of Cooper pairs in Niobium ($\xi = O(100\ \mathrm{nm}) \ll 4\,\mathrm{\mu m}$) [15].

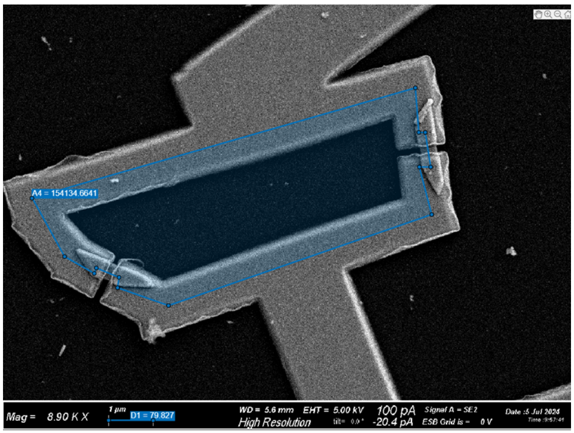

Figure 4.20: SEM image of the symmetric SQUID showing the area to calculate phenomenologically the flux focusing. An effective area of $24.2\,\mu\mathrm{m}^2$ is obtained, in good agreement with the $26\,\mu\mathrm{m}^2$ estimated from the SQUID periodicity. The small difference might arise from the wide Nb electrode pictured in the top half of the image.

magnetic flux penetrating each junction is negligible– is not valid anymore.

Single-Junction Interference So far, the superconducting quantum interference effects reported were caused only by the superconducting loop with tens of square microns of area. With a superconducting flux quantum constant of $\Phi_0 \simeq 2.069\,\mathrm{mT}\,\mu\mathrm{m}^2$ this area corresponds to magnetic fields of hundreds of μT. In addition to that, the only degree of freedom considered for the superconducting phase difference φ was across the two Josephson junctions, assumption limited to lumped, point-like, junctions. Josephson junctions have in fact finite width and length that correspond to small, but non-zero area. The values of areas displayed in Table 4.1, when compared with the value of Φ_0, give the order of magnitude for the magnetic field to produce significant single junction interference phenomena: with areas of fractions of $\mu\mathrm{m}^2$ this corresponds to several mT.

Increasing the value of the applied magnetic field to this order of magnitude unlocks a new degree of freedom for the superconducting phase drop φ that was not considered before: the one parallel to the junction width. Referring to Fig. 4.21, non-negligible flux penetrating the single junction allows for the phase to vary also along the x coordinate such that $\varphi = \varphi\,(x, y)$. As discussed in Sec. 2.3.6, these phase shifts inside the single junction are widely used to probe the supercurrent spatial distribution, and are a strong tool for the investigation of the properties of the supercurrent. When the supercurrent is distributed uniformly inside the junction, these effects manifest in the form of the "Fraunhofer" interference pattern, where a central peak in the supercurrent versus magnetic field is displayed, accompanied with a series of evenly spaced interference minima.

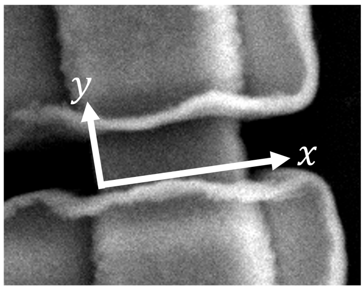

Figure 4.21: Zoom on a single junction of the symmetric SQUID to display the longitudinal (y-axis) and transverse (x-axis) direction to the junction.

In Fig. 4.22(a), the superconducting quantum interference pattern for the symmetric SQUID is shown up to magnetic fields of $20\,\mathrm{mT}$ for a back gate voltage of $20\,\mathrm{V}$ and at a temperature of $350\,\mathrm{mK}$. Zoom-ins at different points are reported in panels (b), (c), and (d), around $-18\,\mathrm{mT}$, $-11\,\mathrm{mT}$, and $-0.5\,\mathrm{mT}$, respectively. The color-bar on top refers to the panels (a), (c), and (d), while for panel (b) another color-bar range was used to increase visibility.

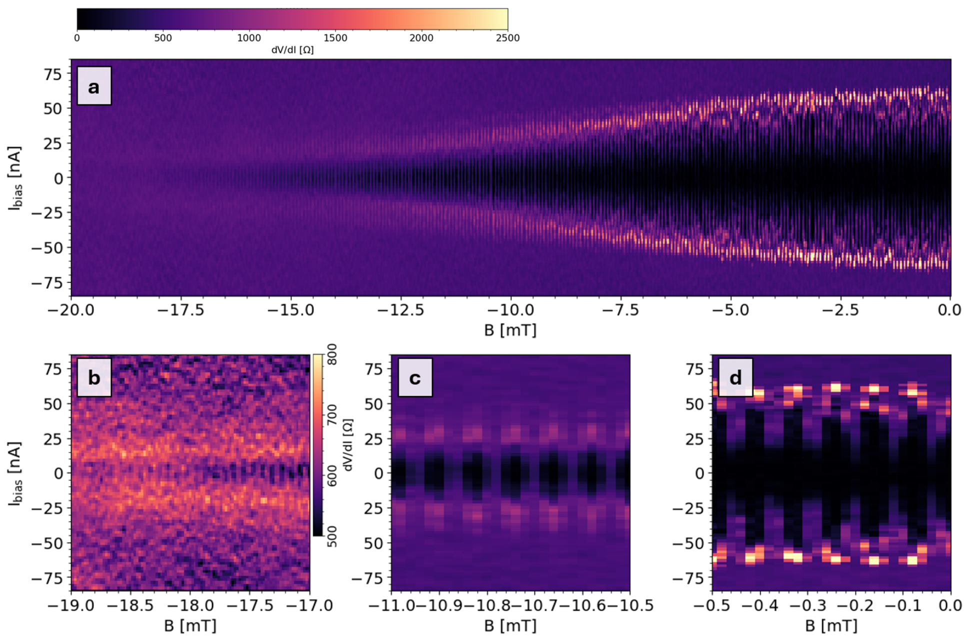

Figure 4.22: **(a),(c),(d)** Differential resistance color-maps referring to the color-bar on top. **(a)** Single junction interference pattern for the symmetric SQUID. **(b)** Zoom near $18.5\,\mathrm{mT}$, where interference disappears, indicating in a more precise way the field at which supercurrents goes to zero. Color bar is changed with respect to the other panels to increase contrast. **(c)** Zoom near $11\,\mathrm{mT}$, showing a balanced SQUID behavior. **(d)** Zoom near $0\,\mathrm{mT}$, showing partial destructive interference in the SQUID pattern already reported in Fig. 4.18 (a).

Since the supercurrent vs. magnetic field is a function of a slow (single junction) component with a rapid (loop) component on top, to avoid artifacts in the visualization of the interference pattern, a proper sampling rate in the magnetic field is required. In fact, a poorly sampled interference pattern might contain fictitious minima related to the information of the area, which, in the end, could lead to misunderstandings about the underlying physics of the system. Following the Nyquist-Shannon theorem, aliasing is avoided by sampling at twice the highest frequency present in the signal. In our terms, this means that *at least* two points per SQUID period are needed. Because of this, measuring a single junction interference pattern with a SQUID modulation on top is an extremely time consuming task; therefore, only a half single-junction interference pattern is measured (from $0\,\mathrm{mT}$ to $-20\,\mathrm{mT}$).

In panel (a), it is observed that superconducting quantum interference happens both at the level of the single junction with a monotonous, Gaussian shape reported in the past [9, 10, 11], and at the level of the superconducting loop. The envelope of the interference pattern presents only one central lobe without any side lobes[4]. Moreover, if two junctions with different areas are connected to form a SQUID, the two different envelopes should be visible simultaneously. Here, however, no notable distortions were observed compared to what is expected from a single Josephson junction, suggesting that the two junction areas are very similar and that the single junction interference minima corresponds to the same area. In fact, according to the SEM images, they are identical within the experimental error, which is negligible in this case.

To calculate the area corresponding to the Fraunhofer minima, which is expected to occur when $B_0 = \Phi_0/A_{\mathrm{JJ}}$, the condition $I_{\mathrm{c,\,envelope}}(\Phi) = 0$ should be satisfied. From panel (b) of Fig. 4.22 the magnetic field at which a interference is lost is estimated to be around $B_0 = 18.5\,\mathrm{mT}$. Converting this value with Φ_0 gives an area of $0.11\,\mu\mathrm{m}^2$, in excellent agreement with the geometrical parameters of both junctions displayed in Table 4.1 which give a geometrical area of $A_{\mathrm{JJ}} = 0.11\,\mu\mathrm{m}^2$. This suggest that at the single junction level, no focusing effect is happening and $A_{\mathrm{JJ,eff}}/A_{\mathrm{JJ}} = 1$.

Further evidence that the estimated area corresponds to the area of *both* the single junctions, rather than just one, is found in the underlying loop interference pattern. As long as SQUID-type modulation is observed, it indicates that supercurrent is flowing through both arms of the SQUID. If the supercurrent were suppressed in one arm, the flux quantization condition would no longer hold, and SQUID modulation would disappear. Additionally, the absence of deviations from the SQUID-type periodicity throughout the entire single junction pattern, along with the consistent effective loop area across all magnetic field values, supports this conclusion. In summary, the analysis confirms that the measured area accurately reflects the collective influence of both junctions, ensuring reliable data interpretation in varying magnetic field conditions.

One interesting observed property is that when the applied magnetic field $|B|$ is greater than $\approx 10\,\mathrm{mT}$, total destructive interference between the two arm is seen, as highlighted by panel (c), in contrast with the partial destructive interference shown in panel (d) and in Fig. 4.18 and Fig. 4.19.

Concluding the experimental overview of the interference data for the symmetric SQUID, it has been demonstrated that SQUID-type interference is present at high values of magnetic field and coexists with the single junction "Fraunhofer" interference pattern. This coexistence highlights the complex interplay between the two types of interference, providing valuable insights into the behavior of the system under varying magnetic conditions. Moreover, the properties of the SQUID interference were shown to be tunable via a back gate. By adjusting the back gate voltage, it was possible to modulate the value of the minima in the interference pattern. At high back gate voltages, the minima exhibited a non-zero current value, indicating partial destructive interference. In contrast,

[4] The range of magnetic fields explored for this device was up to $40\,\mathrm{mT}$, confirming the absence of supercurrent above $20\,\mathrm{mT}$.

at low back gate voltages, the minima reached zero, indicating complete destructive interference. This tunability underscores the versatility of the system and its potential for fine-tuning electronic properties through external controls.

4.3.2 *Asymmetric SQUID*

In the asymmetric SQUID one junction is three times wider than the other. This was achieved by contacting one InSb nanoflag along its wider direction and the other along its narrower direction. As for the symmetric device, the interference versus back gate, temperature, and magnetic field is explored, first focusing on the loop interference, and then analyzing the single junction interference effects.

Loop Interference The interference patterns at $T = 350\,\mathrm{mK}$ for four different back gate values are shown in the four panels of Fig. 4.23. Starting from panel (a), a typical asymmetric interference pattern is shown. For finite values of current bias, a zero differential resistance is present, thus showing supercurrent. The maximum supercurrent that can flow through the device is modulated with the magnetic field on a µT scale, displaying interference. The type of interference displayed corresponds to a partial destructive interference, as the interference pattern does not modulate to zero for any value of the magnetic field shown. When the back gate voltage value is reduced, (panels (b) and (c)) , the modulation amplitude of the interference decreases, disappearing completely at $V_{bg} = 4.0\,\mathrm{V}$.

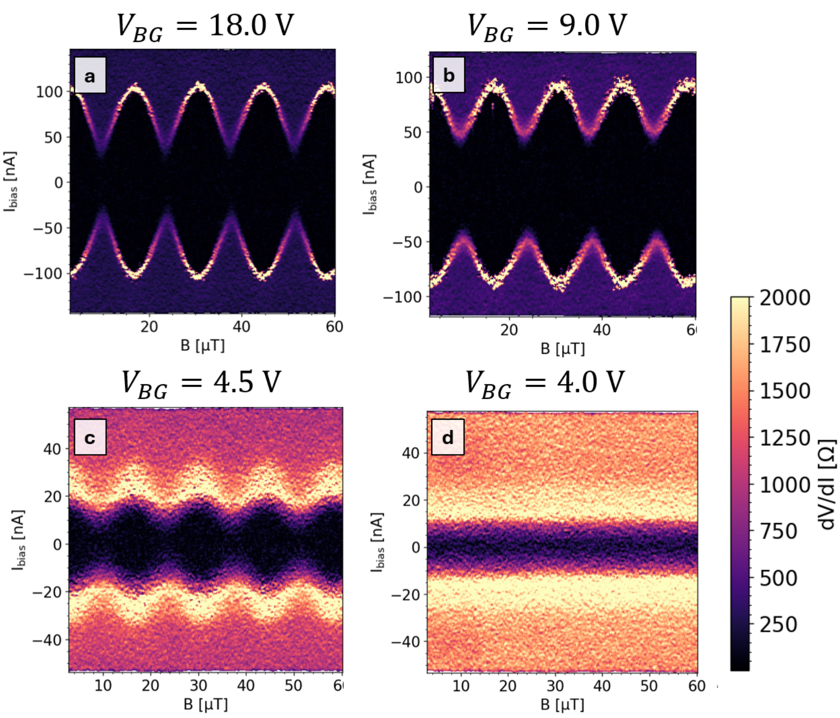

Figure 4.23: **(a)** - **(c)** Asymmetric SQUID interference patterns at different values of back gate. **(d)** SQUID-type interference disappears at a back gate of $4\,\mathrm{V}$, indicating that supercurrent is flowing only through one arm.

When the back gate voltage is below $4.5\,\mathrm{V}$, one nanoflag is pinched off and does not carry supercurrent. In this case, the flux quantization condition does not hold anymore, as the supercurrent flows only in one arm of the SQUID, not enclosing any magnetic flux. For these values of back gate voltage, the asymmetric SQUID behaves as a single Josephson junction since the arm that carries the supercurrent, having zero-resistance, "shunts" the other arm. This remarkable property of the device demonstrates the ability to switch on and off the interference effect with a single back gate.

In a second cool-down of the device, the interference pattern at different temperatures was measured and is shown in Fig. 4.24 at a back gate voltage of $15\,\mathrm{V}$, where both the Josephson junctions carry supercurrent, displaying interference. While the period-

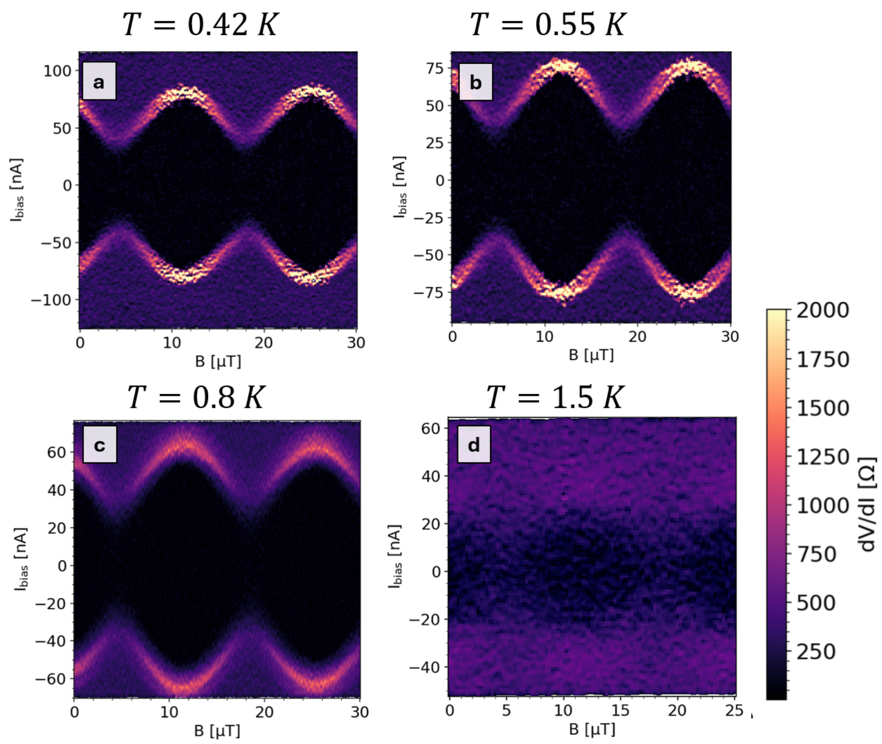

Figure 4.24: **(a)-(d)** Asymmetric SQUID interference patterns at different temperatures. The data displayed are measured during a second cool-down of the device, where the values of the critical current as well as the normal state conductance were reduced with respect to the first cool-down.

icity of the pattern was preserved, the maximum amount of supercurrent was reduced, a probably because the samples was exposed to thermal cycles and stress. The temperature behavior shows that the SQUID interference pattern is asymmetric up to values of $T \simeq 1.5\,\mathrm{K}$, where the minima are near zero current.

The measured magnetic field periodicity for the asymmetric SQUID interference pattern does not change with temperature and back gate also for this device. Using the superconducting flux quantum to convert the periodicity to the effective SQUID area, $A_{\mathrm{eff}} = 149\,\mu\mathrm{m}^2$ is obtained, against a geometrical area of $A_{\mathrm{geo}} = 118\,\mu\mathrm{m}^2$. The resulting ratio between the two area $A_{\text{eff}}/A_{\text{geo}} = 1.26$ is lower with respect to the symmetric SQUID. This is expected, as the ratio of the total Nb strips area, which is the amount that contributes with the flux focusing, with respect to the loop internal area is reduced and as such the focusing factor is also reduced. Repeating the procedure done with the symmetric SQUID, we can consider the focusing to come from half the Nb strips, as shown in Fig. 4.25. An area of $149\,\mu\text{m}^2$ is found, in perfect agreement with $A_{\text{eff}} = 149\,\mu\text{m}^2$ found from the SQUID interference pattern.

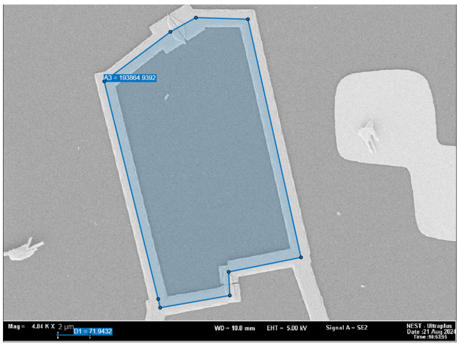

Figure 4.25: SEM image of the asymmetric SQUID highlighting the flux focusing area. The criterion used was to take the path at the center of the superconducting loop. An effective area of $149\,\mu\text{m}^2$ is obtained, in perfect agreement with the area of $149\,\mu\text{m}^2$ obtained from the SQUID pattern periodicity.

Single-Junction Interference For the asymmetric SQUID, when increasing the magnetic field to enter the single-junction interference regime, two different areas are now in "resonance" with the superconducting flux quantum. Referring to the classical Fraunhofer pattern, the Josephson junction with the smaller area will correspond to minima in the interference pattern at higher magnetic fields with respect to the minima in the pattern of the junction with a larger area. The interference pattern of the symmetric SQUID at high values of the magnetic field is shown in Fig. 4.26. From a loop area of $\approx 100\,\mu\text{m}^2$ to a single junction area of $\approx 0.1\,\mu\text{m}^2$, there are three orders of magnitude of difference which, by reciprocity, correspond also to three orders of magnitude of difference in the magnetic field range that characterize the interference effects of these areas. To save time in the measurements, the $V - I$ curves at higher value of magnetic fields are restricted to lower current bias since the supercurrent is low at high magnetic fields In addition to that, only the transition in one direction is measured, from low to high current bias, such that the switching phenomena is the one measured. It has also to be highlighted that the information density carried in the color-map in Fig. 4.26 is too high to be able to distinguish each characteristic, and a process of data manipulation is needed.

On top of a rapid SQUID-type interference pattern, a slowly-varying envelope is modulating the supercurrent amplitude, due to interference happening at the level of the single junctions. To better visualize the non-trivial shape of the envelope, the rapid SQUID-oscillation component has to be factorized out. To achieve this, the maximum value of the switching current for every 10 $V - I$ curves is extracted (that corresponds to $\approx 100\,\mu\text{T}$ steps against a $10\,\mu\text{T}$ SQUID periodicity) and is plotted on top of the dif-

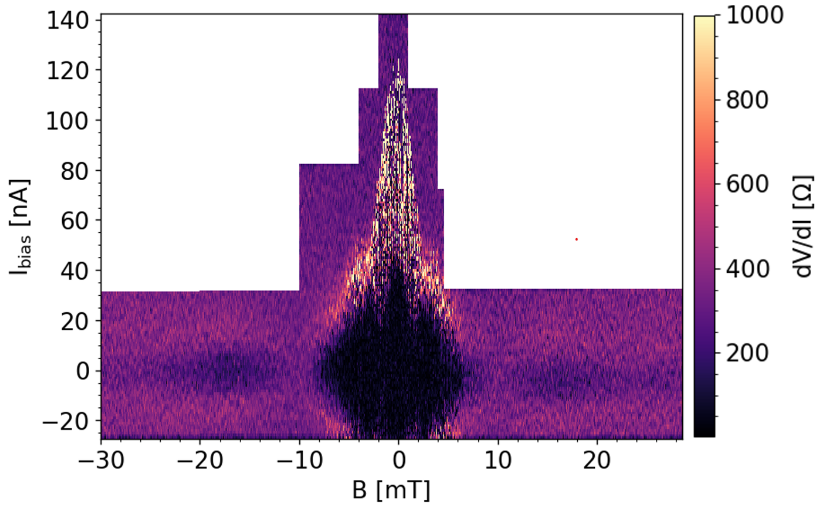

Figure 4.26: Single junction interference pattern of the asymmetric SQUID. Features resembling a full interference minima are present at $B = \pm 10\,\mathrm{mT}$, while a "shoulder" is present near $3\,\mathrm{mT}$.

ferential resistance, at the average magnetic field value of these 10 $V - I$ curves, in the color-map in Fig.4.27. A "shoulder" in the critical current values around $3\,\mathrm{mT}$ is present. A full destructive interference minima is seen at $10\,\mathrm{mT}$.

The clear advantage of the method used to factor out the SQUID oscillation is that it is very simple and allows for a quick visualization of the envelope; the problem is that the feature that one can resolve are limited by the number of points over which the supercurrent maxima are taken. Sharp minima, if present, would not be distinguishable. At the same time, if too few points are used, then the SQUID component would be still visible and appear as spurious, non-physical minima.

Instead of interpreting the SQUID rapid component as a limit to the visualization of the Fraunhofer pattern, is it possible to think of it as a local probe to the working point in the single junction interference pattern: if in the neighborhood of a certain magnetic field SQUID-type oscillations are observed, flux quantization holds and the supercurrent is flowing through both arms. On the contrary, if these oscillations are not observed, then one junction must be in a "Fraunhofer" minima, carrying zero supercurrent and lifting the flux quantization condition in the loop.

In Fig. 4.28, the values of the switching currents from Fig. 4.26 are plotted for two ranges of magnetic field. The switching current was determined as a described in Appendix A. The superimposed high frequency modulation is due to the loop interference. It is clearly visible that for magnetic field $B = 3.0 \pm 0.5\,\mathrm{mT}$, $B = 6.0 \pm 0.5\,\mathrm{mT}$ (panel (a)), and $B = 9.5 \pm 1\,\mathrm{mT}$ (panel (b)), the amplitude of the high frequency interference component is reduced, suggesting that locally one junction carries little supercurrent, and is near a Fraunhofer destructive interference minimum.

The full minima of the interference pattern of the whole SQUID $I_c(B = 9.5\,\mathrm{mT}) = 0$ occur because the area of the two junctions are in ratio $\simeq 3$ one to the other, such

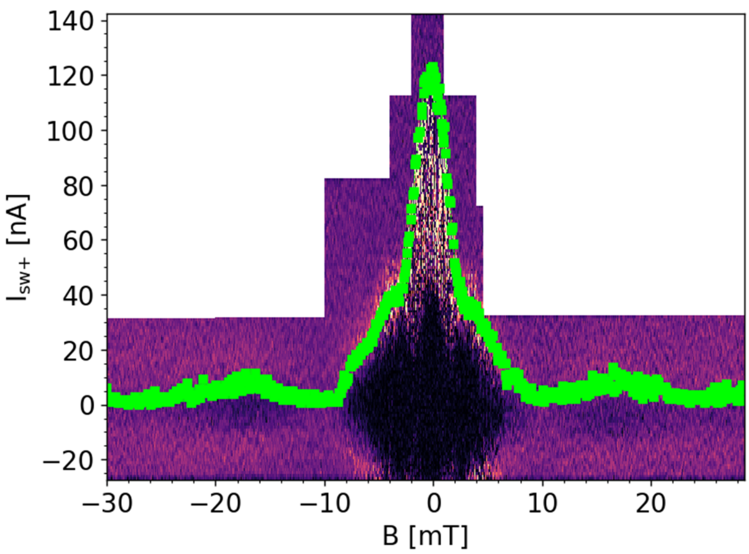

Figure 4.27: Interference pattern of the asymmetric SQUID in the range $(-30, 30)\mathrm{mT}$ with the envelope critical currents (green squares) superimposed, which highlight the single junctions interference. The non-trivial shape is attributed to the two single junctions of different area.

that the first minima of the smaller junction corresponds (within a certain range) to the third minima of the other. Most notably, the third minimum was never observed for Josephson junctions made with InSb nanoflags. The SQUID "interferometry" provides strong evidence that, in the alternative geometry where the Niobium contact is made along the wider direction of the nanoflag, these type of Josephson junctions can display multiple minima.

It is worth underlining that when one arm is in a destructive interference condition, the total critical current of the device can still be nonzero, as the other junction is not expected to have necessarily suppressed the supercurrent. This was also underlined in Sec. 2.4.4, where the expected single junction interference pattern was shown in Fig. 2.15 for an ideal SQUID with the same parameters of the asymmetric SQUID fabricated in this thesis. The analytical model developed assumed for simplicity sinusoidal CPRs, but the overall trend predicted is confirmed here.

The motivations given above allow to conclude the reduction in the modulation amplitude of the SQUID-type interference can be attributed to the minima in the "Fraunhofer" pattern of each junction.

Looking at the geometrical parameters given in Table 4.1, the two areas of $0.44\,\mu\mathrm{m}^2$ and of $0.14\,\mu\mathrm{m}^2$ are in a ratio:

$$R_{\mathrm{geo}} = A_{\mathrm{JJ1}}/A_{\mathrm{JJ2}} = 3.14$$

Looking at the ratio of the first minima of the smaller junction, $B = 9.5 \pm 1\,\mathrm{mT}$ to the first minima of the greater junction $B = 3.0 \pm 0.5\,\mathrm{mT}$, the following value is obtained:

$$R_{\mathrm{eff}} = A_{\mathrm{eff,1}}/A_{\mathrm{eff,2}} = B_{0,\mathrm{JJ2}}/B_{0,\mathrm{JJ1}} = 3.16 \pm 0.6$$

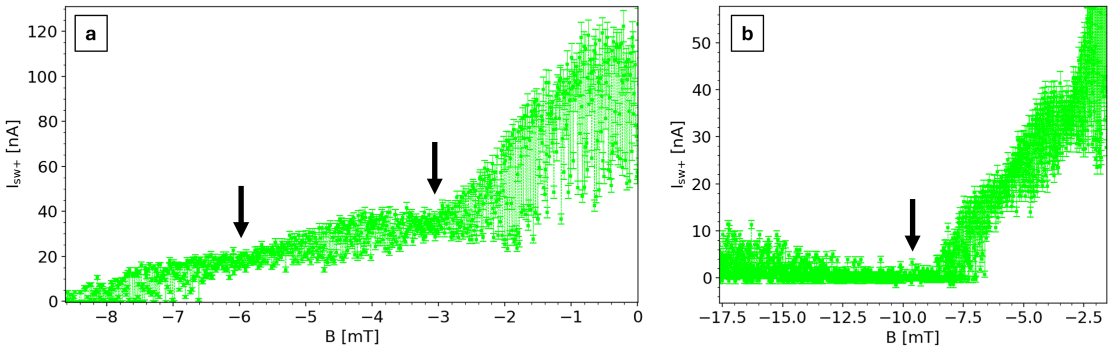

Figure 4.28: **(a)**, **(b)** Critical (switching) currents extracted from the interference pattern shown in Fig. 4.26, showing the high frequency (SQUID) modulation with a low frequency (junction) envelope. **(a)** Zoom of the data near the central lobe, where a reduction in the amplitude of the SQUID modulation is indicated by arrows at $B = -3.0 \pm 0.5\,\mathrm{mT}$ and $B = -6.0 \pm 0.5\,\mathrm{mT}$. **(b)** Zoom near the first full minima indicated by the arrow at $B = 9.5 \pm 1\,\mathrm{mT}$.

The ratio between the effective areas R_{eff} is in optimum agreement with the ratio between the geometrical areas R_{geo}. This further supports that the estimated areas from the Fraunhofer area the effective area of the two junction.

Furthermore, $A_{\text{eff,JJ1}}/A_{\text{geo,JJ1}} = 1.55$ and $A_{\text{eff,JJ2}}/A_{\text{geo,JJ2}} = 1.56$. Both the effective areas are a factor ≈ 1.5 larger. It is also possible for Josephson junction to display flux-focusing, depending on the geometry [50].

Measurements on the asymmetric device confirmed the findings of the symmetric SQUID. Moreover, in the asymmetric geometry, control of the presence of interference is demonstrated with the action of a single gate that exploits the different response of the two nanoflags. Thanks to SQUID interferometry, it has also been possible to distinguish the single junction interference effects even with 3 order of magnitude in difference in area, as SQUID-type interference is resilient at high magnetic fields. Additionally, the measurements suggested multiple minima in the "Fraunhofer" pattern of the wider junction, a feature that was never reported so far, confirming the impact of the length-over-width ratio in determining the behavior of the critical current under the action of a magnetic field.

4.4 Josephson Diode Effect in symmetric and asymmetric SQUIDs

In this section, the experimental results regarding the investigation of the superconducting diode effect in the SQUIDs are presented. This newly born research field is currently under active investigation, and a comprehensive physical understanding has yet to be established. Therefore, this section will focus on reporting the key results, commenting on the experimental features, and discussing what can be inferred about the properties of the devices.

4.4.1 *Superconducting Diode Effect in symmetric and asymmetric SQUIDs*

In the measurement of the interference patterns for both symmetric and asymmetric SQUIDs, the $V - I$ curves were swept in both positive and negative directions, allowing for the acquisition of transitions related to $I_{sw,+}$ and $I_{sw,-}$. In the resulting SQUID interference patterns, it is found that the minima are slightly shifted, indicating the presence of the Josephson diode effect. Since this effect is difficult to visualize from the previously presented figures, Fig. 4.29 provides a zoomed-in view of the minima at a back gate voltage of $15\,\mathrm{V}$ and T = $350\,\mathrm{mK}$ for the asymmetric SQUID.

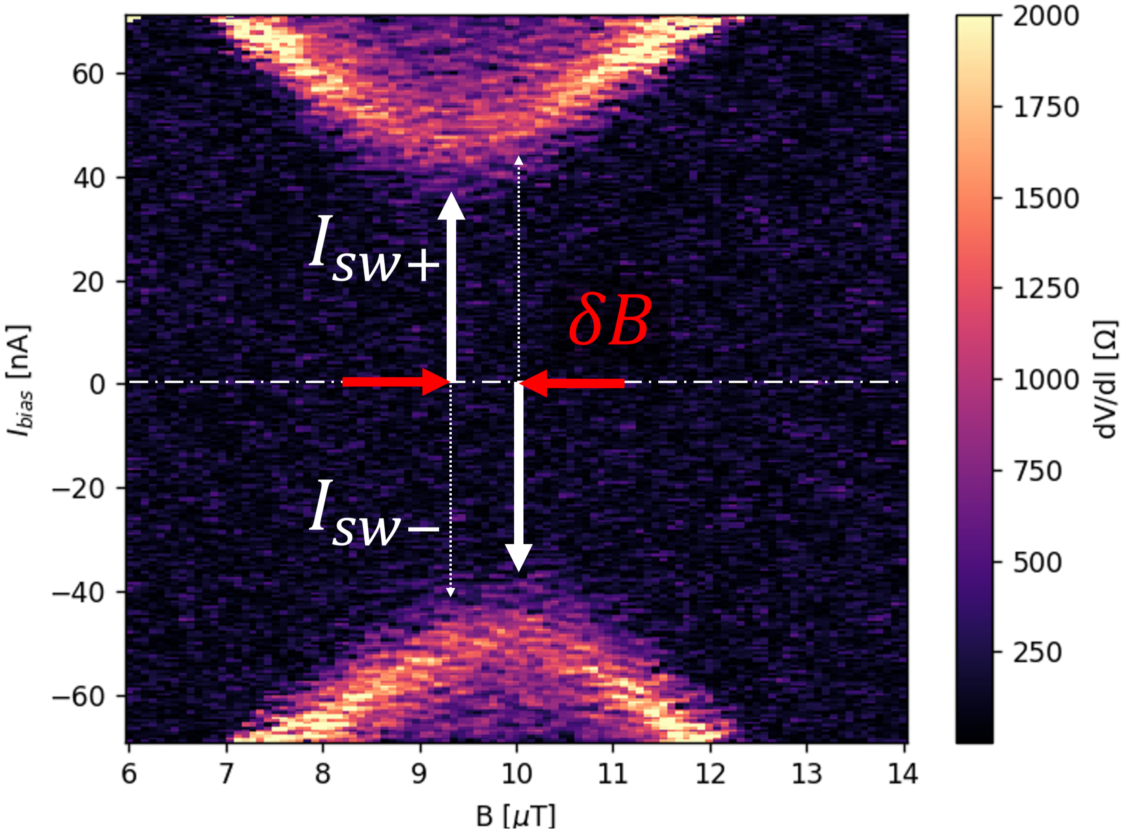

Figure 4.29: Zoom in around the minima in the interference pattern of the asymmetric SQUID, measured at a back gate voltage of $15\,\mathrm{V}$ and T = $350\,\mathrm{mK}$, highlighting the shift in the two minima δB.

The two minima are distinctly shifted by $\delta B \simeq 1\,\mu\mathrm{T}$, which is a very small quantity but still noticeable. To understand explicitly the presence of the Josephson diode effect, consider the following: if the upper switching current $I_{sw,+}$ is at its minimum value for a certain value of the applied magnetic field ($\approx 9\,\mu\mathrm{T}$ in the figure), the shift in the magnetic field is such that the switching current in the other direction $I_{sw,-}$ is not at a minimum. This is a situation for which $I_{sw,+} \neq I_{sw,-}$, corresponding to the diode effect for current bias values:

$$|I_{\text{bias}}| \in [I_{sw,+}, -I_{sw,-}) \tag{4.8}$$

In fact, if the curren bias $|I_{\text{bias}}| > |I_{sw,-}|$, the SQUID is normal in both directions, while if the current bias is such that $|I_{\text{bias}}| < I_{sw,+}$ the SQUID is superconducting in both directions. In the situation in-between, the device is normal in the positive current direction

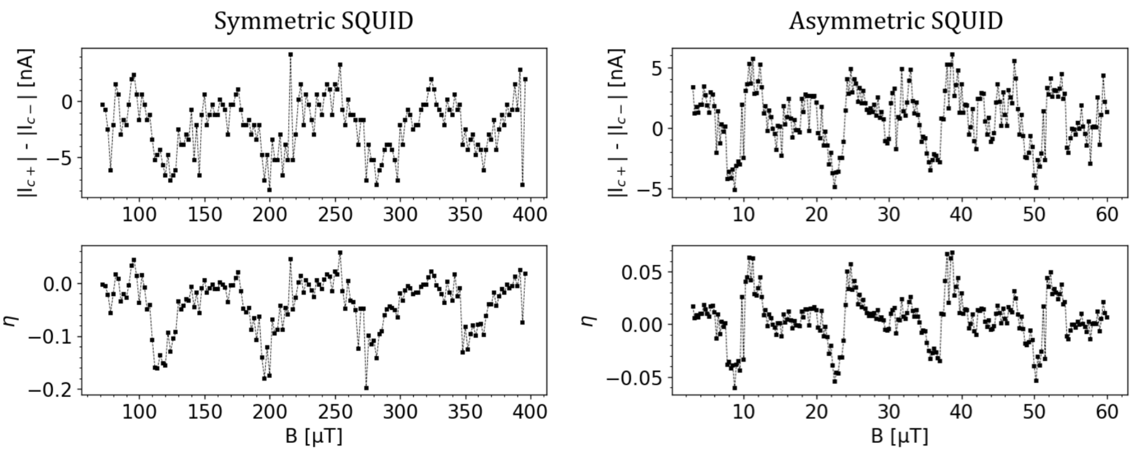

Figure 4.30: **Left:** Demonstration of the Josephson Diode Effect in the symmetric SQUID. In the top image the difference between the two critical current is displayed. On the bottom image the corresponding rectification coefficient η The measurement refers to a back gate voltage of $20\,\mathrm{V}$ and a temperature of $350\,\mathrm{mK}$. **Right:** The same for the asymmetric SQUID at a back gate voltage of $18\,\mathrm{V}$ and a temperature of $350\,\mathrm{mK}$.

and superconducting in the other, realizing a superconducting diode for that particular value of magnetic field.

To characterize how the JDE manifests in both the devices, the difference between the magnitude of the critical currents[5] in the positive and negative directions was calculated and is plotted on the top image in Fig. 4.30, with the rectification coefficient η, defined by eq. 2.61, and plotted on the bottom image. The situation for the symmetric SQUID is represented on the left, and for the asymmetric on the right. I underline that no smoothing procedure or running average was performed to alter the data, and the only procedure that has been done is the extraction of the switching and retrapping currents with the method described in Appendix A.

Beginning the description with the symmetric SQUID, both the absolute difference of the critical currents and the rectification coefficient exhibit a periodic behavior that is consistent with the periodicity of the SQUID. This consistency confirms that the observed phenomena are not caused by noise. The absolute difference $|I_{c+}| - |I_{c-}|$ is modulated by the magnetic field within a range of $5\,\mathrm{nA}$. Notably, there are magnetic field values where this difference is positive, and fields where this difference is negative. This variation directly affects the rectification coefficient, indicating that the magnetic field can change the polarity of the symmetric SQUID diode. The rectification coefficient does not appear to be symmetric with respect to the zero current, a feature that needs a more detailed investigation.

The asymmetric SQUID confirms the modulation of the absolute difference between

[5]To improve the signal to noise ratio, averaging between switching and retrapping current is performed, since no notable difference is present between those two quantities and JDE is seen on *both* the retrapping and switching currents.

the two critical currents, $|I_{c+}| - |I_{c-}|$, to be within $-5 - 5\,\mathrm{nA}$ range, with the important difference that the periodic modulation period changes to the μT scale, in agreement with the asymmetric SQUID effective area. The rectification coefficient shows a remarkable match with what is observed for Josephson junctions (Fig. 2.20), but with a periodic behavior. In this case, too, the rectification coefficient can be tuned by the magnetic field, altering the polarity of the asymmetric SQUID diode and achieving values around 5%.

From the back gate characterization of the SQUID interference pattern, the gate-tunability of the Josephson diode effect can be investigated. As discussed in [82], the field effect modulation of the diode effect provides evidence of the semiconducting channel's role in giving rise to this phenomenon. In Fig. 4.31 the back gate modulation of the JDE is presented. For clarity, each curve was shifted by $10\,\mathrm{nA}$.

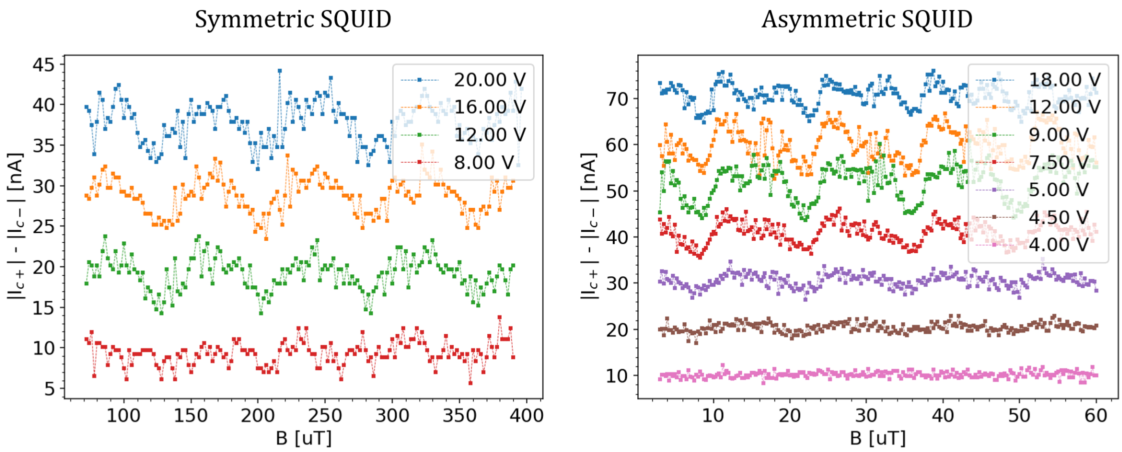

Figure 4.31: Back gate modulation of the Josephson Diode Effect. The critical current reported refers to $T = 350\,\mathrm{mK}$.

In the symmetric SQUID, the amplitude of the modulation of the difference $|I_{c+}| - |I_{c-}|$ remains unchanged when tuning the back gate from $20\,\mathrm{V}$ to $12\,\mathrm{V}$, but is suppressed at $8\,\mathrm{V}$. This is a key property, since at a backgate voltage of $8\,\mathrm{V}$, the type of SQUID interference pattern (similar to Fig. 4.18, panel (c)) transitions from not modulating completely to zero, to showing total destructive interference. To exhibit the Josephson diode effect, a properly asymmetric SQUID is required, with the two arms having different critical currents. The asymmetric SQUID consistently exhibits the Josephson diode effect at all the back gate voltage explored, and only diminishes to zero at a back gate voltage of $4\,\mathrm{V}$. At this specific back gate voltage, no interference is observed in the corresponding SQUID pattern (Fig. 4.23, panel (d)). This occurs because no supercurrent is flowing in one of the two arms of the SQUID, leading to the absence of the JDE.

It is important to emphasize that the Josephson diode effect displayed is not solely a property arising only from superconductors. It is possible to argue that if the supercurrent is pinched off, then the diode effect would naturally not be visible, since there is no supercurrent at all. However, this is not the case, as evidenced both by the symmetric SQUID and the asymmetric SQUID. When in the first case the interference pattern becomes symmetric, supercurrent can still flow through the device. In the latter case, when the supercurrent in one junction is suppressed, supercurrent flow is still present in the other arm. Both arguments confirm that the JDE is indeed attributable to the distinct behavior of the entire SQUID, including the semiconducting regions.

Having determined that the JDE comes from the key role of the InSb nanoflags, to understand the role of each arm in the rectification it is possible to compare the rectification coefficient at each magnetic field with the SQUID interference pattern. Fig. 4.32, top image, shows the color-map of the rectification coefficient of the asymmetric SQUID against magnetic field and back gate voltage, while the bottom image shows the upper switching current of the SQUID interference pattern for reference. Comparing the two

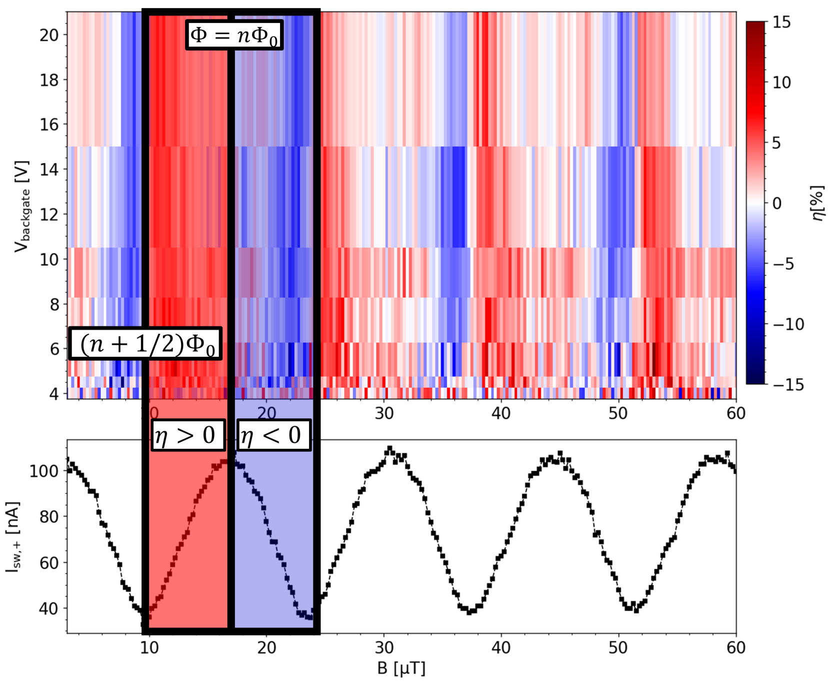

Figure 4.32: Color map of the rectification coefficient for the asymmetric SQUID, as a function of the back gate voltage (y-coordinate) and magnetic field (x coordinate). The fluctuations near $V_{bg} = 4\,\mathrm{V}$ are due to noise. In the bottom image the upper switching current as a function of the magnetic field.

it is possible to observe that when the magnetic field is such that the SQUID pattern is in the minima[6], then η changes sign. This observation is consistent with the theoretical predictions expected for SQUIDs: three conditions should be present *at the same time* for a SQUID to be able to display JDE [86]:

1. The external flux should not be equal to a an integer multiple of half the flux quantum: $\Phi \neq n\frac{\Phi_0}{2}$
2. The single junction transmissions should not be equal: $\tau_1 \neq \tau_2$

[6]When there is JDE, the minima is not exactly in, e.g., $\Phi_0/2$. Referring to Fig. 4.29, it is shifted by $\pm\delta B/2$, depending if the positive or negative branch of the interference pattern are considered. In the case discussed, the difference is less than $0.5\,\mu\mathrm{T}$

3. At least one Josephson junction needs to be highly transmitting to have a sizable higher harmonic content in the CPR.

Confirming the expectations that the Josephson junctions based on InSb nanoflags are highly transmissive and present higher harmonics content in the CPR. [10].

Concluding this section, it is emphasized that the Josephson diode effect (JDE) has been unequivocally demonstrated in both symmetric and asymmetric SQUID geometries. A rectification coefficient of up to 5% was observed, and this coefficient was tunable based on the magnetic field, in a consistent manner with the field periodicity of the SQUID. This tunability allows for the reversal of the SQUID's diode polarity by changing the sign of η on a μT scale. Moreover, the diode effect was found to be gate-tunable, a key property in attributing the origin of this effect to the InSb nanoflags (point #2). This gate tunability further supports the presence of non-sinusoidal current-phase relationships within these systems (point #2 + point #3), providing additional proof of the role of the semiconducting channel in influencing the JDE.

4.5 Discussion

4.5.1 *Interference Model*

Fitting the interference patterns $I_c(\Phi)$ with the correct model requires an a-priori knowledge of *both* current phase relationships $I_1(\varphi_1),\ I_2(\varphi_2)$ of the two junctions.

To date, no measurements are available for the CPR of InSb nanoflags. Therefore, the most simple model that describes SQUIDs is the sinusoidal one, presented in Sec. 2.4. Because of its simplicity, it is effective in providing a first description of the SQUIDs. The following expression is used:

$$I_c\left(B, I_{c1}, I_{c2}, A, \delta\right) = \sqrt{\left(I_{c1} - I_{c2}\right)^2 + 4 I_{c1} I_{c2} \cos\left(\pi \frac{BA}{\Phi_0} + \delta\right)^2} \tag{4.9}$$

This relation has 4 free fit parameters: I_{c1} and I_{c2} are the magnitudes of the critical currents of the two Josephson junctions, A is the effective loop area resulting from the periodicity of the SQUID pattern, and δ is a phase parameter used to "center" the pattern, taking into account effects of finite magnetization (rigid shifts in the magnetic field B).

An analysis of the data with this model is useful for an additional reason. The two parameters I_{c1} and I_{c2} are related to two variables important for the SQUID interference pattern $I_c(\Phi)$: the modulation amplitude $\Delta I_c = \max I_c(\Phi) - \min I_c(\Phi)$ and the average value $\langle I_c(\Phi)\rangle_\Phi$, where $\langle , \rangle_\Phi$ denotes the average over one magnetic flux period. The connection between these parameters ($I_{c1} \geq I_{c2}$) is the following:

$$I_{c1} = \langle I_c(\Phi)\rangle_\Phi \tag{4.10}$$

$$I_{c2} = \frac{\Delta I_c}{2} \tag{4.11}$$

By fitting with the sinusoidal SQUID model, I also obtain an estimate of these two quantities, that are characteristic of the interference pattern.

4.5.2 *Sinusoidal model - symmetric SQUID*

Back gate dependence The fit procedure using eq. 4.9 was performed on the dataset presented in Sec. 4.3.1. The fits are performed using a non-linear least-square method, using the optimization routine offered by the SciPy function *curve_fit*. One example of the fit procedure applied to the interference pattern of the symmetric SQUID at a back gate voltage of $20\,\mathrm{V}$ and at a temperature of $350\,\mathrm{mK}$ is reported in Fig. 4.33. The top image shows the fit (red curve) superimposed on the switching currents (black squares). In the bottom image the residuals are displayed.

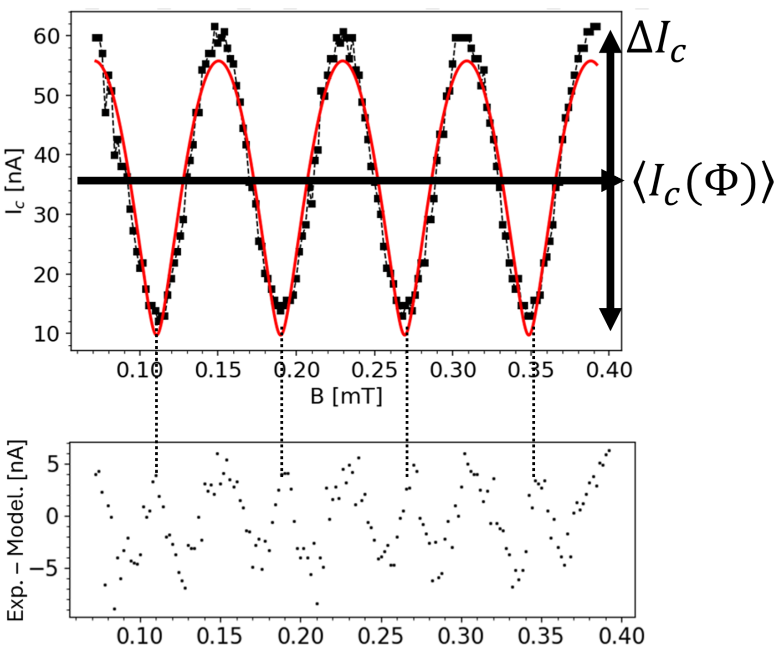

Figure 4.33: **Top**: Switching currents (black squares) for the data presented in Fig. 4.18 (a), with the superimposed fit (red) using eq. 4.9. **Bottom**: Residuals of the fit, displaying an even distribution around zero current, but an overall oscillatory behavior.

The optimal parameters estimated are:

- I_{c1} = $32.8 \pm 0.4\,\mathrm{nA}$
- I_{c2} = $23.0 \pm 0.5\,\mathrm{nA}$
- A = $26.1 \pm 0.1\,\mu\mathrm{m}^2$
- δ = $0.32 \pm 0.02\,\mathrm{rad}$

An overall good agreement is found between the data and the model. The residuals of the fit displace evenly around $0\,\mathrm{nA}$ in a $5\,\mathrm{nA}$ range, but are not randomly scattered, but show an oscillatory behavior, feature that the whole dataset presented.

This oscillatory behavior comes from the fact that the single $\sin(\varphi)$ component in the CPR is not able to capture all the physics of the SQUID pattern.

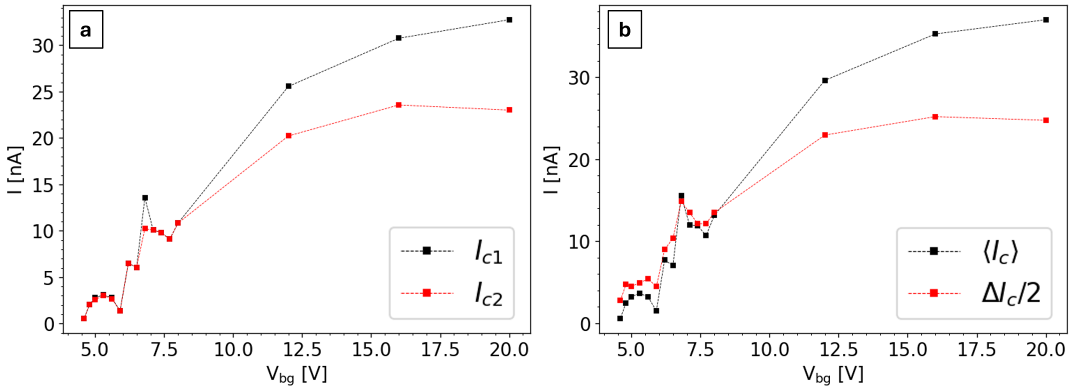

Figure 4.34: **(a)** Critical currents obtained from the fitting procedure. Two transport regime for the SQUID are identified: unbalanced above $V_{bg} = 8\,\mathrm{V}$ and balanced below. **(b)** Average value of the interference pattern and half modulation amplitude.

The fit procedure discussed, when repeated for different values of back gate, allows to reconstruct the transfer curves for the supercurrent of each junction. As shown in panel (a) of Fig. 4.34, this allows to determine the transport regime of the device, from an unbalanced transport regime above $V_{bg} = 8\,\mathrm{V}$ (where one arm carries more supercurrent than the other), to a balanced configuration below $8\,\mathrm{V}$ where the device behaves as a symmetric interferometer. Panel (b) displays the average value and half the modulation amplitude. These values are obtained independently from the fit. The trend, which has some fluctuations due to noise in the data, reproduces the results of the fit confirming the equivalence in the description: the interferometer is unbalanced above $V_{bg} = 8\,\mathrm{V}$ and balanced below.

Supposing I_{c1} and I_{c2} represent the critical currents of the two arms, then the width of the nanoflags measured from the SEM images allows to estimate the maximum critical current density of each junction. At a back gate voltage of $20\,\mathrm{V}$, one arm has a value $I_{c1}/W = 86\,\mathrm{nA}\,\mu\mathrm{m}^{-1}$ and the other of $I_{c2}/W = 61\,\mathrm{nA}\,\mu\mathrm{m}^{-1}$.

Temperature dependence Looking at the temperature behavior of the critical currents can give additional information on the transport regime of the two junctions. In Fig. 4.35, the temperature trend of the two fit parameters I_{c1} and I_{c2} is reported. A similar decay in the $I_c(T)$ curve is found for both junctions, which is rather linear below $0.8\,\mathrm{K}$, and then presents a smaller rate of decay, in a convex-like fashion.

It has been discussed that the decay of the critical current with temperature has a significant dependence length of the Josephson junction [115]. For long ballistic junctions, the critical current decreases exponentially with increasing temperature, following the relation $I_c \propto \exp\left(-k_b T/\delta E\right)$ over a wide temperature range, where δ_E is a characteristic energy scale. In short junctions, the critical current follows a different temperature dependence, and when $k_b T$ becomes much smaller than the induced gap, it saturates at a value proportional to the product of the induced gap Δ^* and the number of transverse modes in the junction. It has to be underlined that in the past a crossover between a short-junction regime and a long-junction regime was observed on Josephson junctions

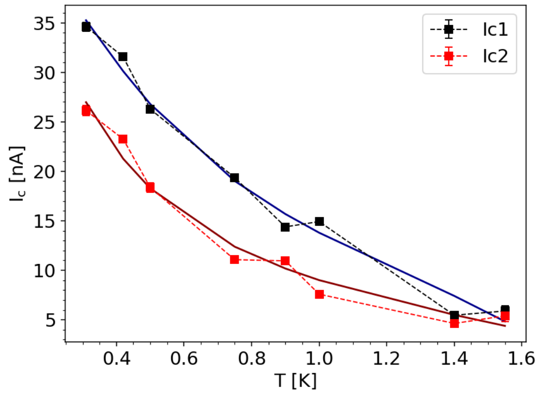

Figure 4.35: Behavior of the critical current obtained from the fit with temperature. A similar trend is displayed by both critical currents, which confirm the symmetric physical behavior of the two junctions. The fit, performed with the KO-2 model, gives $T^*_{c1} = 1.81\,\mathrm{K}, T^*_{c2} = 2.0\,\mathrm{K}$.

similar to the ones reported in this thesis [10, 116]. The long junction regime was present at temperatures well below $T = 350\,\mathrm{mK}$, such that at the temperature explored here, the long junction regime is already suppressed and the devices are described by a short junction model. Here we assume that the I_{c1} and I_{c2} calculated from the interference pattern with the sinusoidal models are the critical current of the two junctions, and to use this information to fit the temperature trend with a well-known model. The CPR in the short ballistic junction limit can be described by the Kulik-Omelyanchuk II model [10, 117], in which the transmission coefficient of each mode is substituted with one averaged transmission τ:

$$I(\varphi) = \frac{Ne\Delta^*}{2\hbar} \frac{\tau \sin\varphi}{\sqrt{1-\tau\sin{(\varphi/2)}^2}} \tanh\left[\frac{e\Delta^*}{2k_bT}\sqrt{1-\tau\sin{(\varphi/2)}^2}\right], \tag{4.12}$$

where the gap has the BCS temperature dependence

$$\Delta^*(T) = \Delta^*(0)\tanh\left[1.74\sqrt{(T^*_c/T)-1}\right]$$

At 20 V of back gate voltage the device was shown to be in a crossover regime between ballistic and diffusive transport. Hence, the ballistic model for the CPR and not the diffusive model was chosen. From a numerical point of view, having the product of N, Δ^*, τ in the prefactor can lead to complication in the optimization of the parameters. Therefore, the prefactor is changed to I_0, as was done in [11], while keeping the temperature dependence of the induced gap. The results of the two series of fit are displayed in Fig. 4.35 as the continuous solid line. The only parameter which has the same estimate regardless of the fit details is T^*_c, which takes the following values:

- $T^*_{c1} = 1.81 \pm 0.03\,\mathrm{K}$
- $T^*_{c2} = 2.0 \pm 0.1\,\mathrm{K}$

The values found are compatible with $T^*_c = 1.85\,\mathrm{K}$ reported in [10].

4.5.3 *Sinusoidal model - asymmetric SQUID*

Back gate dependence Fig. 4.36 shows the fit procedure to the data at a back gate voltage of $15\,\mathrm{V}$ and at a temperature of $350\,\mathrm{mK}$ with eq. 4.9 for the asymmetric SQUID.

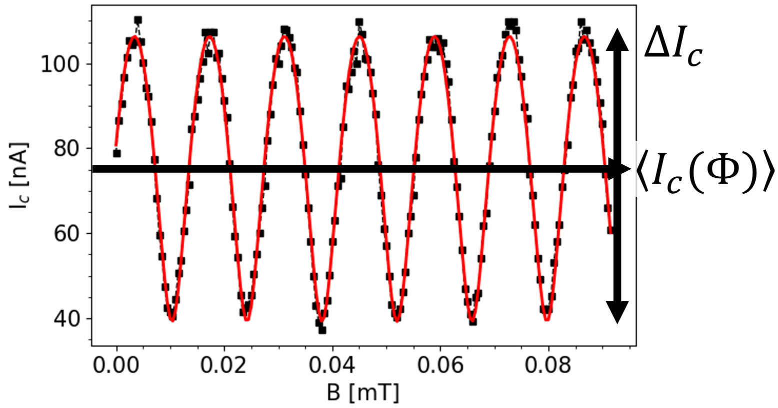

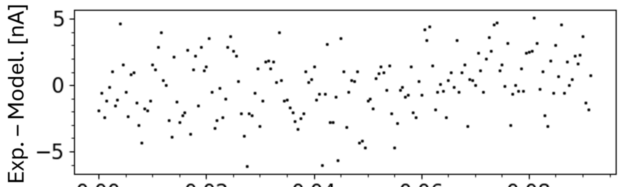

Figure 4.36: **Top**: Switching currents (black squares) for the data presented in Fig. 4.23 (a), with the superimposed fit (red) using eq. 4.9. **Bottom**: Residuals of the fit, evenly distributed around zero current.

The optimal parameters are:

- $I_{c1} = 72.8 \pm 0.2\,\mathrm{nA}$
- $I_{c2} = 23.0 \pm 0.3\,\mathrm{nA}$
- $A = 149.0 \pm 0.1\,\mu\mathrm{m}^2$
- $\delta = 2.37 \pm 0.01\,\mathrm{rad}$

In this case, a better agreement is found between the data and the model, with respect to the symmetric SQUID, as highlighted from the plot of the residuals. The trend of the two parameters I_{c1} and I_{c2}, is plotted versus the back gate voltage in the left image of Fig. 4.37. Both junctions show critical current modulation with the back gate voltage below $V_{bg} = 12\,\mathrm{V}$, and in one arm the critical current goes to zero at a back gate value of $4.0\,\mathrm{V}$.

It is certainly worth trying to assess which is the junction that pinches off the supercurrent. However, one problem that could arise in trying to do so is that one fit parameter, for example I_{c1}, for some value of the back gate could refer to one arm and, for some other voltages, could refer to the other. This problem should be highlighted by a crossing in the two critical current values. This is not observed in Fig. 4.37 and

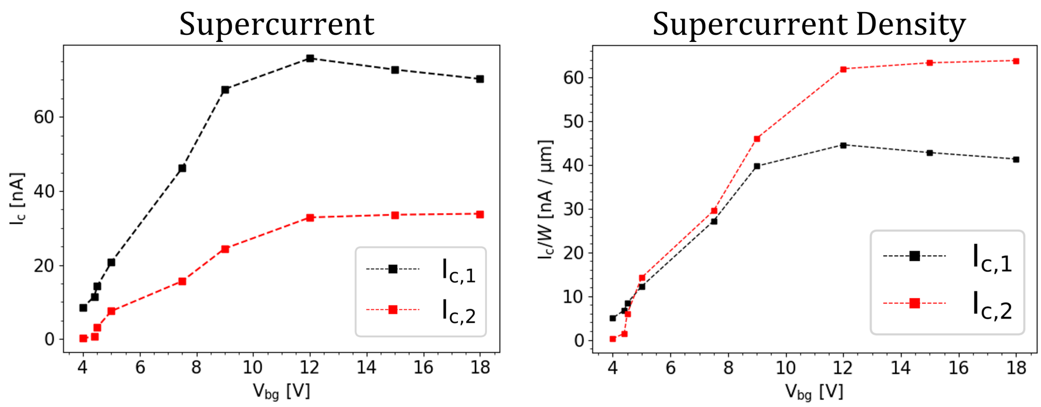

Figure 4.37: **Left**: Critical current values as a function of the back gate voltage, showing modulation. No crossings are observed between the two parameters, hence the parameters belong to the same junction for every back gate value. **Right**: Critical current densities calculated thanks to the non crossing behavior. The narrow junction presents higher supercurrent density, and pinches off at $V_{bg} = 4\,\mathrm{V}$.

is possible to state that, for example, I_{c1} is the critical current of the same junction for every value of the back gate plotted (the same applies to the other arm with I_{c2}).

Most likely, the high-I_c junction is the one $1.7\,\mu\mathrm{m}$ wide and the small-I_c junction is the one with the smaller width of $0.5\,\mu\mathrm{m}$. This is supported by the fact that to zero order we can consider the supercurrent to be distributed uniformly in the junction.

Having attributed each channel to a critical current it is possible to calculate the critical current densities of each junction, displayed in the right image of Fig. 4.37. At high backgate voltage, the narrower junction has a higher supercurrent density reaching a value of $I_{c2}/W = 62\,\mathrm{nA}\,\mu\mathrm{m}^{-1}$, while the wider one shows a smaller critical current density of at maximum $40\,\mathrm{nA}\,\mu\mathrm{m}^{-1}$. The supercurrent *density* obtained for the narrow junction is also consistent with was found for the symmetric SQUID, in which the two junctions had the same geometry, supporting the assumption that wider junction carries the higher amount of *absolute supercurrent*, while carrying lower *supercurrent density*.

To investigate the possibility of calculating the CPR from the interference pattern, the degree of asymmetry of the device as a function of the back gate, I_{c1}/I_{c2}, is a useful parameter. It is plotted in Fig. 4.38. From a factor of 2 at voltages around $18\,\mathrm{V}$, the ratio is increased, up to a maximum of 4.5 at a back gate voltage of $4.5\,\mathrm{V}$, with the trend increasing more rapidly at lower back gate voltages, when one junction is close to the supercurrent pinch-off point.

As mentioned in Sec. 2.4.6: with a maximum degree of asymmetry of 4.5 it is not possible to state that the interference pattern perfectly resembles the CPR of the small-I_c junction. However, from a theoretical perspective, it is valuable to estimate the deviation of the interference pattern from the CPR at this asymmetry ratio. In the worst case

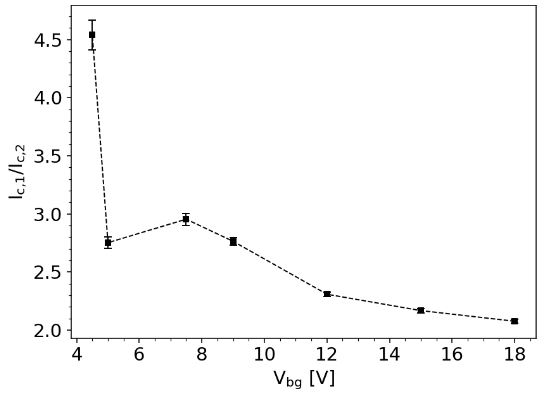

Figure 4.38: Asymmetry between the two arms of the asymmetric SQUID, calculated as I_{c1}/I_{c2} at each value of back gate.

scenario[7], suppose that the high-I_c junction has a sinusoidal CPR. Modeling the CPR with eq. 2.31 with a single effective transmission coefficient, τ^*, it is possible to estimate the error made when associating the AC part of the interference pattern with the CPR.

To this end, four asymmetric SQUID interference patterns are calculated for the following cases: $\tau_1^* = 0$ and $\tau_2^* = \{0, 0.5, 0.7, 0.9\}$. The AC part of the interference pattern (as it is usually done) $I_c(\Phi) - \langle I_c(\Phi)\rangle$ is compared to the CPR of the small-I_c junction. As τ_2^* increases, the interference pattern resemble less the CPR of the small-I_c junction, and the relative error committed is:

$$\max\left(\frac{(I_c(\Phi) - \langle I_c(\Phi)\rangle) - I_2(2\pi\Phi/\Phi_0)}{I_{c2}}\right) = \begin{cases} 6\% & \text{for } \tau_2^* = 0 \\ 30\% & \text{for } \tau_2^* = 0.5 \\ 50\% & \text{for } \tau_2^* = 0.7 \\ > 100\% & \text{for } \tau_2^* = 0.9 \end{cases}$$

Since there is no reason to exclude a high transparency (τ_2^*) of the interfaces of the narrow junction, it is not possible to derive the CPR directly from these measurements. More advanced numerical methods are required to make any meaningful statements about the CPR.

Temperature dependence The results of the fit for the temperature behavior at a back gate of $15\,\mathrm{V}$ are reported in Fig. 4.39. The left image shows the decay of the critical currents with temperature, while the image on the right show the behavior for the supercurrent density. The reduced values of critical currents with respect to the values shown previously are due to the fact that this dataset come from the second cool-down of the asymmetric device. A linear trend is found in both junctions, keeping the asymmetry also at high temperature,with the supercurrent density of the narrow junction decaying more rapidly. It is noteworthy that the supercurrent persists at temperatures

[7] As pointed out in Sec. 2.4.6, a strong asymmetry in the critical currents has to hold alongside a strong asymmetry in the derivatives of the CPRs. The best condition arises when the high-I_c junction is strongly skewed and the target junction of the CPR measurement is sinusoidal.

well exceeding one kelvin, which aligns with the observations made in the symmetric device.

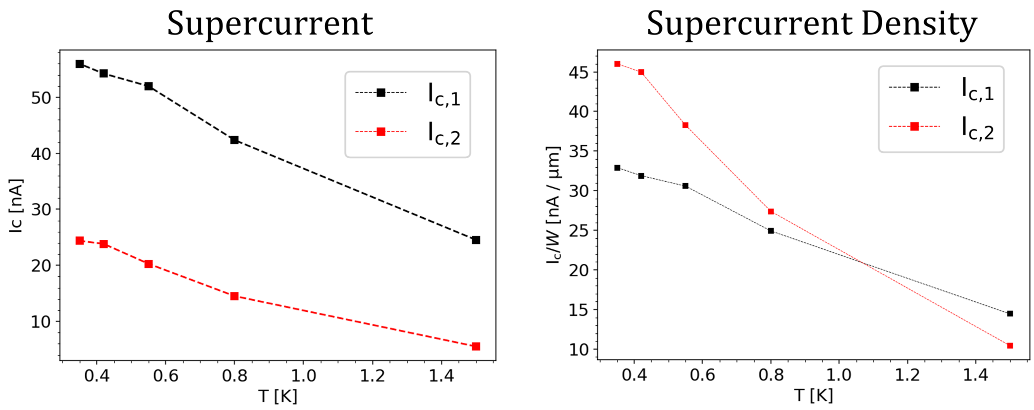

Figure 4.39: **Left**: Critical current values estimated with the fit procedure of the SQUID patterns against the temperature. **Right** Critical current densities, showing a different decay for the narrow junction (I_{c2}, red) and the wider junction (I_{c1}, black).

4.5.4 *Numerical Simulations*

Thanks to an active collaboration with the group led by Prof. Maura Sassetti from the University of Genoa, numerical simulations are performed to gain deeper insight and a better understanding of the physics governing the SQUIDs presented in this thesis. These simulations have proven to be invaluable in elucidating the behavior observed in these systems. As this project is still ongoing, the current focus has been on performing and refining these procedures for the symmetric SQUID. Consequently, the results and discussions presented here pertain exclusively to this specific device. It is important to note that the methodologies and findings reported in this section are being subject to further refinement as the research progresses.

Motivations for a tight-binding approach In the most simple model (Josephson junctions with sinusoidal CPR), the effect of destructive interference is explained by the condition of flux quantization and happens for a specific value of the magnetic field where the superconducting phase drops of the two junctions are out of phase by $180°$; this has been treated explicitly in Sec. 2.4.2.

When looking at the SQUID interference pattern presented in Fig. 4.18, one notes that the interference pattern of the *symmetric* SQUID does not modulate to zero at high back gate voltage. Different hypothesis can be made to discuss possible reasons for non-zero supercurrent in the minima of the interference pattern. If the two junctions are identical, one would naively expect the same critical current of each arm with the same modulation, such that with the two junction in "antiphase", $I_1(\varphi_1) = -I_2(\varphi_2)$, the total current is zero for every back gate voltage.

To explain the experimental observation that the interference pattern does not modulate to zero in the minima, from the standard theory of SQUIDs (that considers junctions with sinusoidal CPRs), introduced in Sec. 2.4, the following conclusions are possible:

- The two junctions possess different critical current: $I_{c1} \neq I_{c2}$.
- The loop has a finite inductance L, with a non negligible screening parameter β_L, and at first order:

$$\frac{\Delta I_c}{I_c} = \frac{1}{1+\beta_L}, \tag{4.13}$$

  such that even with the same critical current, $I_{c1} = I_{c2}$, the SQUID pattern does not modulate to zero.

This second hypothesis is discarded immediately, as in Sec. 4.1, I concluded that $\beta_L = 10^{-3}$, implying that the role of the inductance is negligible. In this case $\Delta I_c / I_c \to 1$ and the SQUID must modulate to zero.

Concluding $I_{c1} \neq I_{c2}$, and attributing the values to $I_{c1} = \langle I_c \rangle, I_{c2} = \Delta I_c/2$ is not so direct and correct. Suppose that two junctions with identical, skewed, CPRs and with the same critical current are connected to form a symmetric SQUID. The skewed CPR can be represented at zero temperature by eq. 2.31, reported here for convenience:

$$I(\varphi) = \sum_j \left(\frac{\tau_j e \Delta}{h}\right) \frac{\sin\varphi}{\sqrt{1-\tau_j \sin(\varphi/2)^2}}, \tag{4.14}$$

The "skewness" depends on the transmission coefficients: the lower the τ, the more the CPR resembles the sinusoidal case. With this CPR, it can be shown that the SQUID interference pattern does not modulate to zero even with $I_{c1} = I_{c2}$, as long as the CPR is skewed. Three interference patterns for the case $I_1(\varphi) = I_2(\varphi)$, calculated numerically for symmetric SQUIDs with CPR described by the relation written above, with three transmission coefficients, are displayed in Fig. 4.40.

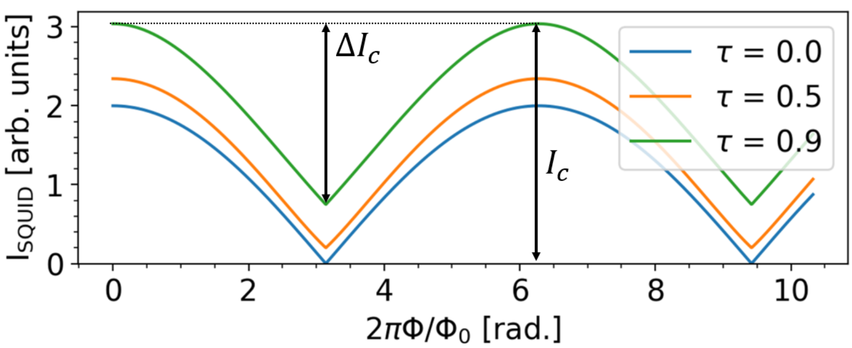

Figure 4.40: SQUID interference patterns calculated using eq. 2.31 for three different values of transmission coefficients τ.

If the junction has a sinusoidal CPR, represented by the case $\tau = 0$, then there are values of the magnetic flux for which $I_c(\Phi) = 0$. If $\tau \neq 0$, this does not happen, and the

SQUID pattern does not modulate to zero. Moreover, the more the CPR is skewed, the more limited is the modulation depth ΔI_c compared to the maximum critical current of the whole SQUID I_c. This ratio reaches an asymptotic value (from numerical calculations with $\tau \simeq 1$) of:

$$\frac{\Delta I_c}{I_c}(\tau \to 1) = \frac{1}{2} \tag{4.15}$$

That also allows to conclude that if $\Delta I_c / I_c < 0.5$, then $I_{c1} \neq I_{c2}$ for any skewness.

In the data presented for the symmetric SQUID $\Delta I_c / I_c > 0.5$. Hence one needs to consider the role of the skewness in "gapping" the symmetric SQUID interference pattern. Using SQUID models based on eq. 2.31 has revealed to be challenging, as the estimated parameters were highly dependent on the initial conditions and were not robust to small perturbations. Thus, a more in depth, refined, characterization and modeling is required that keeps into account what has been observed so far.

Tight-binding simulations of the symmetric SQUID Numerical simulations using the recursive Green's function method were performed by Dr. Simone Traverso, Dr. Samuele Fracassi, Dr. Niccolò Traverso Ziani, and Prof. Maura Sassetti from the University of Genoa and by Dr. Matteo Carrega from CNR-SPIN. The procedure is reported in Appendix B. The tight-binding simulations of the symmetric SQUID are performed with the following parameters:

1. T = $351\,\mathrm{mK}$, consistent with the temperature one measured in the experiments.

2. The normal region has the following parameters: L = $200\,\mathrm{nm}$, W = $380\,\mathrm{nm}$, as determined from the scanning electron microscope images of the real devices.

3. The induced superconducting gap is set at Δ^* = $320\,\mu\mathrm{eV}$. This value is similar to the one estimated in Sec. 4.2.2.

4. The conversion of the back-gate voltage to the chemical potential in the band is performed with this expression: $\mu = 4.12\,\mathrm{eV}\ \mathrm{V}^{-1} V_{bg}$. The chemical potentials of the two junctions are the same, motivated by the fact that only one voltage threshold was observed in the normal state characterization (Sec. 4.2.1).

5. The barriers at the interface for the two Josephson junctions (JJ1 and JJ2) are characterized by strengths of U_1= $60\,\mathrm{meV}$, U_2= $58\,\mathrm{meV}$, respectively. The slight difference in the barrier strengths is justified by the observation of the Josephson diode effect, reported in Sec. 4.4.

The comparison of the tight-binding simulations with the experimental data is shown in Fig. 4.41 for two values of back gate . The values $20\,\mathrm{V}$ and $8\,\mathrm{V}$ are chosen to represent "high" and "low" back gate voltages, respectively. At high back gate, the SQUID interference pattern does not modulate to zero, and a minimum of $I_{sw+} \simeq 10\,\mathrm{nA}$ is reported (top image, left). Instead, at low back gate voltages, the interference pattern modulates completely to zero and is not "gapped" (top image, right).

The experimental data support the following interpretation: the two Josephson junctions exhibit slightly different barrier transparencies, which are dependent on the back-gate voltage. The transparency at each NS interface is [31]:

$$\tau = \frac{1}{1+Z^2},$$

where $Z \propto \sqrt{\frac{1}{\mu}}$. From point 2, $\mu \propto V_{bg}$, with the consequence that at higher back gate voltages the interfaces are more transparent, while the opposite is true at lower voltages.

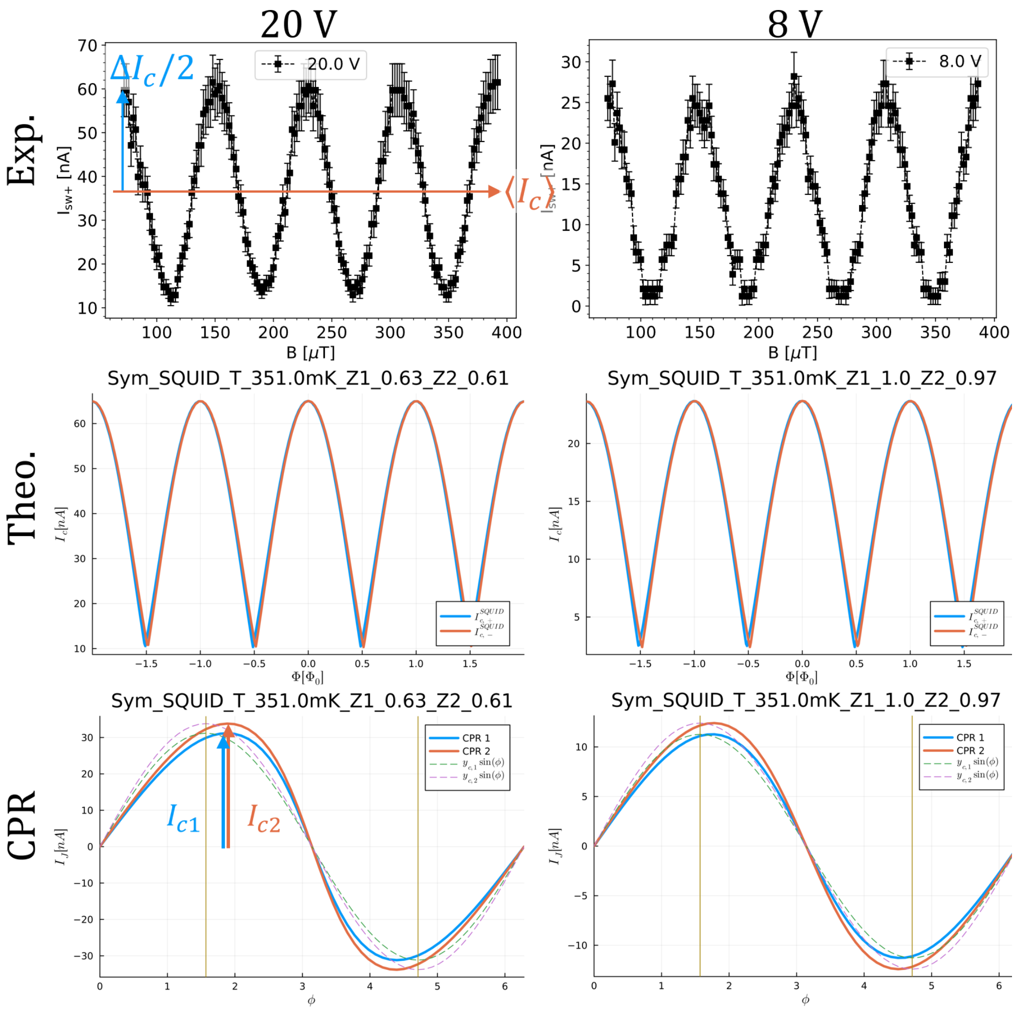

Figure 4.41: Comparison between numerical simulation and experimental data for two values of back gate voltage. The corresponding calculated CPR are plotted in the bottom row.

The transparency directly affects the skewness of the current phase relations. This becomes significant for $\tau > 0.5$, corresponding to high back-gate voltages. At $20\,\mathrm{V}$, the current phase relations (bottom image, left) of both junctions are skewed and deviate from the sinusoidal CPR. As noted in Sec. 4.5.4, if the skewness is relevant, the SQUID interference pattern does not modulate completely to zero and is "gapped". We attribute the origin of the gapped SQUID interference pattern due to the skewness of the current phase relations.

Moreover, the small asymmetry between the individual transparencies of the Josephson junctions accounts for the diode effect observed at high back-gate voltages. It is remarked that this asymmetry alone does not fully explain the gap observed in the SQUID interference pattern, and the primary reason for this gap is the skewness of the current-phase relations.

The sinusoidal model, which links I_{c2} to the average value of the interference pattern and I_{c1} to half the modulation depth, yields $I_{c2} \simeq 37\,\mathrm{nA}$ and $I_{c1} \simeq 25\,\mathrm{nA}$. When compared with the numerical simulations which yield both I_{c1} and $I_{c2} \simeq 30\,\mathrm{nA}$, it is evident (CPR on the left) that the sinusoidal model *overestimates* I_{c1} and *underestimates* I_{c2}.

Conversely, at low back-gate voltages, where $\tau \simeq 0.5$, the CPRs tend to become sinusoidal, see the CPR at $8\,\mathrm{V}$ in Fig. 4.41. This results in the closure of the gap in the SQUID interference pattern. In this regime, the simple sinusoidal model predicts $I_{c1} = I_{c2} \approx 13\,\mathrm{nA}$. When comparing this prediction with the CPR shown on the right in Fig. 4.41, there is a better agreement with respect to $20\,\mathrm{V}$, in accordance with the interpretation that the CPR becomes more sinusoidal at lower back-gate voltages.

Thanks to the tight binding simulations, a quantitative estimate of the skewness of the CPR of the Josephson junction in the symmetric SQUID geometry has been obtained. The results are consistent with the experimental observation of the diode effect and the "gap" opening of the symmetric SQUID interference pattern at high back gate voltage. These findings evidence the role of higher harmonics in the CPR of Josephson junctions based on InSb nanoflags in determining the behavior of the device.

5

Conclusions and future perspectives

In this master thesis, the following accomplishments have been reported:

1. The first fabrication of Superconducting Quantum Interference Devices (SQUIDs) with SNS Josephson junctions based on InSb nanoflags was achieved both in a symmetric and asymmetric geometry. The corresponding SQUID-type interference was observed, leading to the first demonstration of SQUID interference in two dimensional nanostructures of InSb with a periodicity of $\Phi_0 = h/2e$.

2. The devices, in both symmetric and asymmetric geometries, exhibited non- reciprocal transport, displaying a tunable Josephson diode effect, with rectification up to 5%. The rectification can be modulated by the SQUID periodicity and the back gate. The polarity of the superconducting diodes can be reversed via magnetic field, by tuning the set-point in the SQUID period.

In the symmetric geometry, the SQUID configuration can be changed from balanced at low back gate, to an unbalanced at high back gate. In the balanced configuration, it is possible to suppress the superconducting behavior by total destructive interference at an integer number of applied half flux quanta: $\Phi = \left(n + \frac{1}{2}\right) \Phi_0$. In the unbalanced configuration, partial destructive interference is displayed, i.e., the superconducting behavior is not completely suppressed by quantum interference.

Numerical simulations indicate that this behavior is attributed to the skewness of the current-phase relationship. In fact, SQUIDs fabricated with symmetric Josephson junctions with a skewed current-phase relationship do not manifest total destructive interference. In our study, the skewness of the current-phase relationship is modulated by the back gate voltage: at high back gate voltages, the current-phase relationship is skewed, whereas at low back gate voltages, it tends to become more sinusoidal.

In the asymmetric geometry, by suppressing the supercurrent in one arm of the SQUID, the interference pattern can be effectively extinguished, resulting in the absence of modulations corresponding to the SQUID periodicity, while still allowing supercurrent flow across the device. In both geometries, SQUID interferometry enables to inspect with precision the single Junctions interference patterns, giving evidence for multiple minima in the single junction interference pattern of the wide Josephson junction, a feature that was never reported in previous devices.

In SQUIDs, to manifest Josephson diode effect, it is mandatory that at least one of the two junctions possess higher harmonic content in the current phase relationship. Having observed the diode effect in both the symmetric and the asymmetric geometries, allows to confirm that Josephson junctions fabricated with InSb nanoflags exhibit a non-sinusoidal current phase relationship due to the high transparency of the interfaces.

To perform a measurement of the current phase relationship, a stronger asymmetry than the one obtained in this thesis is required, which can be achieved by two methods. One method consists in realizing a SQUID in which one arm consist of a InSb nanoflag Josephson junction in parallel with a superconducting nanobridge. As a matter of fact, nanobridges are known to exhibit critical currents of several μA and high derivatives in the current phase relationship, providing optimal conditions for probing the current phase relationship. The other approach keeps two nanoflags in the SQUID geometry, but requires the capability to manipulate one or both junctions *via* local gating. For this purpose, top gates have already been fabricated and are currently under investigation.

The results obtained in this thesis provide a solid foundation for further studies aimed at measuring and parametrizing the current phase relationship of InSb nanoflags Josephson junctions by SQUID interferometry.

Bibliography

[1] Bennet, C. H. and Di Vincenzo, D., Quantum information and computation. *Nature* **404**, (2000), 247–255.

[2] Kitaev, A., Fault-tolerant quantum computation by anyons. *Annals of Physics* **303**, (2003), 2–30.

[3] Sato, M. and Fujimoto, S., Majorana Fermions and Topology in Superconductors. *Journal of the Physical Society of Japan* **85**, (2016), 072001.

[4] Sato, M., Takahashi, Y., and Fujimoto, S., Non-Abelian Topological Order in s-Wave Superfluids of Ultracold Fermionic Atoms. *Phys. Rev. Lett.* **103**, (2009), 020401.

[5] Aghaee, M., et al., InAs-Al hybrid devices passing the topological gap protocol. *Phys. Rev. B* **107**, (2023), 245423.

[6] Ren, H., et al., Topological superconductivity in a phase-controlled Josephson junction. *Nature* **569**, (2019), 93–98.

[7] Ke, C. T., et al., Ballistic superconductivity and tunable π–junctions in InSb quantum wells. *Nature Communications* **10**, (2019), 3764.

[8] Lesser, O., Saydjari, A., Wesson, M., Yacoby, A., and Oreg, Y., Phase-induced topological superconductivity in a planar heterostructure. *Proceedings of the National Academy of Sciences* **118**, (2021), e2107377118.

[9] Salimian, S., Carrega, M., Verma, I., Zannier, V., Nowak, M. P., Beltram, F., Sorba, L., and Heun, S., Gate-controlled supercurrent in ballistic InSb nanoflag Josephson junctions. *Applied Physics Letters* **119**, (2021), 214004.

[10] Iorio, A., et al., Half-integer Shapiro steps in highly transmissive InSb nanoflag Josephson junctions. *Phys. Rev. Res.* **5**, (2023), 033015.

[11] Turini, B., Salimian, S., Carrega, M., Iorio, A., Strambini, E., Giazotto, F., Zannier, V., Sorba, L., and Heun, S., Josephson Diode Effect in High-Mobility InSb Nanoflags. *Nano Letters* **22**, (2022), 8502–8508.

[12] Della Rocca, M. L., Chauvin, M., Huard, B., Pothier, H., Esteve, D., and Urbina, C., Measurement of the Current-Phase Relation of Superconducting Atomic Contacts. *Phys. Rev. Lett.* **99**, (2007), 127005.

[13] Babich, I., Kudriashov, A., Baranov, D., and Stolyarov, V. S., Limitations of the Current–Phase Relation Measurements by an Asymmetric dc-SQUID. *Nano Letters* **23**, (2023), 6713–6719.

[14] Nichele, F., et al., Relating Andreev Bound States and Supercurrents in Hybrid Josephson Junctions. *Phys. Rev. Lett.* **124**, (2020), 226801.

[15] de Vries, F. K., Sol, M. L., Gazibegovic, S., Veld, R. L. M. o. h., Balk, S. C., Car, D., Bakkers, E. P. A. M., Kouwenhoven, L. P., and Shen, J., Crossed Andreev reflection in InSb flake Josephson junctions. *Phys. Rev. Res.* **1**, (2019), 032031.

[16] Database from Ioffe Institute of physical parameters of semiconducting materials: https://www.ioffe.ru/SVA/NSM/Semicond/InSb/index.html.

[17] Ihn, T. (2009) *Semiconductor Nanostructures: Quantum states and electronic transport*. Oxford University Press.

[18] Yu, P. Y. and Cardona, M. (2010) *Fundamentals of Semiconductors: Physics and Materials Properties*. Springer Berlin Heidelberg.

[19] Schroder, D. K. (2005) *Semiconductor Material and Device Characterization*. Wiley.

[20] Fiori, G. and Iannaccone, G. (2006) Threshold voltage dispersion and impurity scattering limited mobility in carbon nanotube field effect transistors with randomly doped reservoirs. *2006 European Solid-State Device Research Conference*, Sep., p. 202–205, IEEE.

[21] Shur, M., Low ballistic mobility in submicron HEMTs. *IEEE Electron Device Letters* **23**, (2002), 511–513.

[22] Pan, D., Fan, D. X., Kang, N., Zhi, J. H., Yu, X. Z., Xu, H. Q., and Zhao, J. H., Free-Standing Two-Dimensional Single-Crystalline InSb Nanosheets. *Nano Letters* **16**, (2016), 834–841.

[23] Tinkham, M. (2004) *Introduction to Superconductivity*. Dover Publications Inc.

[24] de Gennes, P. (1999) *Superconductivity Of Metals And Alloys*. CRC Press.

[25] London, H. and London, F., The Electromagnetic Equations of the Supraconductor. *Proceedings of the Royal Society of London. Series A - Mathematical and Physical Sciences* **149**, (1935), 71–88.

[26] Ginzburg, V. L. and Landau, L. D. (1965) 73 - On the theory of superconductivity. Ter Haar, D. (ed.), *Collected Papers of L. D. Landau*, pp. 546–568, Pergamon.

[27] Maxwell, E., Isotope Effect in the Superconductivity of Mercury. *Physical Review* **78**, (1950), 477–477.

[28] Likharev, K. K., Superconducting weak links. *Rev. Mod. Phys.* **51**, (1979), 101–159.

[29] Timm, C. (2020) *Theory of superconductivity*. Lecture notes, TU Dresden., https://tu-dresden.de/mn/physik/itp/cmt/ressourcen/dateien/skripte/Skript_Supra.pdf.

[30] Andreev, A. F., The thermal conductivity of the intermediate state in superconductors. *Sov. Phys. JETP* **19**, (1964), 1228.

[31] Blonder, G. E., Tinkham, M., and Klapwijk, T. M., Transition from metallic to tunneling regimes in superconducting microconstrictions: Excess current, charge imbalance, and supercurrent conversion. *Physical Review B* **25**, (1982), 4515–4532.

[32] Klapwijk, T., Blonder, G., and Tinkham, M., Explanation of subharmonic energy gap structure in superconducting contacts. *Physica B+C* **109–110**, (1982), 1657–1664.

[33] Octavio, M., Tinkham, M., Blonder, G. E., and Klapwijk, T. M., Subharmonic energy-gap structure in superconducting constrictions. *Physical Review B* **27**, (1983), 6739–6746.

[34] Aminov, B. A., Golubov, A. A., and Kupriyanov, M. Y., Quasiparticle current in ballistic constrictions with finite transparencies of interfaces. *Physical Review B* **53**, (1996), 365–373.

[35] Schäpers, T. (2001) *Superconductor/Semiconductor Junctions*. Springer Tracts in Modern Physics, Springer.

[36] Kjaergaard, M., Suominen, H. J., Nowak, M. P., Akhmerov, A. R., Shabani, J., Palmstrøm, C. J., Nichele, F., and Marcus, C. M., Transparent Semiconductor-Superconductor Interface and Induced Gap in an Epitaxial Heterostructure Josephson Junction. *Phys. Rev. Appl.* **7**, (2017), 034029.

[37] Sauls, J. A., Andreev bound states and their signatures. *Philosophical Transactions of the Royal Society A: Mathematical, Physical and Engineering Sciences* **376**, (2018), 20180140.

[38] van Woerkom, D. J., Proutski, A., van Heck, B., Bouman, D., Väyrynen, J. I., Glazman, L. I., Krogstrup, P., Nygård, J., Kouwenhoven, L. P., and Geresdi, A., Microwave spectroscopy of spinful Andreev bound states in ballistic semiconductor Josephson junctions. *Nature Physics* **13**, (2017), 876–881.

[39] Dvir, T., Aprili, M., Quay, C. H. L., and Steinberg, H., Zeeman Tunability of Andreev Bound States in van der Waals Tunnel Barriers. *Phys. Rev. Lett.* **123**, (2019), 217003.

[40] Beenakker, C., Universal Limit of Critical-Current Fluctuations in Mesoscopic Josephson Junctions. *Physical Review Letters* **67**, (1991), 3836–3839.

[41] Bardeen, J. et al., Structure of Vortex Lines in Pure Superconductors. *Physical Review* **187**, (1969), 556–569.

[42] Dolcini, F., Houzet, M., and Meyer, J. S., Topological Josephson ϕ_0 junctions. *Phys. Rev. B* **92**, (2015), 035428.

[43] Dolcini, F. and Giazotto, F., Switching the sign of Josephson current through Aharonov-Bohm interferometry. *Phys. Rev. B* **75**, (2007), 140511.

[44] Fracassi, S., Traverso, S., Traverso Ziani, N., Carrega, M., Heun, S., and Sassetti, M., Anomalous supercurrent and diode effect in locally perturbed topological Josephson junctions. *Applied Physics Letters* **124**, (2024), 242601.

[45] Golubov, A. A., Kupriyanov, M. Y., and Il'ichev, E., The current-phase relation in Josephson junctions. *Reviews of Modern Physics* **76**, (2004), 411–469.

[46] Granata, C. and Vettoliere, A., Nano Superconducting Quantum Interference device: A powerful tool for nanoscale investigations. *Physics Reports* **614**, (2016), 1–69.

[47] Barone, A. and Paternò, G. (1982) *Physics and Applications of the Josephson Effect*. John Wiley & Sons, Inc.

[48] Dynes, R. C. and Fulton, T. A., Supercurrent Density Distribution in Josephson Junctions. *Phys. Rev. B* **3**, (1971), 3015–3023.

[49] Ke, C. T., et al., Anomalous periodicity of magnetic interference patterns in encapsulated graphene Josephson junctions. *Phys. Rev. Res.* **1**, (2019), 033084.

[50] Suominen, H. J., Danon, J., Kjaergaard, M., Flensberg, K., Shabani, J., Palmstrøm, C. J., Nichele, F., and Marcus, C. M., Anomalous Fraunhofer interference in epitaxial superconductor-semiconductor Josephson junctions. *Phys. Rev. B* **95**, (2017), 035307.

[51] Barzykin, V. and Zagoskin, A. M., Coherent transport and nonlocality in mesoscopic SNS junctions: anomalous magnetic interference patterns. *Superlattices and Microstructures* **25**, (1999), 797–807.

[52] Clarke, J., SQUIDs. *Scientific American* **271**, (1994), 46–53.

[53] Martínez-Pérez, M. J. and Koelle, D., NanoSQUIDs: Basics & recent advances. *Physical Sciences Reviews* **2**, (2017), 20175001.

[54] Annunziata, A. J., Santavicca, D. F., Frunzio, L., Catelani, G., Rooks, M. J., Frydman, A., and Prober, D. E., Tunable superconducting nanoinductors. *Nanotechnology* **21**, (2010), 445202.

[55] Guiducci, S., Carrega, M., Taddei, F., Biasiol, G., Courtois, H., Beltram, F., and Heun, S., Full electrostatic control of quantum interference in an extended trenched Josephson junction. *Phys. Rev. B* **99**, (2019), 235419.

[56] Zalic, A., Taniguchi, T., Watanabe, K., Gazit, S., and Steinberg, H., High Magnetic Field Stability in a Planar Graphene-NbSe2 SQUID. *Nano Letters* **23**, (2023), 6102–6108.

[57] Haxell, D. Z., et al., Measurements of Phase Dynamics in Planar Josephson Junctions and SQUIDs. *Phys. Rev. Lett.* **130**, (2023), 087002.

[58] Guarcello, C., Solinas, P., Braggio, A., Di Ventra, M., and Giazotto, F., Josephson Thermal Memory. *Phys. Rev. Appl.* **9**, (2018), 014021.

[59] Beyer, J. and Drung, D., A SQUID series array dc current sensor. *Superconductor Science and Technology* **21**, (2008), 095012.

[60] Yang, Z., Zhai, C., Yang, H., Zhao, J., and Lu, Y., Investigation of Superconducting Quantum Interference Readout Electronics Based on Self-Feedback Differential Low-Noise Amplifier. *Journal of Low Temperature Physics* , (2024), n/a.

[61] Russo, R., Esposito, E., Crescitelli, A., Di Gennaro, E., Granata, C., Vettoliere, A., Cristiano, R., and Lisitskiy, M., NanoSQUIDs based on niobium nitride films. *Superconductor Science and Technology* **30**, (2016), 024009.

[62] Kim, N.-H., Kim, H.-S., Yang, Y., Peng, X., Yu, D., and Doh, Y.-J. (2018), Fabrication and Characterization of Superconducting Quantum Interference Device using $(Bi_{1-x}Sb_x)_2Se_3$ Topological Insulator Nanoribbons. ArXiv:1801.07855.

[63] Wells, F. S., Pan, A. V., Wang, X. R., Fedoseev, S. A., and Hilgenkamp, H., Analysis of low-field isotropic vortex glass containing vortex groups in $YBa_2Cu_3O_{7-x}$ thin films visualized by scanning SQUID microscopy. *Scientific Reports* **5**, (2015), 8677.

[64] Clarke, J. (1996) *Squid Fundamentals*, p. 1–62. Springer Netherlands.

[65] Clarke, J. and Braginski, A. I. (2004) *The SQUID Handbook: Fundamentals and Technology of SQUIDs and SQUID Systems*. Wiley.

[66] Voss, R. F., Laibowitz, R. B., and Broers, A. N., Niobium nanobridge dc SQUID. *Applied Physics Letters* **37**, (1980), 656–658.

[67] Awschalom, D. D., Rozen, J. R., Ketchen, M. B., Gallagher, W. J., Kleinsasser, A. W., Sandstrom, R. L., and Bumble, B., Low-noise modular microsusceptometer using nearly quantum limited dc SQUIDs. *Applied Physics Letters* **53**, (1988), 2108–2110.

[68] Nanda, G., Aguilera-Servin, J. L., Rakyta, P., Kormányos, A., Kleiner, R., Koelle, D., Watanabe, K., Taniguchi, T., Vandersypen, L. M. K., and Goswami, S., Current-Phase Relation of Ballistic Graphene Josephson Junctions. *Nano Letters* **17**, (2017), 3396–3401.

[69] Spanton, E. M., Deng, M., Vaitiekėnas, S., Krogstrup, P., Nygård, J., Marcus, C. M., and Moler, K. A., Current–phase relations of few-mode InAs nanowire Josephson junctions. *Nature Physics* **13**, (2017), 1177–1181.

[70] Murani, A., et al., Ballistic edge states in Bismuth nanowires revealed by SQUID interferometry. *Nature Communications* **8**, (2017), 15941.

[71] Koops, M. C., van Duyneveldt, G. V., and de Bruyn Ouboter, R., Direct Observation of the Current-Phase Relation of an Adjustable Superconducting Point Contact. *Phys. Rev. Lett.* **77**, (1996), 2542–2545.

[72] Ginzburg, L. V., Batov, I. E., Bol'ginov, V. V., Egorov, S. V., Chichkov, V. I., Shchegolev, A. E., Klenov, N. V., Soloviev, I. I., Bakurskiy, S. V., and Kupriyanov, M. Y., Determination of the Current–Phase Relation in Josephson Junctions by Means of an Asymmetric Two-Junction SQUID. *JETP Letters* **107**, (2018), 48–54.

[73] Rikken, G. L. J. A., Fölling, J., and Wyder, P., Electrical Magnetochiral Anisotropy. *Phys. Rev. Lett.* **87**, (2001), 236602.

[74] Ando, F., Miyasaka, Y., Li, T., Ishizuka, J., Arakawa, T., Shiota, Y., Moriyama, T., Yanase, Y., and Ono, T., Observation of superconducting diode effect. *Nature* **584**, (2020), 373–376.

[75] Wakatsuki, R., Saito, Y., Hoshino, S., Itahashi, Y. M., Ideue, T., Ezawa, M., Iwasa, Y., and Nagaosa, N., Nonreciprocal charge transport in noncentrosymmetric superconductors. *Science Advances* **3**, (2017), e1602390.

[76] Margineda, D., Crippa, A., Strambini, E., Fukaya, Y., Mercaldo, M. T., Cuoco, M., and Giazotto, F., Sign reversal diode effect in superconducting Dayem nanobridges. *Communications Physics* **6**, (2023), 343.

[77] Vodolazov, D. Y. and Peeters, F. M., Superconducting rectifier based on the asymmetric surface barrier effect. *Phys. Rev. B* **72**, (2005), 172508.

[78] Van de Vondel, J., de Souza Silva, C. C., Zhu, B. Y., Morelle, M., and Moshchalkov, V. V., Vortex-Rectification Effects in Films with Periodic Asymmetric Pinning. *Phys. Rev. Lett.* **94**, (2005), 057003.

[79] Carapella, G., Granata, V., Russo, F., and Costabile, G., Bistable Abrikosov vortex diode made of a Py–Nb ferromagnet-superconductor bilayer structure. *Applied Physics Letters* **94**, (2009), 242504.

[80] Baumgartner, C., et al., Supercurrent rectification and magnetochiral effects in symmetric Josephson junctions. *Nature Nanotechnology* **17**, (2021), 39–44.

[81] Yan, S., Luo, Y., Su, H., Gao, H., Wu, X., Pan, D., Zhao, J., Wang, J.-Y., and Xu, H. (2025), Gate Tunable Josephson Diode Effect in Josephson Junctions made from InAs Nanosheets. ArXiv:2501.15523.

[82] Mazur, G., van Loo, N., van Driel, D., Wang, J.-Y., Badawy, G., Gazibegovic, S., Bakkers, E., and Kouwenhoven, L., Gate-tunable Josephson diode. *Phys. Rev. Appl.* **22**, (2024), 054034.

[83] Zapata, I., Bartussek, R., Sols, F., and Hänggi, P., Voltage Rectification by a SQUID Ratchet. *Phys. Rev. Lett.* **77**, (1996), 2292–2295.

[84] Sterck, A., Kleiner, R., and Koelle, D., Three-Junction SQUID Rocking Ratchet. *Phys. Rev. Lett.* **95**, (2005), 177006.

[85] Fominov, Y. V. and Mikhailov, D. S., Asymmetric higher-harmonic SQUID as a Josephson diode. *Phys. Rev. B* **106**, (2022), 134514.

[86] Souto, R. S., Leijnse, M., and Schrade, C., Josephson Diode Effect in Supercurrent Interferometers. *Phys. Rev. Lett.* **129**, (2022), 267702.

[87] Cuozzo, J. J., Pan, W., Shabani, J., and Rossi, E., Microwave-tunable diode effect in asymmetric SQUIDs with topological Josephson junctions. *Phys. Rev. Res.* **6**, (2024), 023011.

[88] Li, Y., et al., Interfering Josephson diode effect in Ta2Pd3Te5 asymmetric edge interferometer. *Nature Communications* **15**, (2024), 9031.

[89] Wu, S., Guo, L., Li, Z., Shang, X., Wang, W., Huang, Q., and Zhou, J., Effect of the low-temperature buffer thickness on quality of InSb grown on GaAs substrate by molecular beam epitaxy. *Journal of Crystal Growth* **277**, (2005), 21–25.

[90] Lei, Z., Cheah, E., Schott, R., Lehner, C. A., Zeitler, U., Wegscheider, W., Ihn, T., and Ensslin, K., Quantum transport in InSb quantum well devices: progress and perspective. *Journal of Physics: Condensed Matter* **36**, (2024), 383001.

[91] Lei, Z., Cheah, E., Krizek, F., Schott, R., Bähler, T., Märki, P., Wegscheider, W., Shayegan, M., Ihn, T., and Ensslin, K., Gate-defined two-dimensional hole and electron systems in an undoped InSb quantum well. *Phys. Rev. Res.* **5**, (2023), 013117.

[92] Verma, I., Salimian, S., Zannier, V., Heun, S., Rossi, F., Ercolani, D., Beltram, F., and Sorba, L., High-Mobility Free-Standing InSb Nanoflags Grown on InP Nanowire Stems for Quantum Devices. *ACS Applied Nano Materials* **4**, (2021), 5825–5833.

[93] Suyatin, D. B., Thelander, C., Björk, M. T., Maximov, I., and Samuelson, L., Sulfur passivation for ohmic contact formation to InAs nanowires. *Nanotechnology* **18**, (2007), 105307.

[94] Bessolov, V. N. and Lebedev, M. V., Chalcogenide passivation of III–V semiconductor surfaces. *Semiconductors* **32**, (1998), 1141–1156.

[95] Solov'ev, V., Sedova, I., Lvova, T., Lebedev, M., Dement'ev, P., Sitnikova, A., Semenov, A., and Ivanov, S., Effect of sulfur passivation of InSb (001) substrates on molecular-beam homoepitaxy. *Applied Surface Science* **356**, (2015), 378–382.

[96] Giazotto, F., Heikkilä, T. T., Luukanen, A., Savin, A. M., and Pekola, J. P., Opportunities for mesoscopics in thermometry and refrigeration: Physics and applications. *Rev. Mod. Phys.* **78**, (2006), 217–274.

[97] Paolucci, F., Bianco, F., Giazotto, F., and Roddaro, S., Active Electron Cooling of Graphene. *Advanced Functional Materials* **n/a**, (2025), 2418456.

[98] Jiang, N., Lindemann, U., Giebeler, F., and Thummes, G., A 3He pulse tube cooler operating down to 1.3 K. *Cryogenics* **44**, (2004), 809–816.

[99] Radebaugh, R. (1999) Development of the pulse tube refrigerator as an efficient and reliable cryocooler. *Proc. Institute of Refrigeration (London)*, vol. 96, pp. 11–29.

[100] Pobell, F. (2007) *Matter and Methods at Low Temperatures.* Springer Berlin Heidelberg.

[101] Guiducci, S. (2014) *Electron transport and Scanning Gate Microscopy studies on hybrid ballistic SNS junctions.* Master's thesis, University of Pisa.

[102] Gubin, A. I., Il'in, K. S., Vitusevich, S. A., Siegel, M., and Klein, N., Dependence of magnetic penetration depth on the thickness of superconducting Nb thin films. *Phys. Rev. B* **72**, (2005), 064503.

[103] Rectangular Loop Inductance calculator: https://www.emisoftware.com/calculator/rectangular-loop/.

[104] Zaytseva, I., Abaloszew, A., Camargo, B. C., Syryanyy, Y., and Cieplak, M. Z., Upper critical field and superconductor-metal transition in ultrathin niobium films. *Scientific Reports* **10**, (2020), 19062.

[105] Turini, B., Salimian, S., Carrega, M., Paolucci, F., Zannier, V., Sorba, L., and Heun, S., Side-Gate Modulation of Supercurrent in InSb Nanoflag-Based Josephson Junctions. *Physica Status Solidi (b)* **n/a**, (2024), 2400534.

[106] Courtois, H., Meschke, M., Peltonen, J. T., and Pekola, J. P., Origin of Hysteresis in a Proximity Josephson Junction. *Phys. Rev. Lett.* **101**, (2008), 067002.

[107] Ambegaokar, V. and Baratoff, A., Tunneling Between Superconductors. *Phys. Rev. Lett.* **10**, (1963), 486–489.

[108] Mayer, W., Yuan, J., Wickramasinghe, K. S., Nguyen, T., Dartiailh, M. C., and Shabani, J., Superconducting proximity effect in epitaxial Al-InAs heterostructures. *Applied Physics Letters* **114**, (2019), 103104.

[109] Han, Z., Allain, A., Arjmandi-Tash, H., Tikhonov, K., Feigel'man, M., Sacépé, B., and Bouchiat, V., Collapse of superconductivity in a hybrid tin–graphene Josephson junction array. *Nature Physics* **10**, (2014), 380–386.

[110] Kulik, I. O. and Omel'yanchuk, A. N., Properties of superconducting microbridges in the pure limit. *Soviet Journal of Low Temperature Physics* **3**, (1977), 459–461.

[111] Zaitsev, A., Quasiclassical Equations of the Theory of Superconductivity for Contiguous Metals and the Properties of Constricted Microcontacts. *Journal of Experimental and Theoretical Physics* **86**, (1984), 1742–1758.

[112] Haberkorn, W., Knauer, H., and Richter, J., A theoretical study of the current-phase relation in Josephson contacts. *Physica Status Solidi (a)* **47**, (1978), K161–K164.

[113] Niebler, G., Cuniberti, G., and Novotný, T., Analytical calculation of the excess current in the Octavio–Tinkham–Blonder–Klapwijk theory. *Superconductor Science and Technology* **22**, (2009), 085016.

[114] Artemenko, S., Volkov, A., and Zaitsev, A., On the excess current in microbridges S-c-S and S-c-N. *Solid State Communications* **30**, (1979), 771–773.

[115] Borzenets, I. V., et al., Ballistic Graphene Josephson Junctions from the Short to the Long Junction Regimes. *Phys. Rev. Lett.* **117**, (2016), 237002.

[116] Kayyalha, M., Kargarian, M., Kazakov, A., Miotkowski, I., Galitski, V. M., Yakovenko, V. M., Rokhinson, L. P., and Chen, Y. P., Anomalous Low-Temperature Enhancement of Supercurrent in Topological-Insulator Nanoribbon Josephson Junctions: Evidence for Low-Energy Andreev Bound States. *Phys. Rev. Lett.* **122**, (2019), 047003.

[117] Lee, G.-H., Kim, S., Jhi, S.-H., and Lee, H.-J., Ultimately short ballistic vertical graphene Josephson junctions. *Nature Communications* **6**, (2015), 6181.

[118] Clark, A. and Ekin, J., Defining critical current. *IEEE Transactions on Magnetics* **13**, (1977), 38–40.

[119] Vedin, R. and Lidmar, J., Switching current distributions in superconducting nanostrips. *Phys. Rev. Res.* **7**, (2025), 013066.

[120] Hazra, D., Kirtley, J. R., and Hasselbach, K., Retrapping Current in Bridge-Type Nano-SQUIDs. *Phys. Rev. Appl.* **4**, (2015), 024021.

[121] Lefevre-Seguin, V., Turlot, E., Urbina, C., Esteve, D., and Devoret, M. H., Thermal activation of a hysteretic dc superconducting quantum interference device from its different zero-voltage states. *Phys. Rev. B* **46**, (1992), 5507–5522.

[122] Massarotti, D., Pal, A., Rotoli, G., Longobardi, L., Blamire, M. G., and Tafuri, F., Macroscopic quantum tunnelling in spin filter ferromagnetic Josephson junctions. *Nature Communications* **6**, (2015), 7376.

[123] Li, S.-X., Yu, Y., Zhang, Y., Qiu, W., Han, S., and Wang, Z., Quantitative Study of Macroscopic Quantum Tunneling in a dc SQUID: A System with Two Degrees of Freedom. *Phys. Rev. Lett.* **89**, (2002), 098301.

[124] Balestro, F., Claudon, J., Pekola, J. P., and Buisson, O., Evidence of Two-Dimensional Macroscopic Quantum Tunneling of a Current-Biased dc SQUID. *Phys. Rev. Lett.* **91**, (2003), 158301.

[125] Levajac, V., Barakov, H., Mazur, G. P., van Loo, N., Kouwenhoven, L. P., Nazarov, Y. V., and Wang, J.-Y., Supercurrent in the Presence of Direct Transmission and a Resonant Localized State. *Phys. Rev. Lett.* **132**, (2024), 176304.

[126] Kaperek, K., Heun, S., Carrega, M., Wójcik, P., and Nowak, M. P., Theory of scanning gate microscopy imaging of the supercurrent distribution in a planar Josephson junction. *Phys. Rev. B* **106**, (2022), 035432.

[127] Vurgaftman, I., Meyer, J. R., and Ram-Mohan, L. R., Band parameters for III–V compound semiconductors and their alloys. *Journal of Applied Physics* **89**, (2001), 5815–5875.

[128] Furusaki, A., DC Josephson effect in dirty SNS junctions: Numerical study. *Physica B: Condensed Matter* **203**, (1994), 214–218.

[129] Asano, Y., Numerical method for dc Josephson current between d-wave superconductors. *Phys. Rev. B* **63**, (2001), 052512.

[130] Sancho, M. P. L., Sancho, J. M. L., Sancho, J. M. L., and Rubio, J., Highly convergent schemes for the calculation of bulk and surface Green functions. *Journal of Physics F: Metal Physics* **15**, (1985), 851.

A

Critical Current Determination

In the study of superconducting devices, the characterization of the critical currents as a function of different parameters represents the easiest and most important way to investigate the properties of these systems. In this appendix, the method used throughout the thesis to extrapolate the values of the switching and retrapping currents from the $V-I$ curves is explained and commented, starting with some considerations on the superconducting transition and proceeding with the description of the algorithm.

Estimating the critical current

Given the $V-I$ curve of a superconducting element, the issue of defining the critical current at which the element transitions into the normal state has been previously considered, highlighting the limitations of various definitions. This is because the $V-I$ characteristics in most situations are not step functions but exhibit a continuous increase in voltage with increasing current from the superconducting to the dissipative state. The various possible definitions of this quantity make comparisons between experiments challenging and can also affect the shape of the parametrization of the critical current [118]. Mapping the definition of superconductivity directly onto the definition of critical current is problematic. Superconductivity can be summarized as a phase of matter exhibiting both zero electrical resistance and the Meissner effect, but from a practical perspective, it is clear that demonstrating both *simultaneously* can be extremely challenging, if not impossible, for most experimental setups available today. Because of this, the most commonly used methods rely on identifying regions of zero resistance. Since this thesis investigates the physics of the Josephson effect, I will discuss the case of Josephson junctions, with non-obvious extensions to SQUIDs.

In the ideal case, a finite current flows through a Josephson junction without developing a voltage drop. For this reason, it is often referred to as "supercurrent". This happens up to a certain value defined as critical current (I_c), where a transition to a finite voltage state occurs. Given the Current-Phase-Relationship (CPR) $I(\varphi)$ introduced in Sec. 2.3.4, the critical current I_c is defined as:

$$I_c = \max_{\varphi} I(\varphi) \tag{A.1}$$

How the transition from the superoconducting to the dissipative state manifests depends on experimental conditions such as temperature, noise, sweep rate, geometry of the setup, and other parameters [119]. In the optimal case, a clean step function transition occurs, as shown in panel (a) of Fig. A.1.

When contributions from noise and temperature are non-negligible, the $V - I$ curve appears more rounded, as in panel (b). Consequently, the "transition" feature is obscured by a gradual increase in the average voltage drop across the device as the current bias is increased.

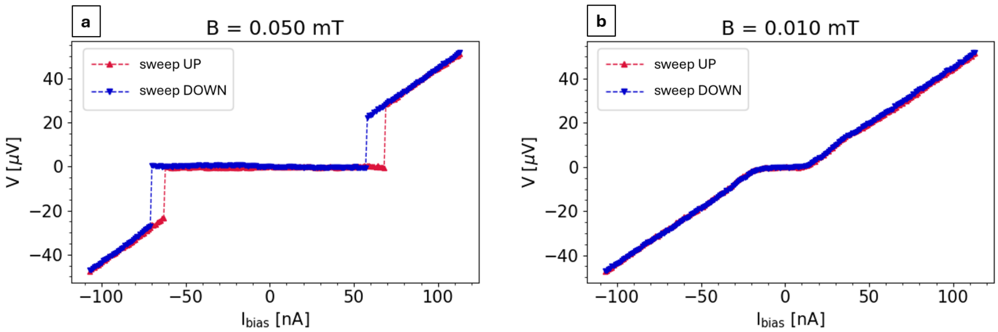

Figure A.1: **(a)** $V - I$ curve presenting a difference between switching and retrapping currents with a sharp and step-like transition. **(b)** $V - I$ rounded due to thermal excitations. The two curve are acquired at the same value of back gate (20 V) but at different values of magnetic field for the asymmetric SQUID (see main text).

Suppose that no noise is present in the setup, the sweep rate is very low, and the temperature is zero. In this case, the $V - I$ curve will present a sharp transition, as displayed in panel (a). In this scenario, it is unambiguous to determine the current at which the transition occurs, and many criteria can be developed that will yield consistent results. Conversely, in the case represented in panel (b), where noise is present caused by the environment and the electronics, the sweep rate is finite, and the temperature is non-zero, it is not obvious to determine I_c, since the $V - I$ curve is smooth at every value of the current. In brief, to interpret the $V - I$ curves in these cases, the dynamics of the phase difference across the superconducting elements must be taken into account.

It was mentioned in Sec. 2.3.5 that a first understanding is provided by the RCSJ model, in which the phase dynamics is mapped to the problem of determining the motion of a particle in a tilted washboard potential. One conclusion that can be drawn from the model is that the more appropriate quantity that estimates the critical current is the switching and not the retrapping current, as the latter depends more on out-of-equilibrium phenomena, such as difference in electronic temperature in the normal state and sweep rate [106, 120]. Because of this, the efforts in this section are focused on describing the switching current and the switching mechanisms and assessing whether it is appropriate to estimate I_c by measuring the switching current.

The simplest switching mechanism occurs by thermal excitation of the phase particle above the barrier in the tilted washboard potential. By modeling thermal noise as white noise (zero average and uncorrelated), in the RCSJ framework it is possible to analytically calculate the $V-I$ curves for the non-hysteretic case and for sinusoidal CPR. The voltage difference as a function of the current bias is represented by the following expression[1] [47] :

$$\langle V \rangle = \frac{2}{\gamma} R I_c \frac{\exp(\pi\gamma\alpha) - 1}{\exp(\pi\gamma\alpha)} \frac{1}{T_1} \tag{A.2}$$

$$T_1 = \int_0^{2\pi} d\varphi \exp -\frac{\gamma}{2}\alpha\varphi I_0(\gamma \sin\frac{\varphi}{2}) \tag{A.3}$$

where $\gamma = \hbar I_c/(ek_bT)$, $\alpha = I/I_c$, and I_0 is the modified Bessel function. Some important limits can be considered in this case: for $\gamma \to 0$, the case where the thermal energy dominates, $V \to RI$, and no superconductivity can be detected in the $V-I$ curve. Instead for $\gamma \to \infty$, the case in which thermal excitations are negligible, $V = 0$ for $I < I_c$; and $V = RI_c\sqrt{\alpha^2 - 1}$ for $I > I_c$. Hence is possible to distinguish precisely a dissipation-less state from a voltage-carrying one. Numerical integration of eq. A.2 gives the rounded shape for the transition with increasing ratio between the current thermal noise and critical current, as displayed in Fig. A.2.

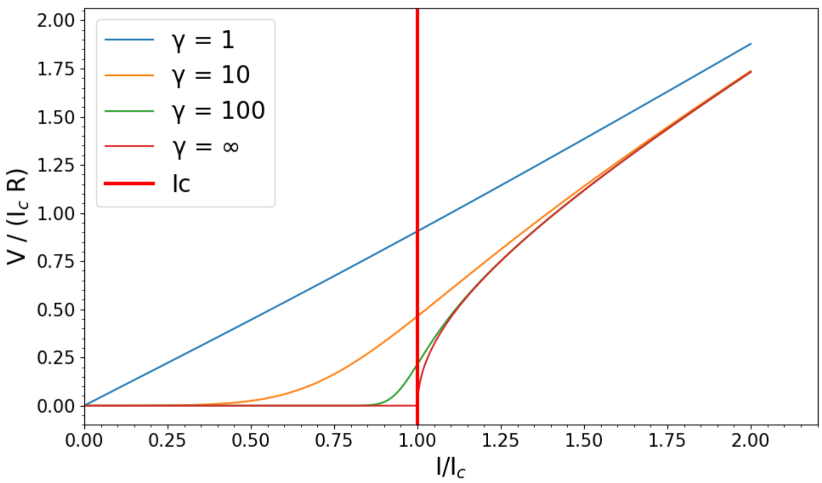

Figure A.2: Voltage current characteristic in the presence of thermal noise described by eq. A.2. High values of γ correspond to the case of low current thermal noise compared to the critical current. The transition feature at high temperature (low γ) is hidden by thermal excitations.

For the same value of the critical current, the transition at different temperatures looks different, as thermal excitations play a major role in the dynamics of the phase. The average $\dot{\varphi}$ is non-zero, resulting in a non-zero $\langle V \rangle$ also for currents below the critical current. It has to be noted that a possible temperature behavior of the critical current

[1]In stochastic equations, like the RCSJ equations with a random noise component, it is meaningless discussing the specific value of the solution, as the noise component is a stochastic variable and does not attain a particular value. However, it is meaningful to discuss the probability that a given variable has a particular value at a certain time. The quantities reported in the formulae are time and ensemble averages and should be understood in statistical terms.

has not been included in the model represented in Fig. A.2: for every value of γ, the critical current is the same. [2] From this analysis it follows that in the case of rounded $V - I$ curves due to thermal noise, a more accurate estimate of I_c is obtained by values of currents slightly larger than those for which the voltage is non-zero.

The distribution of switching current and the switching mechanism in presence of thermal excitations has been measured and characterized, confirming the power of the RCSJ framework in making accurate predictions [121]. However, recent investigations show that the simple picture of *only* thermal excitation of the phase particle is not always accurate, as macroscopic quantum tunneling through the barrier or phase diffusion can be the dominant escape mechanism from the potential minima [122, 123, 124]. Because of this, there can be situations where even if thermal excitations are negligible, premature switching caused by quantum tunneling or phase diffusion can result in switching currents being only a fraction of the critical current [57]. To discriminate the escape regime and the switching mechanism, measurements of large numbers of switching events should be performed, which is not always possible.

However, it has been argued that in the case of only thermal activation of the phase particle, the switching current is a reliable estimator of the critical current [12]. Therefore keeping in mind its limitations, the switching current still remains the best observable for this purpose and efforts towards precise measurements of this quantity are required. In this thesis, both the switching current and the retrapping current are measured with one $V - I$ curve in both directions, using a slow sweep rate (each $V - I$ curve always took more than 1 min, $\dot{I}_{\text{bias}} < 4\,\text{nA s}^{-1}$). When there is a substantial difference between switching and retrapping, the switching current is used to estimate the critical current.

There are various methods available for determining the switching current, depending on the physical quantity measured directly, such as differential resistance or voltage. Measuring derivatives with a lock-in amplifier can be time-consuming when a large number of curves need to be recorded, and performing numerical derivatives[3] on noisy data with multiple switching events can be challenging. In the dataset acquired, the voltage is measured while varying the current, and the more appropriate method should directly involve this quantity to better align with the experimental process. Setting a "threshold" to the voltage to identify the switching event is the method selected for all data acquired in this thesis, due to its greater accuracy in the case of noisy data; it is also consistent with other methods used in the literature [125].

[2] In SNS Josephson junctions where Andreev Bound States (ABS) carry the supercurrent, the temperature behavior of I_c (defined by eq. A.1) comes from the thermal occupation of the higher energy ABS, and from the temperature dependence of the induced gap $\Delta^*(T)$. In this section I am discussing the switching current at an experimental level and its difference from the critical current.

[3] Using numerical low-pass filters to ease the differentiation process is not always appropriate as it can significantly alter the nature of the data, producing artifacts.

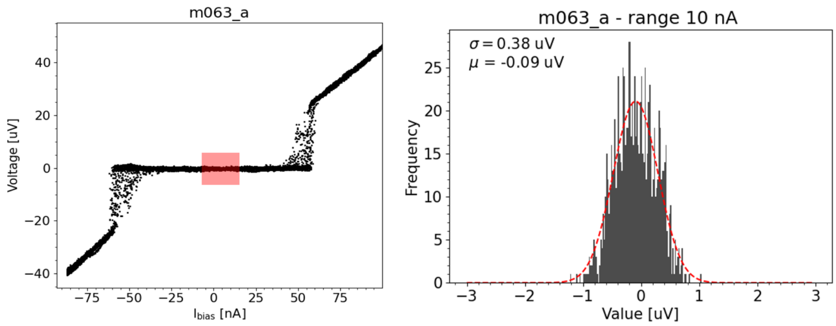

Figure A.3: $V - I$ characteristic and the distribution of the measured voltage in a range of $10\,\mathrm{nA}$ around zero, well below the transition value. From the histogram on the right, fitted with a Gaussian curve, the standard deviation is identified as $\sigma = 0.4\,\mu\mathrm{V}$.

Voltage threhsold algorithm

The essence of the voltage threshold method to determine the critical current consist in the following assessment:

$$\text{if } V \geq V_{\text{threshold}} \qquad \Rightarrow \text{Normal state}$$
$$\text{if } V < V_{\text{threshold}} \qquad \Rightarrow \text{Superconducting state}$$

How the method is implemented for real $V - I$ curves that include voltage fluctuations is explained in the following:

Step 1 consist in estimating the threshold. Every experimental setup possess a certain level of noise-floor, which depends on the filtering system, on the electronics, and on the environment surrounding the sample. The threshold is estimated from the superconducting state, which displays a zero voltage drop. For every $V - I$ curve, the distribution of voltage values in the superconducting region is analyzed, and plotted in a histogram, as shown in Fig. A.3. The histogram is fitted with a Gaussian curve, with the mean and the standard deviation to be determined as optimal parameters. In the case shown in Fig. A.3, the average is compatible with zero[4], while the standard deviation is $\sigma \approx 0.4\,\mu\mathrm{V}$. The threshold is then defined as 10 times the standard deviation:

$$V_{\text{threshold}}[i = 0] = 10\sigma \tag{A.4}$$

Step 2 consist in estimating the critical current. To be precise, the algorithm distinguish between switching and retrapping according to the sign of the sweep rate. If the magnitude of the bias current is increasing, then the switching current is estimated. If the bias current is decreasing in amplitude then the retrapping current is estimated. The critical current is defined in the following way:

$$I_c[i] = \max\left(I_{\text{bias}}\right) \text{ such that: } V((I_{\text{bias}})) < V_{\text{threshold}}[i-1] \tag{A.5}$$

In other words, the highest amount of current that can flow through the device without developing a voltage greater than the threshold is the critical current. While in principle

[4] If not, one needs to subtract the offset of the voltage measurement (e.g., arising from thermal drift of the preamplifier) of the voltage measurement

the algorithm could stop here, since an estimate of the critical current is found, this is not the case, as some inherent limitations of the algorithm are present and the estimate must be self-consistent.

Step 3 takes into account these limitations. The rule number zero for the algorithm is to determine a zero critical current for a linear $V-I$ trace. From this statement it is possible to determine an inherent limit: the threshold method cannot be applied to values of current below a certain threshold $I_{\text{threshold}}$ because in principle no distinctions are present between Ohmic traces and $V-I$ curves with $I_c < I_{\text{threshold}}$. This is sketched in Fig. A.4, where an Ohmic trace $V = RI$ displays $V < V_{\text{threshold}}$ for $I < I_{\text{threshold}}$. In this case the current threshold is defined as:

$$I_{\text{threshold}} = \frac{V_{\text{threshold}}}{R} \tag{A.6}$$

This is a first rough estimate that does not take into account the shape of the transition or the presence of excess current at low bias, which directly increase the current threshold. For typical resistances of $1.5\,\text{k}\Omega$ and voltage thresholds of $5\,\mu\text{V}$ this sets a fundamental limit to the algorithm (depending on devices, parameters, ..) around $3\,\text{nA}$. To make the estimate self consistent, the critical current must satisfy the following condition:

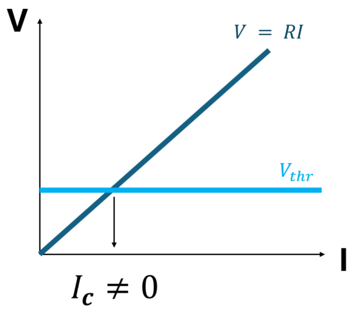

Figure A.4: Ohmic trace displaying that up to step 2 a finite critical current of $I_c = R/V_{\text{threshold}}$ is attributed, which is not physical.

$$I_c[i] > 2I_{\text{threshold}} \tag{A.7}$$

If it does not satisfy this condition, then the step 2 is repeated with $V_{\text{threshold}}[i+1] = 0.95V_{\text{threshold}}[i]$, until self consistency is obtained.

In **Step 4** the uncertainty in the critical current is estimated. Given another $V-I$ curve measured under the same conditions, the critical current values should be consistent within the given uncertainty. The uncertainty is calculated as follows: at the most basic level, there is the contribution from the resolution of the current sweep, δI_{bias}. Next, the dependence of the critical current on the chosen voltage threshold is assessed. For a perfect step-like transition, changing the threshold by a small amount, $\delta V_{\text{threshold}}$ does not affect the estimated I_c. For a rounded transition, changing the threshold results in a change in the estimated critical current proportional to the differential resistance near the estimated I_c:

$$\delta I_{c1} = \delta V_{\text{threshold}}/(\partial V/\partial I|_{I_c})$$

The smoother and rounder the transition, the greater the dependency on the chosen threshold. Since typically hundreds of $V-I$ are taken for each measurement, the standard deviation in the voltage threshold values is taken as $\delta V_{\text{threshold}}$. An additional $\delta I_{c2} = 10\% I_c$ contribution, probably overestimated, is added due to the fact that only one $V-I$ curve per parameter value is measured, not allowing to perform averaging of voltage values. While for low I_c values this is less relevant, for high I_c curves the premature switching events, due to thermal but also relevant contributions from the noise in

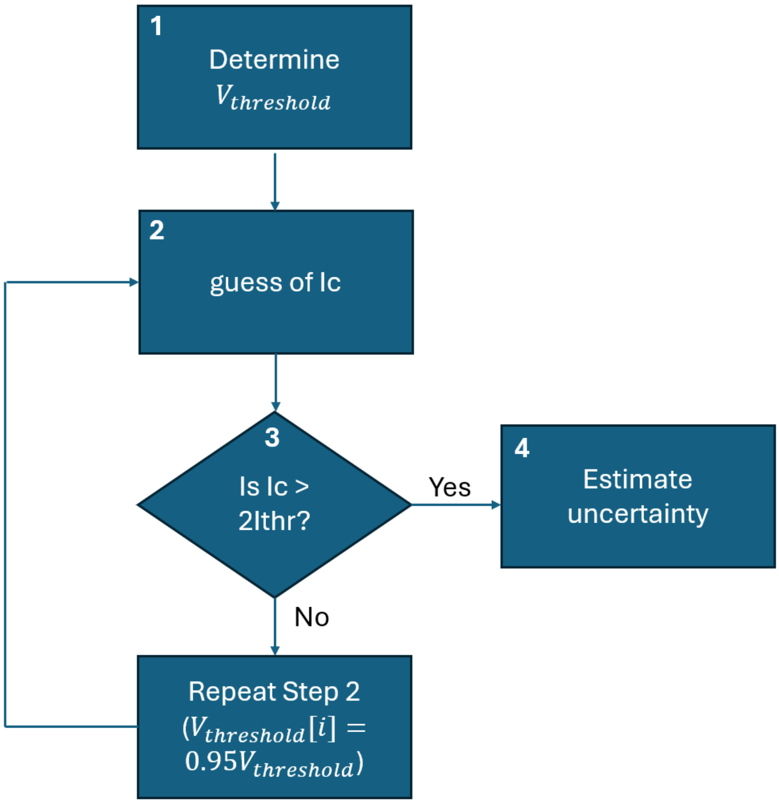

Figure A.5: Flow diagram for the threshold algorithm used

the setup, limit the accuracy of the critical current measurement. The three components obtained in this way are combined by summing the squares:

$$\Delta I_c = \sqrt{\delta I_{bias}^2 + \delta I_{c1}^2 + \delta I_{c2}^2} \tag{A.8}$$

The flow diagram representing the algorithm is displayed in Fig. A.5, while two example are displayed in Fig. A.6 and Fig. A.7 for the asymmetric and symmetric SQUID, respectively.

It has to be highlighted that the difficulty in estimating the critical current does not consist in determining the value of the sharpest transitions, but in using only one consistent method for the different types of transitions involved, from a situation $I_c > I_{th}$ to $I_c \simeq I_{th}$ to $I_c < I_{th}$. The comparisons reported in Fig. A.6 and Fig. A.7 are satisfactory and capture the features shown in the differential resistance color-maps. These comparisons are made with the differential resistance, and not with a color-map based on the voltage, for the following reason: the acquisition of one SQUID interference pattern takes several hours, and the preamplifiers, which amplify the SQUID voltage, show significant thermal drift, causing different voltage offsets for each curve. Numerical differentiation along the bias direction on each $V - I$ curve nullifies the effect of thermal drift, allowing for a more precise comparison of the switching current between $V - I$ curves at different magnetic fields.

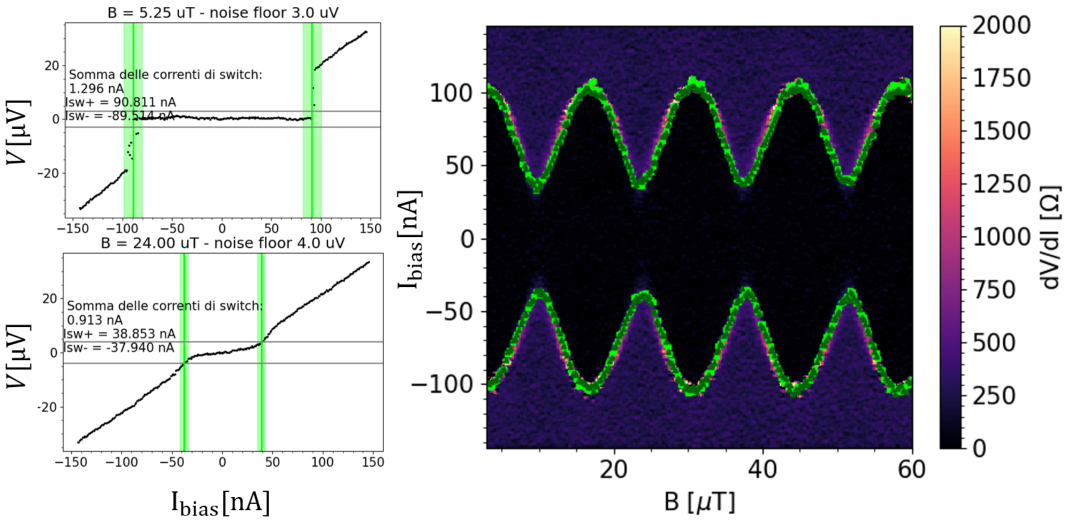

Figure A.6: In the top left and bottom left images, two $V-I$ curves for the asymmetric SQUID with the values of the switching currents are shown. The shaded vertical bars represent the uncertainty. In the right image, the differential resistance color-map is plotted with superimposed both the switching (light green) and retrapping (dark green) current values.

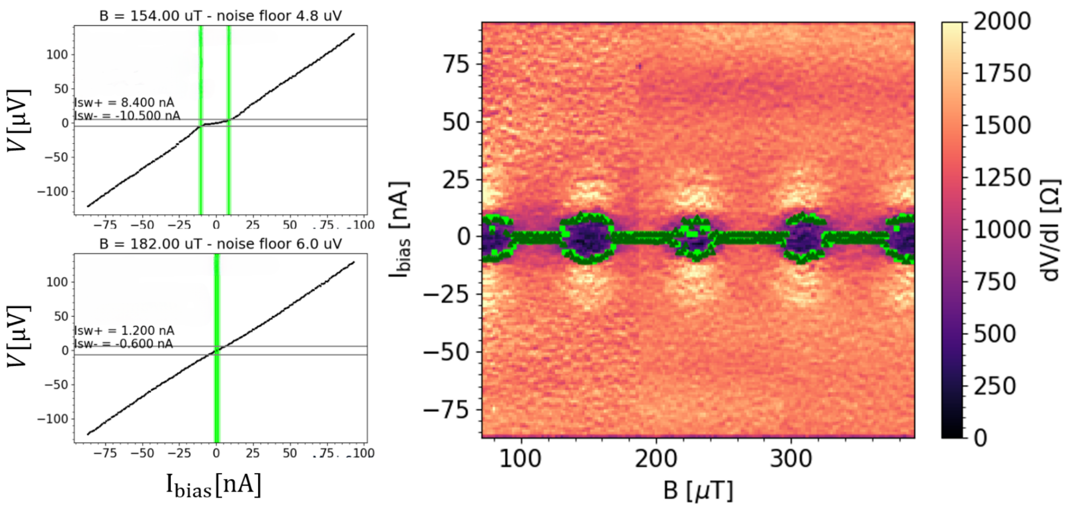

Figure A.7: In the top left and bottom left images, two $V-I$ curves for the symmetric SQUID with the values of the switching currents are shown. The shaded vertical bars represent the uncertainty. The values obtained for the $V-I$ curve in the SQUID minima are compatible with zero. In the right image, the differential resistance color-map with superimposed both the switching (light green) and retrapping (dark green) current values is plotted.

B

Recursive Green's function method to compute the Josephson supercurrent

Tight-binding modelization of InSb nanoflags

To describe the InSb nanoflag we consider a two-bands tight-binding model on the square lattice [126]. The $\boldsymbol{k}$-space Bloch Hamiltonian is given by

$$\mathcal{H}(\boldsymbol{k}) = \{(4t-\mu) - 2t[\cos(k_x)+\cos(k_y)]\}\sigma_0 - 2\mathcal{E}_R \sin(k_y)\sigma_x + 2\mathcal{E}_R \sin(k_x)\sigma_y + \mathcal{E}_B\sigma_z, \tag{B.1}$$

where σ_0 is the 2×2 identity matrix, and $\sigma_i,\ i = x, y, z$ are the Pauli matrices acting on the spin degree of freedom. Here $t = \frac{\hbar^2}{2m^* a^2}$ parametrizes the first neighbor hopping, with a the spacing assumed in the lattice discretization and m^* the electron effective mass. Moreover, $\mathcal{E}_B$ and $\mathcal{E}_R$ are energy scales associated to the magnetic field and to the Rashba spin-orbit coupling. They are defined as

$$\mathcal{E}_B = \frac{1}{2} g\mu_B B, \tag{B.2}$$

$$\mathcal{E}_R = \frac{\alpha_R}{2a}. \tag{B.3}$$

with g the giromagnetic factor, μ_B the Bohr magneton and α_R the Rashba coupling.

The real space Hamiltonian is obtained by Fourier transforming the one in Eq. (B.1), which yields

$$H = \sum_{\ell,j} \Psi^\dagger_{\ell,j} H_0 \Psi_{\ell,j} + (\Psi^\dagger_{\ell,j+1} V_y \Psi_{\ell,j} + \text{h.c.}) + (\Psi^\dagger_{\ell+1,j} V_x \Psi_{\ell,j} + \text{h.c.}), \tag{B.4}$$

where the spinor $\Psi^T_{\ell,j} = (c_{\uparrow\ell,j}, c_{\uparrow\ell,j})$ collects the operators $c_{\uparrow\ell,j}$ and $c_{\downarrow\ell,j}$ destroying an electron with spin up and down respectively at the site indexed by (ℓ, j), and

$$H_0 = (4t-\mu)\sigma_0 + \frac{1}{2} g\mu_B B\sigma_z, \tag{B.5}$$

$$V_x = -t\sigma_0 + i\mathcal{E}_R\sigma_y, \tag{B.6}$$

$$V_y = -t\sigma_0 - i\mathcal{E}_R\sigma_x. \tag{B.7}$$

Parameter	Value
m^*	$0.014 m_e$
g	-50
α_R	50meV nm
a	10nm

Table B.1: Numerical values of the model parameters used in the simulations for the InSb nanoflag.

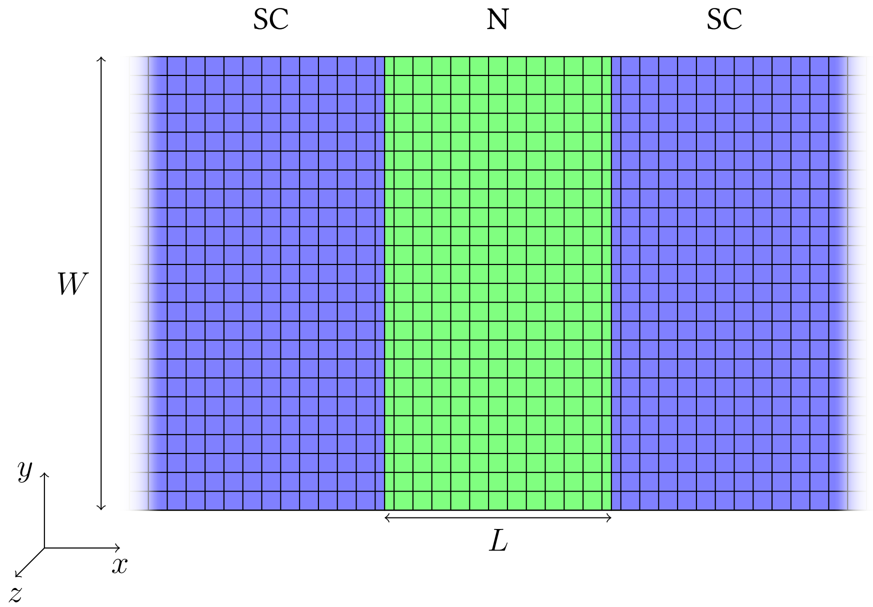

Figure B.1: Scheme of a planar Josephson junction, overlaying the discretized square lattice and laying on the $x-y$ plane. The normal region is colored in green, while the superconducting leads are in blue.

The orbital effects of the magnetic field are included via Peierls substitution of the hopping elements. We take the vector potential in the Landau gauge $\boldsymbol{A} = (-By, 0, 0)$ and replace

$$\Psi^\dagger_{\ell+1,j} V_x \Psi_{\ell,j} \mapsto \Psi^\dagger_{\ell+1,j} V_x e^{-i\frac{e}{\hbar}B(ja-y_0)a} \Psi_{\ell,j}, \tag{B.8}$$

in the real-space tight-binding Hamiltonian of Eq. (B.4), with y_0 an offset depending on the position of the junction with respect to the origin of the coordinate system. The values adopted for the parameters to match InSb [127] are reported in Tab. B.1.

Simulation of a single Josephson junction

We consider a planar Josephson junction, laying on the $x-y$ plane and extending along the x-direction, with the left and right lead obtained by proximitizing the InSb nanoflag with a conventional s-wave superconductor. We denote by L the junction length, and by W its width, placing the origin of coordinates at the bottom left corner of the scattering region. The junction is schematically represented in Fig. B.1.

The setup is described by the Bogoliubov-de-Gennes Hamiltonian

$$\mathcal{H}_{\text{BdG}} = \begin{pmatrix} \mathcal{H}(x) & \Delta(x)\mathbb{I} \\ \Delta^*(x)\mathbb{I} & -\mathcal{T}\mathcal{H}(x)\mathcal{T}^{-1} \end{pmatrix} \tag{B.9}$$

where $\mathcal{T} = -i\sigma_y\mathcal{K}$ is the operator implementing time-reversal symmetry and

$$\Delta(x) = \begin{cases} \Delta & x < 0 \\ 0 & 0 \leq x \leq L\ , \\ \Delta e^{i\phi} & x > L, \end{cases} \tag{B.10}$$

Δ the induced superconducting gap. The x-dependence in $\mathcal{H}$ is associated to the magnetic field B, which is assumed homogeneous in the normal region and zero in the leads, and to the presence of potential barriers of strength $\mathcal{U}$ on the first and last column of sites in the normal region. These are added to tune the transparency at the NS interface, which according to the Blonder-Tinkham-Klapwijk (BTK) model [31] is defined as

$$\tau = \frac{1}{1+Z^2}, \tag{B.11}$$

with $Z = \frac{m^*\mathcal{U}a}{\hbar^2 k_F}$ a pure number parametrizing the barrier strength. If we assume a parabolic dispersion of the bands (which is indeed the case at low energy) and $\mu = \frac{\hbar^2 k_F^2}{2m^*}$, then we have $Z = \sqrt{\frac{m^*}{2\mu}}\frac{\mathcal{U}a}{\hbar}$.

Having defined the tight-binding Hamiltonian of both the leads and the scattering region, the equilibrium Josephson supercurrent is computed through the recursive Green's function approach [128, 129]. Concerning the surface Green's functions of the semi-infinite uncoupled leads, these are computed via the infinite recursive Green's function method [130].

Simulation of the SQUID setup

We model the SQUID setup as shown in Fig. B.2, with the two junctions of width W_1 and W_2 parallel to each other and of the same length L. We denote the separation between the two junctions by d.

In order to compute the Josephson supercurrent in the SQUID configuration we resort to the following approximation: we assume that if the two junctions are separated by a distance much larger than the coherence length of the superconductor ($d \gg \xi$), then they can be assumed to be effectively decoupled. Thus, we actually compute the supercurrent of two independent JJs having the same superconducting order parameter, as shown in in Fig. B.3. The y-dependence in the Peierls substitution, fully accounts for the spatial separation between the junctions, correctly yielding the expected interference pattern. The effective area of the SQUID pierced by the magnetic flux is then defined as $A_{\text{SQUID}} = L\left(d + \frac{W_1+W_2}{2}\right)$.

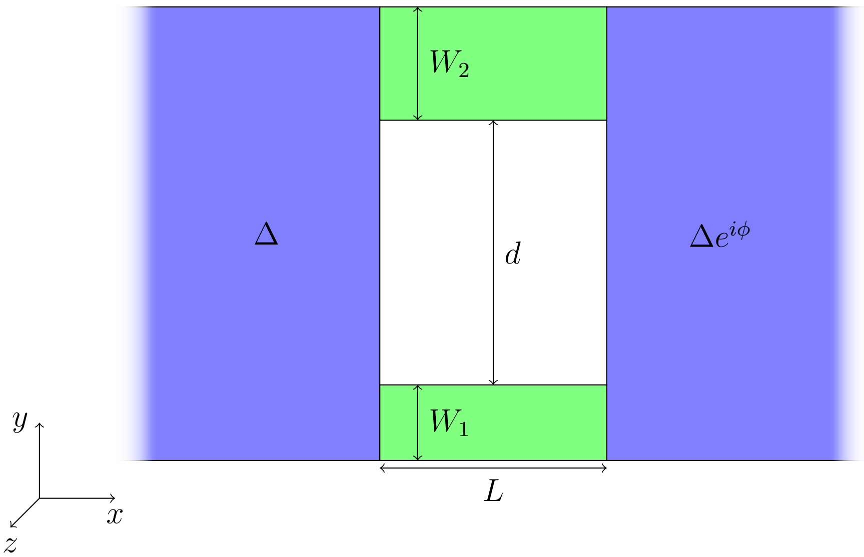

Figure B.2: Scheme of the Josephson junction, overlaying the discretized square lattice. The normal region is colored in green, while the superconducting leads are in blue.

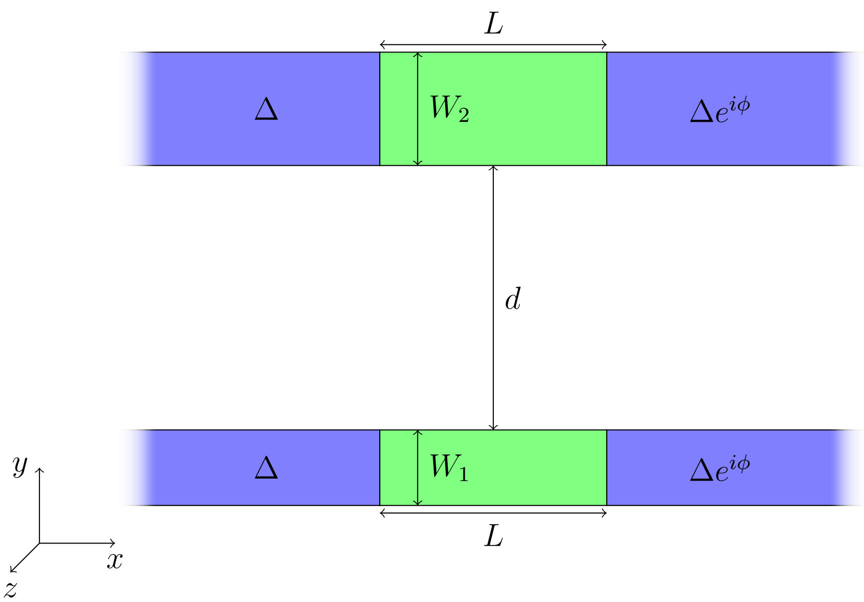

Figure B.3: Scheme of the Josephson junction, overlaying the discretized square lattice. The normal region is colored in green, while the superconducting leads are in blue.